



NAVAL POSTGRADUATE SCHOOL

MONTEREY, CALIFORNIA

THESIS

SOURCE/RECEIVER MOTION-INDUCED DOPPLER
INFLUENCE ON THE BANDWIDTH OF SINUSOIDAL
SIGNALS

by

David J. Pistacchio

December 2003

Thesis Advisor:
Second Reader:

Kevin Smith
Roy Streit

Approved for public release; distribution unlimited.

THIS PAGE INTENTIONALLY LEFT BLANK

{PRIVATE } {PRIVATE } DOCUMENTATION PAGE		REPORT	<i>Form Approved OMB No. 0704-0188</i>
<p>Public reporting burden for this collection of information is estimated to average 1 hour per response, including the time for reviewing instruction, searching existing data sources, gathering and maintaining the data needed, and completing and reviewing the collection of information. Send comments regarding this burden estimate or any other aspect of this collection of information, including suggestions for reducing this burden, to Washington Headquarters Services, Directorate for Information Operations and Reports, 1215 Jefferson Davis Highway, Suite 1204, Arlington, VA 22202-4302, and to the Office of Management and Budget, Paperwork Reduction Project (0704-0188) Washington DC 20503.</p>			
1. AGENCY USE ONLY (Leave blank)	2. REPORT DATE December 2003	3. REPORT TYPE AND DATES COVERED Master's Thesis	
4. TITLE AND SUBTITLE: Source/Receiver Motion-Induced Doppler Influence on the Bandwidth of Sinusoidal Signals		5. FUNDING NUMBERS	
6. AUTHOR(S) : David J. Pistacchio		8. PERFORMING ORGANIZATION REPORT NUMBER	
7. PERFORMING ORGANIZATION NAME(S) AND ADDRESS(ES) Naval Postgraduate School Monterey, CA 93943-5000		10. SPONSORING/MONITORING AGENCY REPORT NUMBER	
9. SPONSORING /MONITORING AGENCY NAME(S) AND ADDRESS(ES) N/A			
11. SUPPLEMENTARY NOTES The views expressed in this thesis are those of the author and do not reflect the official policy or position of the Department of Defense or the U.S. Government.			
12a. DISTRIBUTION / AVAILABILITY STATEMENT Approved for public release; distribution is unlimited		12b. DISTRIBUTION CODE	
13. ABSTRACT (maximum 200 words) <p>Most self-propelled vessels moving on, or under, the ocean surface, contain rotating machinery that radiate finite bandwidth signals into the water. Empirical evidence suggests that the signal bandwidth estimated with a far field receiver is often greater than expected. This thesis investigates the use of an acoustic propagation model to predict the received bandwidth of sinusoidal signals when both the source and the receiver are in motion. The bandwidth parameter is calculated from the multi-frequency transmission loss (TL) predicted with a re-written version of K. Smith's Monterey-Miami Parabolic Equation (MMPE) model, including both receiver and source motion. The results for various propagation environments allow exploration of the characteristics of received bandwidth, predicted from sources on the surface or at depth. The dependency of aggregate bandwidth upon conditional parameters such as range, depth, and normalized pressure are evaluated. In addition to modeling results, this thesis documents a new implementation of the MMPE model, for narrowband signals using only the MATLAB programming language. A MATLAB version has the inherent advantages of increased flexibility and portability. A MATLAB implementation of a range dependent ray trace function based upon a Runge-Kutta integration of the eikonal equations is also presented.</p>			
14. SUBJECT TERMS Source receiver motion Doppler Signal Bandwidth Parabolic Equation acoustic propagation model			15. NUMBER OF PAGES 155
16. PRICE CODE			
17. SECURITY CLASSIFICATION OF REPORT Unclassified	18. SECURITY CLASSIFICATION OF THIS PAGE Unclassified	19. SECURITY CLASSIFICATION OF ABSTRACT Unclassified	20. LIMITATION OF ABSTRACT UL

NSN 7540-01-280-5500

Standard Form 298 (Rev. 2-89)
Prescribed by ANSI Std. Z39-18

THIS PAGE INTENTIONALLY LEFT BLANK

Approved for public release; distribution unlimited.

**SOURCE/RECEIVER MOTION-INDUCED DOPPLER INFLUENCE ON THE
BANDWIDTH OF SINUSOIDAL SIGNALS**

David J. Pistacchio
Civilian
B.S., Syracuse University, 1981

Submitted in partial fulfillment of the
requirements for the degree of

MASTER OF SCIENCE IN ENGINEERING ACOUSTICS

from the

**NAVAL POSTGRADUATE SCHOOL
December 2003**

Author: David J. Pistacchio

Approved by: Dr. Kevin B. Smith
Thesis Advisor

Dr. Roy L. Streit
Second Reader

Dr. Kevin B. Smith, Chair
Engineering Acoustics Curriculum Committee

THIS PAGE INTENTIONALLY LEFT BLANK

ABSTRACT

Most self-propelled vessels moving on, or under, the ocean surface, contain rotating machinery that radiate finite bandwidth signals into the water. Empirical evidence suggests that the signal bandwidth estimated with a far field receiver is often greater than expected. This thesis investigates the use of an acoustic propagation model to predict the received bandwidth of sinusoidal signals when both the source and the receiver are in motion. The bandwidth parameter is calculated from the multi-frequency transmission loss (TL) predicted with a re-written version of K. Smith's Monterey-Miami Parabolic Equation (MMPE) model, including both receiver and source motion. The results for various propagation environments allow exploration of the characteristics of received bandwidth, predicted from sources on the surface or at depth. The dependency of aggregate bandwidth upon conditional parameters such as range, depth, and normalized pressure are also evaluated. In addition to modeling results, this thesis documents a new implementation of the MMPE model for narrowband signals using only the MATLAB programming language. A MATLAB version has the inherent advantages of increased flexibility and portability. A MATLAB implementation of a range dependent ray trace function based upon a Runge-Kutta integration of the eikonal equations is also presented.

THIS PAGE INTENTIONALLY LEFT BLANK

TABLE OF CONTENTS

I.	INTRODUCTION.....	1
II.	THEORETICAL BACKGROUND	5
	A. DERIVATION OF THE SPLIT-STEP FOURIER PE ALGORITHM	5
	B. THE SOURCE FUNCTION INCLUDING SOURCE MOTION	10
	C. INCORPORATING RECEIVER MOTION	15
III.	M3PE IMPLEMENTATION DETAILS.....	19
	A. TAPER FUNCTIONS	19
	B. BOTTOM TRANSITION FUNCTIONS	21
	C. ATTENUATION.....	23
	D. BOTTOM ROUGHNESS.....	25
	E. RANGE AND DEPTH MESH SIZES	26
	F. LIMITATIONS OF M3PE IMPLEMENTATION.....	27
IV.	M3PE APPLIED TO BENCHMARK CASES	29
	A. TRANSMISSION LOSS FOR FLATa.....	29
	B. CONVERGENCE DEMONSTRATED ON FLATa.....	36
	C. RECIPROCITY DEMONSTRATED ON FLATa	39
	D. TRANSMISSION LOSS FOR DOWNa	39
	E. TRANSMISSION LOSS FOR IWa	43
V.	BANDWIDTH ESTIMATION AND STATISTICAL CHARACTERIZATION ..	47
VI.	NUMERICAL EXPERIMENTS WITH A MOVING SOURCE AND RECEIVER.....	51
	A. DESCRIPTION OF ENVIRONMENTS	51
	B. DESCRIPTION OF RESULTS	54
	1. Environment #1.....	54
	2. Environment #2.....	64
	3. Environment #3	73
	4. Environment #4.....	82
VII.	CONCLUSIONS.....	93
VIII.	LIST OF REFERENCES.....	95
APPENDIX A.	USER'S GUIDE FOR THE M3PE MODEL.....	101
	A.1 EXECUTABLE FILES	101
	A.2 CONTROL PARAMETER DEFINITIONS	107
	A.3 ENVIRONMENT DEFINITION FILES.....	109
APPENDIX B.	RANGE DEPENDENT RAY TRACE FUNCTION	115
	B.1 RAY THEORY	115
	B.2 NUMERICAL SOLUTION	120
	B.3 MATLAB IMPLEMENTATION	123
	B.4 BENCHMARK EXAMPLES	130
APPENDIX C.	SCALAR FORM OF THE KE OPERATOR	133

INITIAL DISTRIBUTION LIST 137

LIST OF FIGURES

Figure 1.	Wavenumber taper for source function.....	11
Figure 2.	Example frequency response vs wavenumber (a) or angle (b) for a 20 knot source moving at the grazing angles 0° (blue), 45° (red), or -45° (green) from the horizontal.....	13
Figure 3.	Examples of a depth taper (a) and wavenumber taper (b) for the case $f=100$ Hz, $c_0=1500$ m/s, and $D=200$ m	21
Figure 4.	Example water-bottom transition functions for (a) sound speed and (b) density when $\lambda = 15$ m, and (c) 2 nd derivative of density function.	23
Figure 5.	Example Bottom Roughness	26
Figure 6.	Ray trace in water column for the FLATa environment, $z_s = 30$ m.....	30
Figure 7.	Bottom parameters vs range for the FLATa environment.....	30
Figure 8.	(a) Sound speed, (b) density, and (c) attenuation vs range and depth for the FLATa environment.....	31
Figure 9.	Transmission loss vs range and depth at 250 Hz for the FLATa environment.....	32
Figure 10.	Comparison of transmission loss at 250 Hz between MMPE, Mikhin's IFD, and M3PE PE models for FLATa environment	33
Figure 11.	Transmission loss vs range and depth at 25 Hz for the FLATa environment.....	34
Figure 12.	Comparison of transmission loss at 25 Hz between MMPE, Mikhin's IFD, and M3PE PE models for the FLATa environment	34
Figure 13.	Transmission loss vs range and depth at 1000 Hz for the FLATa environment.....	35
Figure 14.	Comparison of transmission loss at 1000 Hz between MMPE, Mikhin's IFD, and M3PE PE models for the FLATa environment	36
Figure 15.	Comparison of M3PE results at 250 Hz for the FLATa environment, $\Delta r = 2.50$ m (magenta), $\Delta r = 5.0$ m (blue), $\Delta r = 10.0$ m (red), $\Delta r = 20.0$ m (green).....	38
Figure 16.	Comparison of M3PE results at 1000 Hz for the FLATa environment, $\Delta r = 2.50$ m (magenta), $\Delta r = 5.0$ m (blue), $\Delta r = 10.0$ m (red), $\Delta r = 20.0$ m (green)	38
Figure 17.	Results of a reciprocity test for the FLATa environment, $f = 250$ Hz. Magnitude of TL (upper) and phase (lower)	39
Figure 18.	Ray trace in water column for the DOWNa environment, $z_s = 30$ m ...	40
Figure 19.	Sound speed (a), density (b), and attenuation (c) vs range and depth for the DOWNa environment	41
Figure 20.	Transmission loss vs range and depth at 250 Hz for the DOWNa environment.....	42
Figure 21.	Comparison of transmission loss at 250 Hz between MMPE, Mikhin's IFD, and M3PE PE models for the DOWNa environment.....	42
Figure 22.	Ray trace in water column for the IWa environment, $z_s = 30$ m	43
Figure 23.	Sound speed vs range and depth for the IWa environment.....	44

Figure 24.	Transmission loss vs range and depth at 250 Hz for the IWa environment.....	45
Figure 25.	Comparison of transmission loss at 250 Hz between MMPE, Mikhin's IFD, and M3PE PE models for the IWa environment.....	46
Figure 26.	Example Bandwidths Computed for Three Different Functions	48
Figure 27.	Acoustic parameters for environment #1	54
Figure 28.	Ray trace for environment #1, $z_s = 50$ m	55
Figure 29.	k-f spectrum of source in environment # 1, $z_s = 50$ m, $v_s = 15$ kts	55
Figure 30.	Minimum transmission loss across frequency vs range and depth for environment # 1, $z_s = 50$ m, $v_s = 15$ kts, $v_r = -5$ kts.....	56
Figure 31.	Minimum transmission loss across frequency vs range for environment # 1, $z_s = 50$ m, $z_r = 50$ m	56
Figure 32.	Transmission loss vs frequency, environment #1, $z_s = 50$ m, $z_r = 50$ m, 5000 m $< r < 5300$ m, $v_s = 15$ kts, $v_r = -5$ kts	57
Figure 33.	Transmission loss vs frequency and range, environment #1, $z_s = 50$ m, $z_r = 50$ m, $v_s = 15$ kts, $v_r = -5$ kts	58
Figure 34.	Marginalized bandwidth vs range (a), and depth (b) , environment #1, $z_s = 50$ m, $v_s = 15$ kts, $v_r = -5$ kts	59
Figure 35.	Aggregate histogram (a) and scatter plot vs normalized linear TL (b), environment #1, $z_s = 50$ m, $v_s = 15$ kts, $v_r = -5$ kts	60
Figure 36.	Ray trace for environment #1, $z_s = 3$ m	61
Figure 37.	Minimum transmission loss across frequency vs range and depth for environment # 1, $z_s = 3$ m, $v_s = 15$ kts, $v_r = -5$ kts.....	61
Figure 38.	Minimum transmission loss across frequency vs range for environment # 1, $z_s = 3$ m, $z_r = 50$ m, $v_s = 15$ kts, $v_r = -5$ kts	62
Figure 39.	Transmission loss vs frequency, environment #1, $z_s = 3$ m, $z_r = 50$ m, 5000 m $< r < 5300$ m, $v_s = 15$ kts, $v_r = -5$ kts	62
Figure 40.	Transmission loss vs frequency and range, environment #1, $z_s = 3$ m, $z_r = 50$ m, $v_s = 15$ kts, $v_r = -5$ kts.....	63
Figure 41.	Marginalized bandwidth vs range (a), and depth (b) , environment #1, $z_s = 3$ m, $v_s = 15$ kts, $v_r = -5$ kts	63
Figure 42.	Aggregate histogram (a) and scatter plot vs normalized linear TL (b), environment #1, $z_s = 3$ m, $v_s = 15$ kts, $v_r = -5$ kts	64
Figure 43.	Acoustic parameters for environment #2	65
Figure 44.	Ray trace for environment #2, $z_s = 50$ m	65
Figure 45.	k-f spectrum of source in environment # 2, $z_s = 50$ m, $v_s = 15$ kts	66
Figure 46.	Minimum transmission loss across frequency vs range and depth for environment # 2, $z_s = 50$ m, $v_s = 15$ kts, $v_r = -5$ kts.....	66
Figure 47.	Minimum transmission loss across frequency vs range for environment # 2, $z_s = 50$ m, $z_r = 50$ m, $v_s = 15$ kts, $v_r = -5$ kts	67
Figure 48.	Transmission loss vs frequency, environment #2, $z_s = 50$ m, $z_r = 50$ m, 5000 m $< r < 5300$ m, $v_s = 15$ kts, $v_r = -5$ kts	67
Figure 49.	Transmission loss vs frequency and range, environment #2, $z_s = 50$ m, $z_r = 50$ m, $v_s = 15$ kts, $v_r = -5$ kts.....	68

Figure 50.	Marginalized bandwidth vs range (a), and depth (b), environment #2, $z_s = 50$ m, $v_s = 15$ kts, $v_r = -5$ kts	68
Figure 51.	Aggregate histogram (a) and scatter plot vs normalized linear TL (b), environment #2, $z_s = 50$ m, $v_s = 15$ kts, $v_r = -5$ kts	69
Figure 52.	Ray trace for environment #2, $z_s = 3$ m	70
Figure 53.	Minimum transmission loss across frequency vs range and depth for environment # 2, $z_s = 3$ m, $v_s = 15$ kts, $v_r = -5$ kts.....	71
Figure 54.	Minimum transmission loss across frequency vs range for environment # 2, $z_s = 3$ m, $z_r = 50$ m, $v_s = 15$ kts, $v_r = -5$ kts	71
Figure 55.	Transmission loss vs frequency, environment #2, $z_s = 3$ m, $z_r = 50$ m, 5000 m $< r < 5300$ m, $v_s = 15$ kts, $v_r = -5$ kts	71
Figure 56.	Transmission loss vs frequency and range, environment #2, $z_s = 3$ m, $z_r = 50$ m, $v_s = 15$ kts, $v_r = -5$ kts	72
Figure 57.	Marginalized bandwidth vs range (a), and depth (b) , environment #2, $z_s = 3$ m, $v_s = 15$ kts, $v_r = -5$ kts	72
Figure 58.	Aggregate histogram (a) and scatter plot vs normalized linear TL (b), environment #2, $z_s = 3$ m, $v_s = 15$ kts, $v_r = -5$ kts	73
Figure 59.	Acoustic parameters for environment #3	75
Figure 60.	Ray trace for environment #3, $z_s = 50$ m	75
Figure 61.	k-f spectrum of source in environment # 3, $z_s = 50$ m, $v_s = 15$ kts	76
Figure 62.	Minimum transmission loss across frequency vs range and depth for environment # 3, $z_s = 50$ m, $v_s = 15$ kts, $v_r = -5$ kts.....	76
Figure 63.	Minimum transmission loss across frequency vs range for environment # 3, $z_s = 50$ m, $z_r = 50$ m, $v_s = 15$ kts, $v_r = -5$ kts	77
Figure 64.	Transmission loss vs frequency, environment #3, $z_s = 50$ m, $z_r = 50$ m, 5000 m $< r < 5300$ m, $v_s = 15$ kts, $v_r = -5$ kts	77
Figure 65.	Transmission loss vs frequency and range, environment #3, $z_s = 50$ m, $z_r = 50$ m, $v_s = 15$ kts, $v_r = -5$ kts	78
Figure 66.	Marginalized bandwidth vs range (a), and depth (b), environment #3, $z_s = 50$ m, $v_s = 15$ kts, $v_r = -5$ kts	78
Figure 67.	Aggregate histogram (a) and scatter plot vs normalized linear TL (b), environment #3, $z_s = 50$ m, $v_s = 15$ kts, $v_r = -5$ kts	79
Figure 68.	Ray trace for environment #3, $z_s = 3$ m	79
Figure 69.	Minimum transmission loss across frequency vs range and depth for environment # 3, $z_s = 3$ m, $v_s = 15$ kts, $v_r = -5$ kts.....	80
Figure 70.	Minimum transmission loss across frequency vs range for environment # 3, $z_s = 3$ m, $z_r = 50$ m, $v_s = 15$ kts, $v_r = -5$ kts	80
Figure 71.	Transmission loss vs frequency, environment #3, $z_s = 3$ m, $z_r = 50$ m, 5000 m $< r < 5300$ m, $v_s = 15$ kts, $v_r = -5$ kts	81
Figure 72.	Transmission loss vs frequency and range, environment #3, $z_s = 3$ m, $z_r = 50$ m, $v_s = 15$ kts, $v_r = -5$ kts	81
Figure 73.	Marginalized bandwidth vs range (a), and depth (b), environment #3, $z_s = 3$ m, $v_s = 15$ kts, $v_r = -5$ kts	82
Figure 74.	Aggregate histogram (a) and scatter plot vs normalized linear TL (b), environment #3, $z_s = 3$ m, $v_s = 15$ kts, $v_r = -5$ kts	82

Figure 75.	Acoustic parameters for environment #4	84
Figure 76.	Ray trace for environment #4, $z_s = 50$ m	85
Figure 77.	k-f spectrum of source in environment # 4, $z_s = 50$ m, $v_s = 15$ kts	85
Figure 78.	Minimum transmission loss across frequency vs range and depth for environment # 4, $z_s = 50$ m, $v_s = 15$ kts, $v_r = -5$ kts.....	86
Figure 79.	Minimum transmission loss across frequency vs range for environment # 4, $z_s = 50$ m, $z_r = 50$ m, $v_s = 15$ kts, $v_r = -5$ kts	86
Figure 80.	Transmission loss vs frequency, environment #4, $z_s = 50$ m, $z_r = 50$ m, 5000 m $< r < 5300$ m, $v_s = 15$ kts, $v_r = -5$ kts	87
Figure 81.	Transmission loss vs frequency and range, environment #4, $z_s = 50$ m, $z_r = 50$ m, $v_s = 15$ kts, $v_r = -5$ kts	87
Figure 82.	Marginalized bandwidth vs range (a), and depth (b), environment #4, $z_s = 50$ m, $v_s = 15$ kts, $v_r = -5$ kts	88
Figure 83.	Aggregate histogram (a) and scatter plot vs normalized linear TL (b), environment #4, $z_s = 50$ m, $v_s = 15$ kts, $v_r = -5$ kts	88
Figure 84.	Ray trace for environment #4, $z_s = 3$ m	89
Figure 85.	Minimum transmission loss across frequency vs range and depth for environment # 4, $z_s = 3$ m, $v_s = 15$ kts, $v_r = -5$ kts.....	89
Figure 86.	Minimum transmission loss across frequency vs range for environment # 4, $z_s = 3$ m, $z_r = 50$ m, $v_s = 15$ kts, $v_r = -5$ kts	90
Figure 87.	Transmission loss vs frequency, environment #4, $z_s = 3$ m, $z_r = 50$ m, 5000 m $< r < 5300$ m, $v_s = 15$ kts, $v_r = -5$ kts	90
Figure 88.	Transmission loss vs frequency and range, environment #4, $z_s = 3$ m, $z_r = 50$ m, $v_s = 15$ kts, $v_r = -5$ kts	91
Figure 89.	Marginalized bandwidth vs range (a), and depth (b), environment #4, $z_s = 3$ m, $v_s = 15$ kts, $v_r = -5$ kts	91
Figure 90.	Aggregate histogram (a) and scatter plot vs normalized linear TL (b), environment #4, $z_s = 3$ m, $v_s = 15$ kts, $v_r = -5$ kts	92
Figure 91.	Color coded plot of bandwidth vs range and depth for environment #4, $z_s = 3$ m, $v_s = 15$ kts, $v_r = -5$ kts	92
Figure 92.	M3PE Functional Flow (part a)	105
Figure 93.	M3PE Functional Flow (part b)	106
Figure 94.	Example ocean environment definition file	113
Figure 95.	Bottom reflection geometry.....	125
Figure 96.	Surface reflection geometry.....	127
Figure 97.	Flow Diagram of Raytrace Function, part (a).....	128
Figure 98.	Flow Diagram of Raytrace Function, part (b).....	129
Figure 99.	Munk's canonical profile	130
Figure 100.	Example ray trace, $z_s = 1000$ m.....	131
Figure 101.	Example ray trace, $z_s = 500$ m.....	131

LIST OF TABLES

Table 1.	Environmental parameters for the FLATa environment	31
Table 2.	Environmental parameters for the DOWNa environment	41
Table 3.	Environmental parameters for the IWa environment	44
Table 4.	Mesh sizes used for each environment	52
Table 5.	MATLAB file names of functions executing the M3PE model	101
Table 6.	Input/output files	103
Table 7.	Control parameter definitions	107
Table 8.	Parameters contained in the environmental definition files.....	110
Table 9.	Input Variables to the Raytrace Function.....	124

THIS PAGE INTENTIONALLY LEFT BLANK

ACKNOWLEDGMENTS

I am greatly indebted to the significant assistance provided by my primary thesis advisor, Dr. Kevin Smith of the Naval Postgraduate School. His comprehensive lectures on Sound Propagation in the Ocean were the starting point of my understanding of this material. Also his detailed technical descriptions of Parabolic Equation propagation modeling, including many references to previous contributors, was an invaluable source of information upon which this thesis is based. His careful critique of my software implementation resulted in several important corrections and recommendations. Dr. Roy Streit (secondary reader) also contributed many useful comments, especially regarding the mathematics associated with operators. I am also grateful for the opportunity to work with many talented colleagues at the Naval Undersea Warfare Center in Newport R.I., who have served as a constant source of stimulating technical interchange. Finally, I thank my family for their patience while I spent the necessary time away from them to prepare this thesis.

THIS PAGE INTENTIONALLY LEFT BLANK

I. INTRODUCTION

This thesis is motivated by several remarks in the literature concerning spreading of a continuous wave (CW) signal in the frequency domain after propagation in an ocean waveguide (see refs. 1, 2, and 3 for example). In many cases, the frequency spreading can be attributed to differences in the received Doppler (i.e. differential Doppler) of various multipath arrivals when the source and/or receiver are in motion. Experiments also suggest that a Doppler shift imparted on transmitted signals due to surface motion is another factor (see refs. 4 and 5 for example) that can cause frequency spreading even when the source and receiver are stationary. The spread of power across frequency can be quantified into a single bandwidth parameter that is useful for aggregate signal analysis or source classification. In the case of source/receiver motion, it is likely that signal bandwidth is dependent upon the parameters defining the acoustic propagation channel and the relative positions and motion of the source and receiver. To predict the dependencies due to differential Doppler, a model of the broadband transmission loss (TL) in the presence of source and receiver motion is required.

The literature related to acoustic propagation models incorporating the effects of source and receiver motion is diverse. Much of the published work focuses upon approaches based upon ray theory. A series of papers by Jacobson and colleagues^{6,7,8,9,10,,11} use ray theory to evaluate the effect of source motion on transmission loss for specific sound speed profiles (e.g., bilinear or iso-speed SSP). A total, time-dependent, pressure field amplitude and phase is computed by summing individual ray contributions, where parameters such as travel time, received angle, and frequency are modified by relative motion. The papers differ in their focus on specific effects associated with short, intermediate and long ranges, as well as various depths and SSPs. A pair of papers by Flanagan and Weinberg^{12,13} also use ray theory to look at the coherence length and bandwidth of multiple CW signals in the presence of radial and skewed source motions.

Periodic source motion is shown to cause an amplitude modulation that “transfers power” into sidebands, thereby increasing the signal’s effective spectral bandwidth.

References 14 & 15 are among the first papers to incorporate source and/or receiver motion into a normal mode model. Hawker¹⁴ derived an approximate expression for the time-dependent pressure field as a function of wavenumbers (eigenvalues), relative source speed, mode group velocities, and mode (eigen) functions. Included in the derivation is an approximate formulation for the Doppler shifted frequencies of the individual modes as a direct function of the phase and group velocities. Another formulation of the pressure field associated with a moving source was independently derived in an earlier publication by Neubert¹⁵. The unique approximations and assumptions invoked in this work resulted in a somewhat different formulation than that presented by Hawker. Neubert, however, appears to focus on how a conventional stationary source/receiver model can be modified to estimate the field for moving source or receivers.

Hawker’s approach was referenced many years later by Schmidt and Kuperman,¹⁶ where it was compared to another model derived from a wave-number integration approach. The later formulation was used to predict the received frequency response of a band-pass signal emitted from a moving source in a shallow water waveguide. Song and Baggeroer¹⁷ also referred to Hawker’s results in their development of an algorithm to estimate source velocity by computing the Doppler shifts of individual modes.

Methods for including source or receiver motion in a parabolic equation (PE) based acoustic propagation model have also been explored. Howell, Jacobson and Seigman¹⁸ published a solution that applied a Galilean transformation to the wave equation. This equation is solved using a time harmonic pressure solution containing a frequency term that is modified by source and receiver motion. The Helmholtz equation is converted to a parabolic equation using the standard far-field approximations. In turn, this is converted to

the narrow angle parabolic equation by approximating a complicated expression involving the refraction index by a simpler term containing an “effective” refraction index. The result is then solved with standard marching algorithms. Numerical results were presented for a waveguide with a constant speed of sound, although the technique appears sufficiently general to be applied to any spatially variant sound speed profile.

Another approach is considered by Smith¹⁹ who represents source motion by modifying the starting field that initializes a Split-Step Fourier (SSF) PE marching algorithm.^{20,21} Since the source frequency of the starting field is a function of the transmitting angle and source speed (relative to the environment), the transmitting wavenumbers also experience a similar adjustment. Thus, a new starting field can be calculated that incorporates the frequency dependent source distribution as a function of vertical wavenumbers. Smith also describes a method for representing receiver motion by numerically interpolating the received pressure field across the frequency grid at each wavenumber and range. At a particular range, multiple responses in the vertical wavenumber domain versus frequency are “re-mapped” to a new wavenumber-frequency domain. This method lends itself to a very straightforward implementation.

A fair amount has also been written regarding the effects of a time varying ocean surface on the characteristics of a CW signal.^{22,23,24,25,26} Although, these effects are sometimes important, this thesis will concentrate on the effects of source/receiver motion when the surface is flat.

Given the options identified above, we have chosen to base our study on the PE acoustic propagation model implemented by Smith. To facilitate upgrades and numerical experimentation, the model was re-written in the MATLAB programming language (vice the original FORTRAN code). The implementation includes the Doppler effects on a sinusoidal signal from a moving source, and the frequency shift caused by a moving receiver. The resulting code has been named the MATLAB Monterey-Miami Parabolic Equation (M3PE) model. The theoretical background of a PE TL model, including the approach for

implementing source and receiver motion is described in Sections II and III. In Section IV, the functionality of the new implementation is validated by comparing transmission loss results against outputs also generated by the original MMPE and a code based upon a finite difference approach for several benchmark environments.

The M3PE model was used to conduct a series of numerical experiments intended to explore the effective bandwidth of the TL for various types of ocean environments and source depths. This bandwidth parameter is defined in Section V. Numerical results provided in Section VI indicate the possibility for several trends. First it was apparent that the calculated bandwidth parameter often follows the level of TL in range and depth space. That is, higher TL often results in higher bandwidth. Second, the bandwidth of TL is influenced by the tendency of the waveguide to propagate high angles. Higher bandwidths were observed when acoustic conditions allowed the propagation of significant energy at high angles, as opposed to smaller bandwidths that resulted from conditions that stripped out high angle modes. Finally, for the ocean conditions evaluated, there was a tendency for sources near the surface to result in wider TL bandwidths than sources positioned deeper in the water column and closer to the sound axis. These trends require further study since it is not completely apparent how observable they are in real oceans.

A user's guide for operation of the M3PE code is provided in Appendix A. In addition to transmission loss and bandwidth assessment, the code also includes a MATLAB implementation of a range-dependent ray trace function. The theoretical background and implementation details associated with this function are described in Appendix B.

II. THEORETICAL BACKGROUND

A. DERIVATION OF THE SPLIT-STEP FOURIER PE ALGORITHM

The following description closely follows discussions presented by Smith²⁰, and Thomson and Chapman²¹. Much of Smith's work is based upon the approach originally published by Tappert^{27,28}.

If $P(r, z, \omega t) = p(r, z)e^{-i\omega t}$ is the time-harmonic solution to the two-dimensional, angularly symmetric wave equation, then its homogenous solution in cylindrical coordinates satisfies a Helmholtz equation of the form,

$$\frac{1}{r} \frac{\partial}{\partial r} \left(r \frac{\partial p}{\partial r} \right) + \frac{\partial^2 p}{\partial z^2} + k_0^2 n^2(r, z) p = 0, \quad (1)$$

where ω is the angular frequency, $k_0 = \omega/c_0$ is the reference wave number, c_0 is the reference speed of sound, and $n(r, z) = c_0/c(r, z)$ is the range and depth dependent index of refraction. This describes the pressure at $r > 0$ due to a point source at $r=0$ and some variable depth for a constant density waveguide.

The cylindrical spreading term can be eliminated (for convenience) by substituting $p(r, z) = \frac{1}{\sqrt{r}} u(r, z)$, yielding

$$\frac{\partial^2 u}{\partial r^2} + \frac{\partial^2 u}{\partial z^2} + k_0^2 n^2(r, z) u = 0. \quad (2)$$

If we substitute the following operators,

$$P_{op} = \frac{\partial}{\partial r} \quad \text{and} \quad Q_{op} = \sqrt{n^2 + \frac{1}{k_0^2} \frac{\partial^2}{\partial z^2}}, \quad (3)$$

Eq. (2) can be rewritten as

$$(P_{op}^2 + k_0^2 Q_{op}^2) u = 0. \quad (4)$$

This can subsequently be factored into

$$(P_{op} + ik_0 Q_{op})(P_{op} - ik_0 Q_{op})u = 0 , \quad (5)$$

where the commutator operator $[P_{op}, Q_{op}] = P_{op}Q_{op} - Q_{op}P_{op}$ has been assumed to equal zero, as is true for layered media²¹. Equation (5) represents the factorization of the field into incoming and outgoing waves, where the outgoing wave must satisfy

$$P_{op}u = ik_0 Q_{op}u . \quad (6)$$

This treatment can be restricted to outgoing waves for environments where the backscattered field is small relative to the outgoing field.²¹

The field function u for the outgoing wave can now be decomposed into two parts associated with a slowly varying envelope and an oscillating phase function as defined by

$$u = \psi e^{ik_0 r} . \quad (7)$$

When this is substituted into Eq. (6), the result is the following expression for the outgoing field,

$$\frac{\partial \psi}{\partial r} = ik_0 (Q_{op} - 1)\psi , \quad (8)$$

where the PE field term ψ , is related to acoustic pressure by the equation

$$p(r, z) = \frac{1}{\sqrt{k_0 r}} \psi(r, z) e^{ik_0 r} . \quad (9)$$

Equation (8) is a differential equation of the *parabolic* form, vice the elliptical form of Eq. (4). To solve, though, we need an approximate expression for the Q_{op} operator that facilitates solution of a differential equation with a sequential marching algorithm. In our case, the algorithm propagates the solution in range using the representation

$$\psi(r + \Delta r) = \Phi(r)\psi(r) , \quad (10)$$

where

$$\Phi(r) = e^{-ik_0(Q_{op}-1)\Delta r} \quad . \quad (11)$$

In Eqs. (10) and (11), the dependence of Φ on z is suppressed.

A popular definition of Q_{op} is the “wide angle” approximation proposed by Thompson and Chapman,²¹ defined by

$$Q_{op} \approx Q_{WAP} = \left\{ \sqrt{1+\mu} \right\} + \left\{ \sqrt{1+\varepsilon} - 1 \right\}, \quad (12)$$

where

$$\mu = \frac{1}{k_0^2} \frac{\partial^2}{\partial z^2} \quad , \quad \varepsilon = n^2 - 1 \quad . \quad (13)$$

Substituting (12) into (8) results in

$$\frac{\partial \psi}{\partial r} = ik_0 \left(\left\{ \sqrt{1+\mu} \right\} + \left\{ \sqrt{1+\varepsilon} - 1 \right\} - 1 \right) \psi, \quad (14)$$

which can be rewritten as

$$\frac{\partial \psi}{\partial r} = -ik_0 (T_{op} + U_{op}) \psi, \quad (15)$$

where

$$T_{op} = 1 - \sqrt{1+\mu} = 1 - \sqrt{1 + \frac{1}{k_0^2} \frac{\partial^2}{\partial z^2}}. \quad (16)$$

and

$$U_{op} = 1 - \sqrt{1+\varepsilon} = 1 - n = 1 - \frac{c_0}{c(r,z)}. \quad (17)$$

Equation (16) is called the kinetic energy (KE) operator and Eq. (17) is called the potential energy (PE) operator. Using Eqs. (10) and (11), we can implement the marching algorithm using the substitution

$$\psi(r + \Delta r) = \Phi(r) \psi(r) = e^{-ik_0(Q_{op}-1)\Delta r} \psi(r) = e^{-ik_0\Delta r(T_{op} + U_{op})} \psi(r). \quad (18)$$

This manipulation has effectively split the original operator Q_{op} , into an

operator in the z domain (U_{OP}), and an operator in wavenumber space (T_{OP}). Next, we invoke the approximation, $e^{A+B} = e^A e^B e^{[A,B]_{+...}}$ by using the Campbell-Baker-Hausdorff expansion.^{20,29} Since T_{OP} and U_{OP} are small the commutator term can also be neglected. (We note that the approximation is not necessarily valid for operators as it is for algebraic variables, but it is assumed to be sufficiently accurate here.) The resulting propagation algorithm becomes

$$\psi(r + \Delta r) = e^{-ik_0 \frac{\Delta r}{2} U_{OP}(r + \Delta r)} e^{-ik_0 \Delta r T_{OP}} e^{-ik_0 \frac{\Delta r}{2} U_{OP}(r)} \psi(r) , \quad (19)$$

where the potential energy operator was segmented to center the result at each range step.

To apply the KE operator in practice, we require a scalar version of T_{OP} defined as²⁰

$$\hat{T}_{OP}(k_z) = 1 - \sqrt{1 - \frac{k_z^2}{k_0^2}} , \quad (20)$$

$\hat{T}_{OP}(k_z)$ is multiplied by the transformed field in wavenumber space. Appendix C explains how this is equivalent to applying the original operator T_{OP} .

Then, Eq. (19) is implemented by the following sequence of Split-Step Fourier (SSF) transforms and propagation functions²⁰:

$$\psi(r + \Delta r, z) = e^{-ik_0 \frac{\Delta r}{2} U_{OP}(r + \Delta r, z)} \times IDFT \left\{ e^{-ik_0 \Delta r \hat{T}_{OP}(k_z)} \times DFT \left[e^{-ik_0 \frac{\Delta r}{2} U_{OP}(r, z)} \times \psi(r, z) \right] \right\} , \quad (21)$$

where we assume the MATLAB convention for the Discrete Fourier Transform, i.e.

$$DFT \Rightarrow \Psi(k) = \sum_{z=0}^{N-1} \psi(z) e^{-i \frac{2\pi}{N} kz} , \quad k = 0, 1, \dots, N-1 , \quad (22)$$

$$IDFT \Rightarrow \psi(z) = \frac{1}{N} \sum_{k=0}^{N-1} \Psi(k) e^{i \frac{2\pi}{N} kz} , \quad z = 0, 1, \dots, N-1 . \quad (23)$$

Equation (21) concisely represents a series of steps. First the original field

function $\psi(r, z)$ is multiplied by the PE operator (evaluated at range r) in the depth domain. The product is Fourier transformed into wavenumber space using Eq. (22). Then the scalar equivalent of the KE operator is applied via multiplication prior to inverse transforming the product back into the depth domain. Finally, the result is multiplied by the PE operator evaluated at range $r+\Delta r$.

In practice, the variables z and r are replaced by the discrete values z_n and r_j . First r_j is defined as

$$r_j = (j - 1)\Delta r \quad , \quad j = 1, 2, 3, \dots \quad (24)$$

and z_n is defined on the half space mesh as

$$z_n = \begin{cases} \left(n - \frac{1}{2}\right)\Delta z, & n = 1, \dots, \frac{N_z}{2} \\ -\left(N_z - n - \frac{1}{2}\right)\Delta z, & n = \frac{N_z}{2} + 1, \dots, N_z \end{cases} \quad . \quad (25)$$

For conciseness, we will drop the “z” subscript on the wavenumber, $k_z \rightarrow k$, and note that all further references to wavenumber imply the vertical component, unless specifically stated otherwise. The sampling in wavenumber space, k_n , is then defined as

$$k_n = \begin{cases} n\Delta k, & n = 1, \dots, \frac{N_z}{2} \\ -(N_z - n)\Delta k, & n = \frac{N_z}{2} + 1, \dots, N_z \end{cases} \quad , \quad (26)$$

where

$$\Delta k = \frac{\pi}{D} \quad \text{and} \quad \Delta z = \frac{2D}{N_z} \quad , \quad (27)$$

and D is the maximum depth of the water column.

Up to this point, the fluid density has been assumed to be constant. However, a depth variant density can be accommodated in the solution to the

wave equation by replacing the index of refraction, n , in Eq. (2), with an effective index given by

$$n'^2 = n^2 + \frac{1}{2k_0^2} \left[\frac{1}{\rho} \nabla^2 \rho - \frac{3}{2} \left(\frac{1}{\rho} \nabla \rho \right)^2 \right] . \quad (28)$$

According to Smith,²⁰ this can be represented in the marching algorithm by adding a second term to the potential energy propagator as

$$U(z) = U_1(z) + U_2(z) , \quad (29)$$

where $U_1(z)$ is defined by Eq. (17), and $U_2(z)$ is defined by the approximation

$$U_2(z) \approx -\frac{1}{k_0^2} \left[\frac{1 - \sqrt{\rho_w / \rho_b}}{1 + \sqrt{\rho_w / \rho_b}} \right] H_\rho''(z - z_b) , \quad (30)$$

where $H_\rho''(z - z_b)$ is the second derivative of a density transition function to be defined later in Section III-B.

B. THE SOURCE FUNCTION INCLUDING SOURCE MOTION

The PE marching algorithm requires an initial condition at $r = 1$ m for all z . As described by Smith,²⁰ an omni directional point source can be specified by a pair of delta functions for the source at depth z_s , and its image above the surface. A Fourier transformation converts this representation back to the wavenumber domain, resulting in the expression

$$\psi(r = 0, k_n) = \alpha \int_{-\infty}^{\infty} [\delta(z - z_s) - \delta(z + z_s)] e^{-ik_n z} dz = -2i\alpha \sin(k_n z_s) , \quad (31)$$

where α is the scale factor defined as

$$\alpha = \sqrt{\frac{iR_0}{2\pi k_0}} , \quad (32)$$

and R_0 is the reference distance of 1 m.

Next, the source function is modified by a function that corrects far field

errors in the PE solution. This function, suggested by Thomson and Bohun,³⁰ is defined as

$$F(k_n) = \left(1 - \frac{k_n^2}{k_0^2}\right)^{-1/4}, \quad (|k_n| < k_0) \quad . \quad (33)$$

The correction function is set to zero when $|k_n| > k_0$, since this represents an evanescent mode. An illustration of this function for a particular value of k_0 is shown in Fig. 1 below. It is observed that the correction factor in the starting field is most significant at the higher wavenumbers (i.e., larger angles).

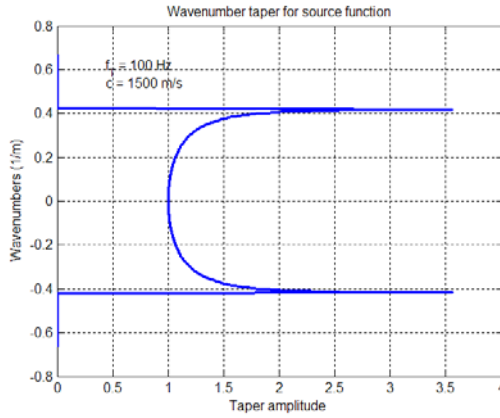


Figure 1. Wavenumber taper for source function

Finally, an extra phase term of $e^{ik_n \frac{\Delta z}{2}}$ is applied to account for the half cell depth grid defined in Eq. (25). The result is a wide angle point source, a.k.a. starting function, specified in the wavenumber domain as

$$\psi(r=0, k_n) = -2i \sqrt{\frac{iR_0}{2\pi k_0}} \left(1 - \frac{k_n^2}{k_0^2}\right)^{-1/4} \sin(k_n z_s) e^{ik_n \frac{\Delta z}{2}}. \quad (34)$$

The starting function presented thus far is only valid for a stationary omnidirectional source. To account for source motion, we recall that $k = k_0 \sin(\theta)$, which implies that

$$\theta_n = \sin^{-1}\left(\frac{k_n}{k_0}\right), \quad (35)$$

where θ_n is the discretely sampled angle from the horizontal (positive down) associated with each wavenumber within the bounds $|k_n| < k_0$. Since the source function is defined for a large sector of wavenumber space, Eq. (35) implies that the source is also generating energy at many vertical angles.

It is also well known (see [31], for example) that the frequency of a continuous wave source moving along the horizontal axis, and received on the same horizontal axis, is related to the transmit frequency by the expression

$$f' = f_T \left(\frac{c - v_r}{c - v_s} \right), \quad (36)$$

where f_T is the original transmit frequency, c is the speed of sound, v_s is the source speed, and v_r is the receiver speed (where the sign of v_s and v_r infers the horizontal direction of motion). If the receiver is stationary, Eq. (35) can be rewritten as

$$f' = f_T \left(\frac{1}{1 - \frac{v_s}{c}} \right) \approx f_T \left(1 + \frac{v_s}{c} \right), \quad (37)$$

where the last approximation is based upon a binomial series expansion. If the source is also moving at an angle ϕ_s to the horizontal, and we are interested in the component of transmission along the angle θ relative to horizontal, then the general expression for the frequency is

$$f' \approx f_T \left(1 + \frac{v_s}{c} \cos(\theta - \phi_s) \right). \quad (38)$$

This can be generalized for all transmission angles θ_n by the expression

$$f_n' \approx f_T \left(1 + \frac{v_s}{c} \cos(\theta_n - \phi_s) \right), \quad n = 1, 2, \dots, N_z. \quad (39)$$

Equations (35) and (39) define a relationship between the transmitted frequency and the vertical direction of transmission. Thus, even a single

frequency sinusoidal source will produce energy across a bandwidth of frequencies as a function of direction in the vertical plane when the source is in motion. An example of the spread of frequencies versus wavenumbers and associated angles for a 100 Hz source traveling at 20 knots is illustrated in Fig. 2 for three different source traveling directions, ϕ_s .

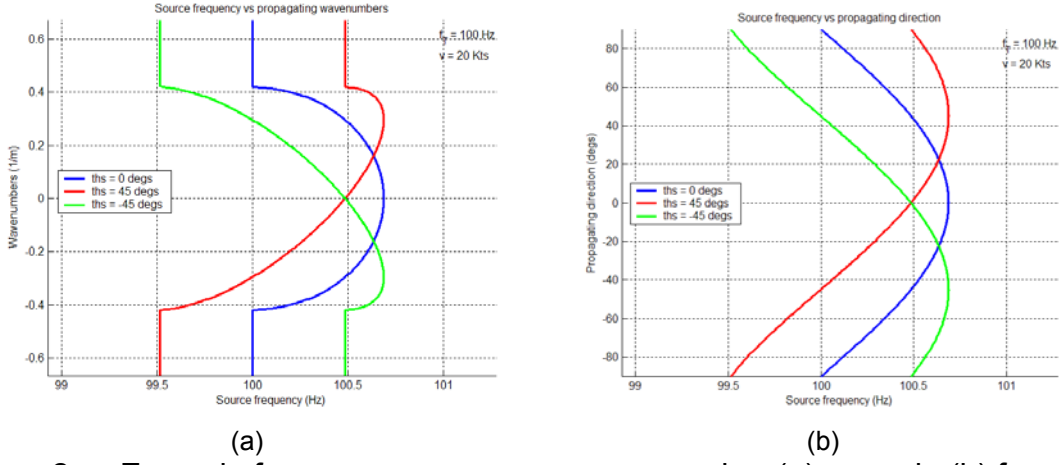


Figure 2. Example frequency response vs wavenumber (a) or angle (b) for a 20 knot source moving at the grazing angles 0° (blue), 45° (red), or -45° (green) from the horizontal

Numerical implementation of this effect requires distribution of the source function defined in (34) onto a discrete grid having coordinates of wavenumber versus frequency. We performed this distribution using a nearest neighbor rule followed by linear interpolation. The process begins by the following discrete assignments:

$$\psi'(r=0, k_n, f_i) = \begin{cases} \alpha \cdot \psi(r=0, k_n) & , \quad f_i \leq f_n' < f_{i+1} \\ (1 - \alpha) \cdot \psi(r=0, k_n) & , \quad \text{otherwise} \end{cases} \quad (40)$$

where f_i represents the discrete frequency grid for which the PE field is evaluated, and f_n' is defined by Eq. (39). Also α is a mixing parameter that was nominally set to 0.9995 in the M3PE implementation to provide approximately 66 dB of cell attenuation.

The grid frequencies are defined as

$$f_i = f_T - \frac{N_f}{2} \Delta f + (i-1) \Delta f \quad , \quad i = 1, 2, \dots, N_f , \quad (41)$$

where

$$\Delta f = (f_{\max} - f_{\min}) / N_f , \quad (42)$$

$$f_{\max} = \max(f_n') , \quad (43)$$

$$f_{\min} = \min(f_n') \quad \forall n = 1 \dots N_z . \quad (44)$$

Here, N_f is the number of frequency cells and $n=1, 2, \dots, N_z$ defines the index of k_n .

Each cell is then smoothed across two adjacent frequency bins using linear interpolation. That is, for each bin where $f_i \leq f_n' < f_{i+1}$, the complex source amplitudes $\psi'(r=0, k_n, f_i)$ and $\psi'(r=0, k_n, f_{i+1})$ and $\psi'(r=0, k_n, f_{i-1})$ are modified as follows:

$$\psi'(f_{i-1}) = \begin{cases} \psi'(f_n') \left[1 - \frac{(f_n' - f_{i-1})}{\Delta f} \right] & , \quad f_i > f_n' \\ \psi'(f_{n-1}') & , \quad f_i \leq f_n' \end{cases} , \quad (45)$$

$$\psi'(f_i) = \psi'(f_n') \left[1 - \left| \frac{(f_n' - f_i)}{\Delta f} \right| \right] , \quad (46)$$

$$\psi'(f_{i+1}) = \begin{cases} \psi'(f_n') \left[1 - \frac{(f_{i+1} - f_n')}{\Delta f} \right] & , \quad f_i \leq f_n' \\ \psi'(f_{n+1}') & , \quad f_i > f_n' \end{cases} , \quad (47)$$

where the dependencies upon r and k_n are dropped for simplicity.

It is also noted that any constraints on the directional response, as required (for example) to represent transmission from a phased array, can be accommodated by simply scaling the source function along the k_n axis by a weight vector that is the inverse Fourier Transform of the desired vertical beam pattern.

C. INCORPORATING RECEIVER MOTION

As pointed out by Smith,¹⁹ the influence of receiver motion cannot be represented by a simple one-time reshuffling of the start-up function across a frequency grid, as described for the source motion case (see Eqs. 44-46). This is because the effects of receiver motion will vary at each range step, and because an analytical form of the pressure response is no longer available after the source has propagated through the medium. Any realization of the frequency-dependent transmission loss at a particular range and depth must wait until the source function propagates through the medium. Since the propagated field is only defined numerically, receiver motion can also only be represented with a numerical approach.

The goal of the algorithm is to remap the pressure response in the wavenumber domain at each range onto a new coordinate axis representing the moving receiver. This mapping can be implemented by a bulk shift and fine interpolation of the complex wavenumber spectra in the positive frequency direction for a closing receiver, or in the negative frequency direction for an opening receiver. A separate interpolation across frequency must be performed at each wavenumber, since the amount of shifting will change in a manner similar to the plots presented in Fig. 2a.

To describe the interpolation procedure, let us first define a new frequency axis that accounts for both source and receiver motion

$$f_i'' = f_T - \frac{N_f}{2} \Delta f'' + (i-1) \Delta f'' \quad , \quad i = 1, 2, \dots, N_f \quad , \quad (48)$$

where

$$\Delta f'' = (f''_{\max} - f''_{\min}) / N_f \quad . \quad (49)$$

Here, the maximum and minimum frequencies have been adjusted to account for the max and min Doppler shift associated with receiver motion. The Doppler shifts for each wavenumber, ΔF_n and their extrema, ΔF_{\min} and ΔF_{\max} , are defined as

$$\Delta F_n = f_r \frac{|v_r|}{c_0} \cos(\theta_n - \phi_r) \quad , \quad (50)$$

$$\Delta F_{\min} = \min_n(\Delta F_n) \quad , \quad (51)$$

$$\Delta F_{\max} = \max_n(\Delta F_n) \quad \forall n = 1 \dots N_z \quad , \quad (52)$$

where v_r is the speed of the receiver, and ϕ_r is its direction relative to grazing.

The maximum or minimum frequency shifts are used to modify the edge values of the new frequency axis depending on the direction of receiver motion (i.e., positive away from the source or negative towards the source), as indicated by

$$f''_{\max} = \begin{cases} f_{\max} + \Delta F_{\min} & , \quad v_r < 0 \\ f_{\max} & , \quad \text{otherwise} \end{cases} \quad , \quad (53)$$

$$f''_{\min} = \begin{cases} f_{\min} + \Delta F_{\max} & , \quad v_r > 0 \\ f_{\min} & , \quad \text{otherwise} \end{cases} \quad , \quad (54)$$

where f_{\min} and f_{\max} were defined previously in Eqs. (43) and (44) for the zero receiver speed case, and ΔF_{\min} and ΔF_{\max} are defined by Eqs. (51) and (52).

Given the new frequency axis, a new PE field in the wavenumber domain can be generated from the following interpolation across frequency,

$$\psi''(j\Delta r, k_n, f_i'') = \sum_{m=1}^M \psi'(j\Delta r, k_n, f'_{i+B_n+m-1}) \cdot h_{n,i}(m) \quad , \quad (55)$$

where B_n is an integer shift in frequency for each wavenumber k_n , and $h_{n,i}(m)$ are the coefficients of a filter whose group delay is equivalent to the remainder between the actual required frequency shift and the bulk shift B_n . The B_n values are defined as $B_n = \text{FLOOR}[\Delta F_n]$, using the MATLAB command as an operator. The coefficients of $h_{n,i}(m)$ can be designed using procedures similar to those applied to time domain interpolative beamforming. For the case of a two coefficient linear interpolator (used in our implementation), the values of $h_{n,i}(m)$

can be deterministically defined as

$$h_{n,i}(1) = 1 , \quad (56a)$$

$$h_{n,i}(2) = \frac{\psi'(j\Delta r, k_n, f'_{i+B_n+1}) - \psi'(j\Delta r, k_n, f'_{i+B_n})}{\Delta f} \frac{(f''_i - f'_{i+B_n+1})}{\psi'(j\Delta r, k_n, f'_{i+B_n+1})} . \quad (56b)$$

It is again noted that the interpolation is performed separately across the frequency axis for each discrete wavenumber coordinate at each range cell. It is also noted that the values $\psi''(j\Delta r, k_n, f''_i)$ represent the final output field, but the un-interpolated field $\psi'(j\Delta r, k_n, f'_i)$ is propagated to the next range within the marching loop.

THIS PAGE INTENTIONALLY LEFT BLANK

III. M3PE IMPLEMENTATION DETAILS

To complete our description of the propagation model, we also need to discuss approaches to handling a variety of implementation details. These include a) taper functions to handle finite computational depths, b) transition functions for sound speed and density discontinuities at the interface between water and the bottom, c) incorporation of attenuation, d) options for bottom roughness, e) rules of thumb for range and depth mesh size resolutions, and f) known limitations of the current M3PE implementation. Many of the limitations stated here have already been implemented in Smith's MMPE model, so incorporating them into the MATLAB version is fertile territory for future upgrades.

A. TAPER FUNCTIONS

In the M3PE implementation, the computational depth, z_{\max} , is nominally twice the maximum water depth, z_w . To minimize the effects of energy propagating at very deep sub-bottom depths, or from very steep vertical angles, a filter is applied to both the wavenumber (KE) and depth (PE) propagators. A depth filter is applied to ensure that the field amplitude approaches zero at the maximum computational depth (below the bottom of the water column), consistent with the far-field radiation boundary condition, $p(z \rightarrow \infty) \rightarrow 0$. Smith²⁰ points out that the filter must be a smooth function to avoid generating higher order spectral terms during Fourier transformation from the abruptness of the filter itself. According to Smith,²⁰ it is desired that the filter begin its taper approximately 1/3 of the distance from the z_{\max} . A function that creates the desired affect is defined as

$$G(z) = \frac{1}{4} (1 - \cos(\Omega_i)) + \frac{1}{2}, \quad (57)$$

with

$$\Omega_i = \min\left(\pi, \frac{6\pi i}{N_z}\right) \quad i = \frac{N_z}{2}, \frac{N_z}{2}-1, \dots, 2, 1 . \quad (58)$$

As defined previously, N_z is the size of the Discrete Fourier Transform (DFT). In the model implementation, the depth propagator $U(z)$ (see Eq. (17)) is multiplied by $G(z)$ at a one-time initialization step. The filter is then repeatedly applied at each range step, resulting in severe attenuation of the deepest depths after several updates of the marching loop. A plot of the depth taper function is shown in Fig. 3a.

To restrict propagation at very steep angles (where the PE approximation is not valid) a separate function is applied to the wavenumber propagator $\hat{T}_{OP}(k_z)$ (see Eq. (20)) of the form

$$E(n) = \frac{1}{2} (1 + \cos(\Theta_n)) \quad , \quad n = 1, 2, \dots, \frac{N_z}{2} \quad , \quad (59)$$

where

$$\Theta_n = \pi \times \begin{cases} \frac{\left(\frac{k_n}{k_0} - \sin(\theta_{\min})\right)}{\left(\sin(\theta_{\max}) - \sin(\theta_{\min})\right)} & , \quad \frac{k_n}{k_0} < \sin(\theta_{\max}) \& \frac{k_n}{k_0} > \sin(\theta_{\min}) \\ 1 & , \quad \frac{k_n}{k_0} \geq \sin(\theta_{\max}) \\ 0 & , \quad \frac{k_n}{k_0} \leq \sin(\theta_{\min}) \end{cases} \quad (60)$$

with the control parameters nominally defined as $\theta_{\min} = 80^\circ$ and $\theta_{\max} = 90^\circ$.

These parameters result in a very sharp transition function as illustrated in Fig. 3b. This, according to Smith,²⁰ provided the best results during benchmark testing. A smaller value for θ_{\min} would result in a smoother response but would not excite the higher angles of propagation as well.

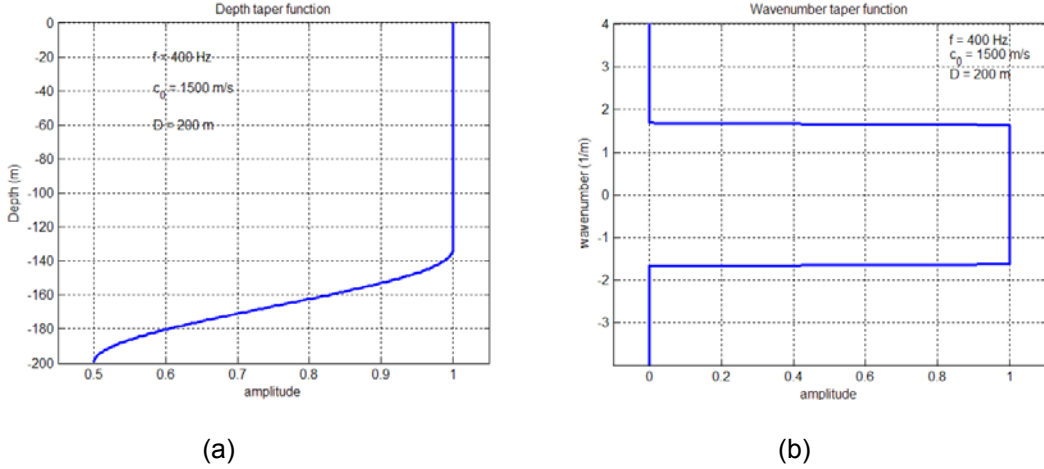


Figure 3. Examples of a depth taper (a) and wavenumber taper (b) for the case $f=100$ Hz, $c_0=1500$ m/s, and $D=200$ m

B. BOTTOM TRANSITION FUNCTIONS

When using a Discrete Fourier Transform to perform a spectral decomposition, it is standard practice to smooth any sharp amplitude transitions in the data to avoid creating harmonic components representing the true Fourier Series of any finite width envelope. In the case of the split-step marching algorithm, these “harmonics” would be observed as sidelobes along the depth axis. In the parametric data representing an acoustic environment, it is likely that a sharp transition will occur in the sound speed and density values at the water-bottom interface. In Smith’s MMPE and our M3PE implementation, a separate transition function is applied to the sound speed and the density. For the speed of sound, the transition function is defined as

$$H_c(\zeta) = \left(1 + e^{-\frac{\zeta}{L_c}} \right)^{-1}, \quad (61)$$

where

$$\zeta = z - z_b, \quad (62)$$

and

$$L_c = \max\left(\frac{\lambda}{10}, \Delta z\right). \quad (63)$$

Note that the maximum function in Eq. (63) enforces the constraint that $L_c \geq \Delta z$. $H_c(\zeta)$ has the following properties:

$$H_c(\zeta) = \begin{cases} \rightarrow 0 & , \quad z < z_b \\ 0.5 & , \quad z = z_b \\ \rightarrow 1 & , \quad z > z_b \end{cases} . \quad (64)$$

The transition function in Eq. (61) is applied to the sound speed at each range about the bottom depth according to

$$c(z, r) = c(z, r) + (c_b - c_w) \cdot H_c(z - z_b) . \quad (65)$$

A different function, having similar properties to H_c , is applied to the density data. This transition function is a cubic spline defined as

$$H_\rho(\zeta) = \begin{cases} 1 & , \quad \zeta < -L_\rho \\ \frac{2}{3} \left(1 + \frac{\zeta}{L_\rho}\right)^3 & , \quad -L_\rho \leq \zeta < \frac{-L_\rho}{2} \\ \frac{1}{2} + \frac{\zeta}{L_\rho} - \frac{2}{3} \left(\frac{\zeta}{L_\rho}\right)^3 & , \quad \frac{-L_\rho}{2} \leq \zeta < \frac{L_\rho}{2} \\ 1 - \frac{2}{3} \left(1 - \frac{\zeta}{L_\rho}\right)^3 & , \quad \frac{-L_\rho}{2} \leq \zeta < L_\rho \\ 1 & , \quad \zeta \geq L_\rho \end{cases} , \quad (66)$$

where

$$L_\rho = \max(2\lambda, 2\Delta z) . \quad (67)$$

$H_\rho(\zeta)$ is applied to the density parameters $\rho(z, r)$ using Eq. (65) with the density and density transition function substituted for the appropriate sound speed related parameters. According to Smith,²⁰ H_ρ was chosen to be a continuously defined function to guarantee the existence of its second derivative. Recall that the propagator U_2 in Eq. (29) is proportional to $H_\rho''(z - z_b)$, i.e. the second derivative of the transition function. Smith defined this function as

$$H''_\rho(\zeta) = \begin{cases} 0 & , \quad \zeta < -L_\rho \\ \frac{4}{L_\rho^2} \left(1 + \frac{\zeta}{L_\rho} \right) & , \quad -L_\rho \leq \zeta < \frac{-L_\rho}{2} \\ \frac{-4}{L_\rho^2} \left(\frac{\zeta}{L_\rho} \right) & , \quad \frac{-L_\rho}{2} \leq \zeta < \frac{L_\rho}{2} \\ \frac{-4}{L_\rho^2} \left(1 - \frac{\zeta}{L_\rho} \right) & , \quad \frac{-L_\rho}{2} \leq \zeta < L_\rho \\ 0 & , \quad \zeta \geq L_\rho \end{cases} \quad (68)$$

Examples of H_c , H_ρ and H''_ρ are plotted in Fig. 4 for a 120 m waveguide at a frequency of 100 Hz.

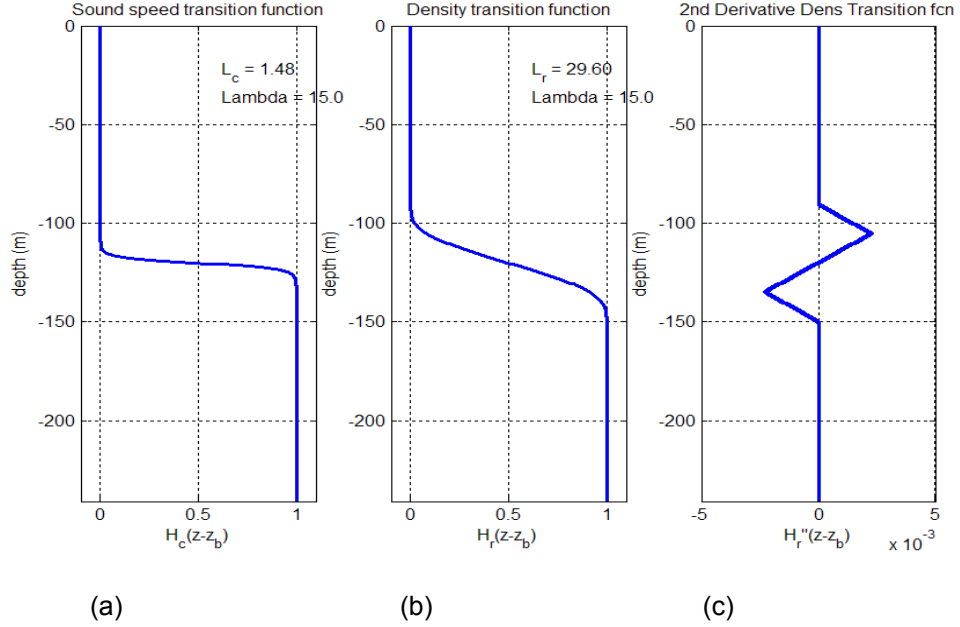


Figure 4. Example water-bottom transition functions for (a) sound speed and (b) density when $\lambda = 15$ m, and (c) 2nd derivative of density function.

C. ATTENUATION

Attenuation is implemented by adding an exponential damping term to the depth propagator function used in the PE marching algorithm, specifically

$$\psi(r + \Delta r, z) = e^{-ik_0 \frac{\Delta r}{2} U_{OP}(r + \Delta r, z) - \frac{\Delta r}{2} \alpha(r + \Delta r, z)} \times IDFT \left\{ e^{-ik_0 \Delta r \hat{T}_{OP}(k_z)} \times DFT \left[e^{-ik_0 \frac{\Delta r}{2} U_{OP}(r, z) - \frac{\Delta r}{2} \alpha(r, z)} \times \psi(r, z) \right] \right\}, \quad (69)$$

where $\alpha(r,z) = \mathbf{a}(r,z)/8.686$, in units of nepers, and \mathbf{a} is the attenuation in units of dB/m.

The attenuation is defined separately for the water column versus the bottom layer. In the water, our implementation employs the Fisher-Simmons model as defined by Kinsler, et al.,³² given by

$$\mathbf{a}(r,z) = \left[\frac{A}{(f_1^2 + f^2)} + \frac{B}{f_2^2 + f^2} + C \right] \frac{f^2}{1000} \quad \text{in dB/m ,} \quad (70)$$

where

$$A = 0.083 \left(\frac{S}{35} \right) e^{\left(\frac{T}{31} \right) - \left(\frac{Z_a}{91} \right) + 1.8(pH - 8)} , \quad (71)$$

$$B = 22 \left(\frac{S}{35} \right) e^{\left(\frac{T}{14} \right) - \left(\frac{Z_a}{6} \right)} , \quad (72)$$

$$C = (4.9 \times 10^{-10}) e^{-\left(\frac{T}{26} \right) - \left(\frac{Z_a}{25} \right)} , \quad (73)$$

$$f_1 = 780e^{\frac{T}{29}} , \quad f_2 = 42000e^{\frac{T}{18}} , \quad \text{and} \quad (74)$$

$$Z_a = \frac{D}{2} . \quad (75)$$

Although subscripts were omitted for convenience, the environmental parameters T (temperature in $^{\circ}\text{C}$), S (salinity in ppm), and pH (acidity coefficient, dimensionless) are allowed to be range-dependent. However, in the current implementation of M3PE, only a single value of T , S , and pH is used to compute attenuation in the entire water column at each range cell. In the bottom layer, the attenuation is simply defined as a range dependent constant, $a'(r,z)$, in terms of dB/λ . This is converted to dB/m according to

$$\mathbf{a}(r,z) = a'(r,z) \frac{f}{c(r,z)} . \quad (76)$$

D. BOTTOM ROUGHNESS

The M3PE implementation allows the mean ocean depth versus range to be modified by a range-dependent roughness function. Several options implemented in M3PE include a zero mean Gaussian and uniform random perturbation with a user defined RMS height. The better option is based upon the original work of Fox and Hayes³³ where the seafloor roughness is modeled with an isotropic, zero mean, magnitude spectrum that follows a power law. Our implementation is based upon the description given by Smith³⁴ as outlined below.

First define the envelope of a roughness spectrum having the form

$$W(n) = \frac{\sigma}{(1 + L_{cor}^2 \kappa^2)^{\beta}}, \quad n = 1, 2, 3, \dots, N_r, \quad (77)$$

where L_{cor} is a correlation length, κ_n is the horizontal wavenumber, N_r is the number of range cells, and β is a power constant that is usually set to the value of 3.5. The spectral envelope is converted into a bottom depth perturbation by using Eq. (77) to factor a complex exponential with a Gaussian amplitude and uniform phase. To illustrate, let

$$S(n) = \sqrt{W(n)} A_n e^{i\theta_n \Delta\kappa}, \quad n = 1, 2, 3, \dots, N_r, \quad (78)$$

where A_n is a standardized Gaussian random variable with zero mean and unit standard deviation (i.e., $N(0,1)$), θ_n is a uniform random variable between the interval $[0,1]$, and $\Delta\kappa$ is the wavenumber cell resolution equal to $2\pi/R_{max}$. R_{max} is the length of the range interval. Then the spectrum function is transformed into a range dependent vector by

$$\xi'(j) = \sum_{n=1}^{N_r} S(n) e^{-i \frac{2\pi}{N} (n-1)(j-1)}, \quad j = 1, 2, 3, \dots, N_r. \quad (79)$$

Next, Eq. (79) is normalized and scaled to result in the final perturbation vector,

$$\xi(j) = \frac{\xi'(j) \cdot \sigma}{\left(\sum_{n=1}^N W^2(n) \right)^{\frac{1}{2}}}, \quad j = 1, 2, 3, \dots, N_r. \quad (80)$$

where σ is a user defined scale factor.

The perturbation vector specified by Eq. 80 is the same length as the range grid. This vector is added to the mean bottom depth at each discrete range to result in a “roughened” bottom. Thus the range resolution imparts a lower limit on the granularity of roughness features. An example of a roughness vector computed for a point set of parameters is shown in Fig. 5.

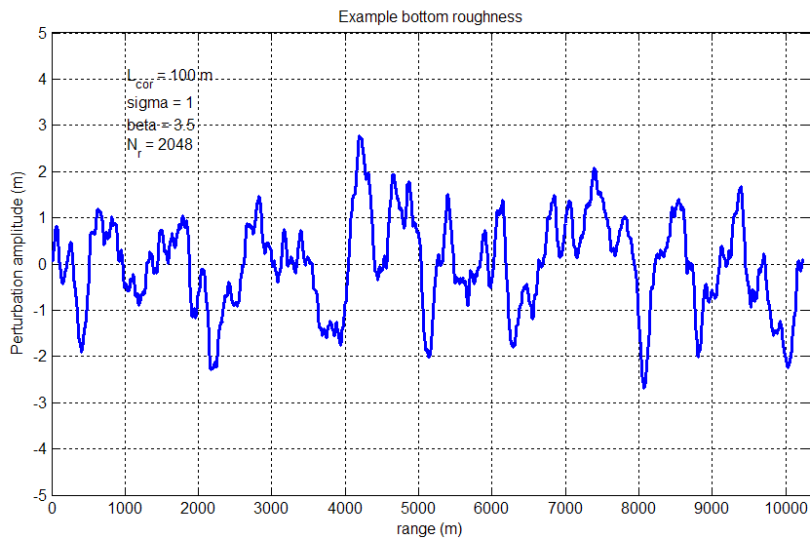


Figure 5. Example Bottom Roughness

E. RANGE AND DEPTH MESH SIZES

In reference [20], Smith evaluated the convergence properties of various depth and range mesh sizes for various benchmark problems. It was found that optimal performance was obtained with the approximate scales

$$\Delta z \approx \frac{\lambda}{10}, \quad (81)$$

$$\Delta r \approx \lambda. \quad (82)$$

where λ is the signal wavelength.

The requirement for depth resolution is dominated by the sound speed mixing length definition, which is $\max(\Delta z, \lambda/10)$. Any depth-mesh size greater than $\lambda/10$, will further increase the transition distance of the sound speed at the bottom, thereby causing inaccuracies in the model solution. The range step size appears to be determined by the “optimal” amount of phase information that is propagated at each step in the marching algorithm. Too large a step size causes errors due to stationarity limits, while too small a step size introduces errors associated with numerical accuracy²⁰. Chapter IV will show examples of performance on benchmark environments for various range step sizes.

F. LIMITATIONS OF M3PE IMPLEMENTATION

It is important to note that the M3PE code does not implement all the features in Smith’s original MMPE code, as well as a variety of other useful capabilities that could be included in future upgrades. This section contains a short description of these limitations.

Currently, the M3PE code only supports the modeling of a sinusoidal source signal. Signals with other spectral shapes could easily be incorporated by upgrading the source definition function to create the broadband signal and appropriately adjusting each frequency component to reflect the required Doppler at each propagating wavenumber. The current MMPE model supports a broadband spectrum with the shape of a Hanning envelope.

Next, the bottom fluid model in M3PE currently does not represent the effects of shear. As noted by Smith²⁰, this can be accomplished by creating an effective density and attenuation that includes the shear sound speed, c_s , and shear attenuation, α_s , parameters. Another feature not supported by M3PE is any treatment of radial coupling. Currently, only a single radial (range versus depth) response is generated.

Also, no accommodation is provided for more than one bottom layer. Sometimes, it is desirable to represent a “slow” sediment layer above a hard (i.e.,

fast) sub-bottom layer. This can be implemented by applying the discontinuity functions for sound speed and density to the transition regions at the water/sediment depths as well as at the sediment/sub-bottom interface.

Finally, no allowance has been made for surface roughness. One technique, first introduced by Dozier³⁵, is based upon a conformal mapping algorithm that transforms the depth variant variables (e.g., $c(r,z)$, $\rho(r,z)$) normally affected by the variable surface height, into a pseudo-space that has a flat surface. In the SSF method, the parameters in the pseudo-space are used to propagate the solution for one range step, and then inverted back to physical space for the next iteration. The result is a propagated field resulting from a single realization of an irregular surface. Another technique presented by Tappert and Nghiem-Phu³⁶ uses the method of images to solve the PE with an rough surface. Either of these methods would be a prime candidate for future upgrades.

IV. M3PE APPLIED TO BENCHMARK CASES

Prior to using the M3PE code to investigate the frequency spread of sinusoidal signals in the presence of motion, the performance of the M3PE model was validated against a set of known test cases. A well documented and sufficiently challenging set of benchmark environments is conveniently available from the website associated with the Shallow Water Acoustic Modeling workshop held in 1999 (a.k.a. SWAM'99)³⁷. Several of the SWAM'99 environments were processed and compared to results generated by Smith using the original MMPE code, and by Mikhin who used an energy conserving implicit finite difference (IFD) PE model³⁸. The IFD models are generally considered to be more accurate than SSF algorithms because of their higher order treatment of the bottom interface boundary condition.²⁰ Our intention is to demonstrate close agreement between the M3PE and MMPE implementations, as well as to make general comments regarding how well either SSF implementation approaches the performance of an IFD method. Since our intention here is to validate the execution of the core SSF PE implementation, both the source and the receiver have zero speed in all the examples in this chapter.

A. TRANSMISSION LOSS FOR FLATa

The first environment, called FLATa, is characterized by a flat bottom and a constant sound speed (c_w) and density (ρ_w) in the water column. A ray trace illustrating iso-speed propagation in the water column for the FLATa environment is shown in Fig. 6, with a source depth of 30 m. The bottom parameters for this case are quite range-dependent along a 20 km radial distance. Illustrations of the range-dependent bottom parameters including bottom sound speed (c_b), gradient of bottom sound speed ($\partial c_b / \partial z$) and bottom density (ρ_b) are plotted in Fig. 7. The attenuation is zero in the water column (α_w), and is a constant 0.1 dB/λ in the bottom (α_b). The shear sound speed (c_s) and attenuation (α_s) were assumed to

be zero. A color coded representation of sound speed, density and attenuation versus range and depth is provided in Fig. 8. It can be observed that the attenuation values follow the shape of the bottom sound speed to maintain a constant loss per wavelength. A summary of all parameters is given in Table 1.

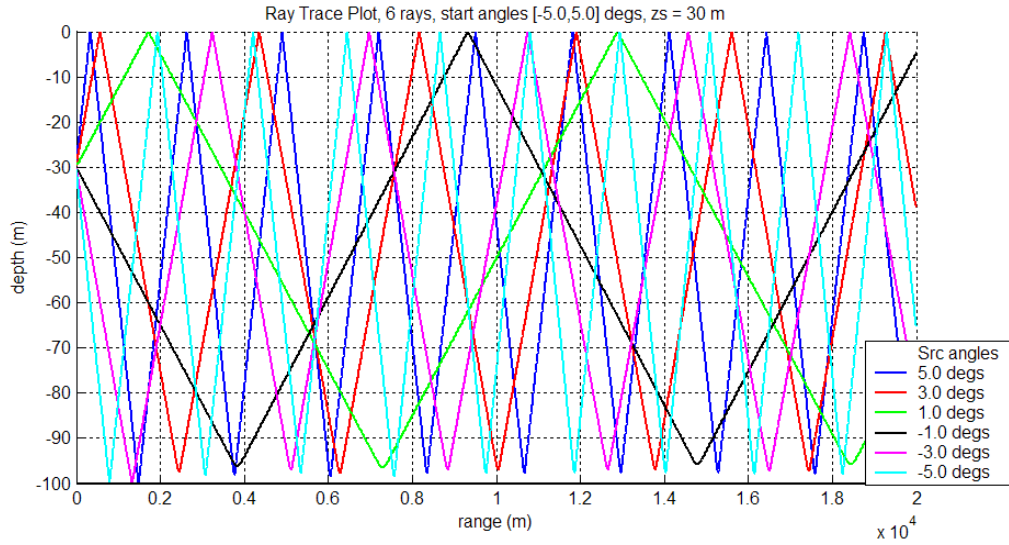


Figure 6. Ray trace in water column for the FLATA environment, $z_s = 30$ m

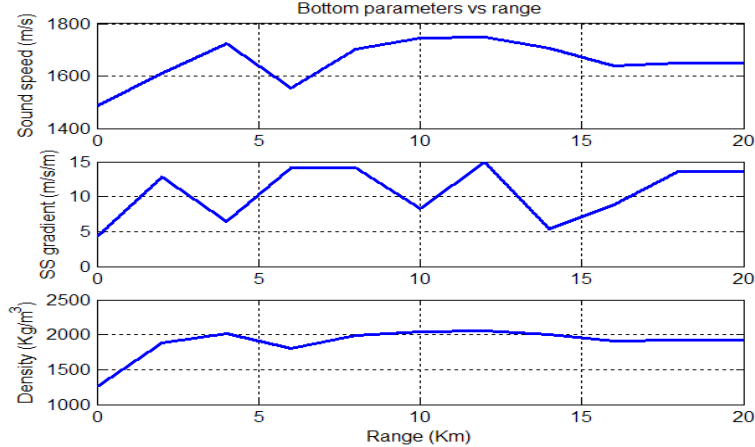


Figure 7. Bottom parameters vs range for the FLATA environment

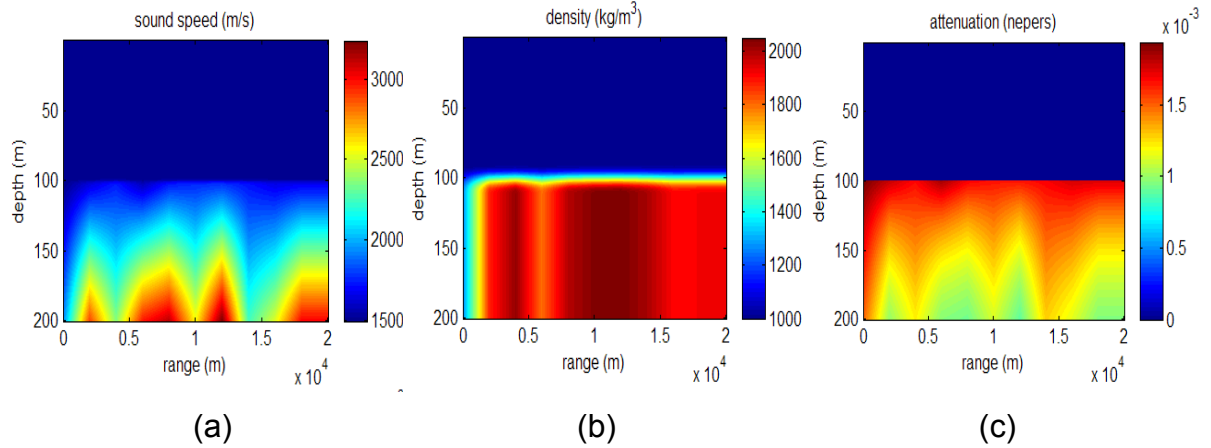


Figure 8. (a) Sound speed, (b) density, and (c) attenuation vs range and depth for the FLATa environment

Table 1. Environmental parameters for the FLATa environment

Bottom depth (m)	c_w m/s	ρ_w (kg/m^3)	α_w dB/ λ	c_b m/s	$\frac{\partial c_b}{\partial z}$ m/s/m	ρ_b (kg/m^3)	α_b dB/ λ	c_s m/s	α_s dB/ λ
100	1500	1000	0.0	variable	variable	variable	0.1	0.0	0.0

An example transmission loss (TL) from the M3PE model computed for the FLATa environment at 250 Hz is shown in Fig. 9. The operating parameters such as DFT size (N_z), number of range cells (N_r), computational depth (z_{\max}), and source depth (z_s) are listed beside the range vs depth plot. At 250 Hz, the wavelength (λ) is about 6 m. Thus the range resolution (5.0 m) and depth resolution (0.195 m) are close to the settings recommended by Smith²⁰ as defined in Eqs. (81) and (82).

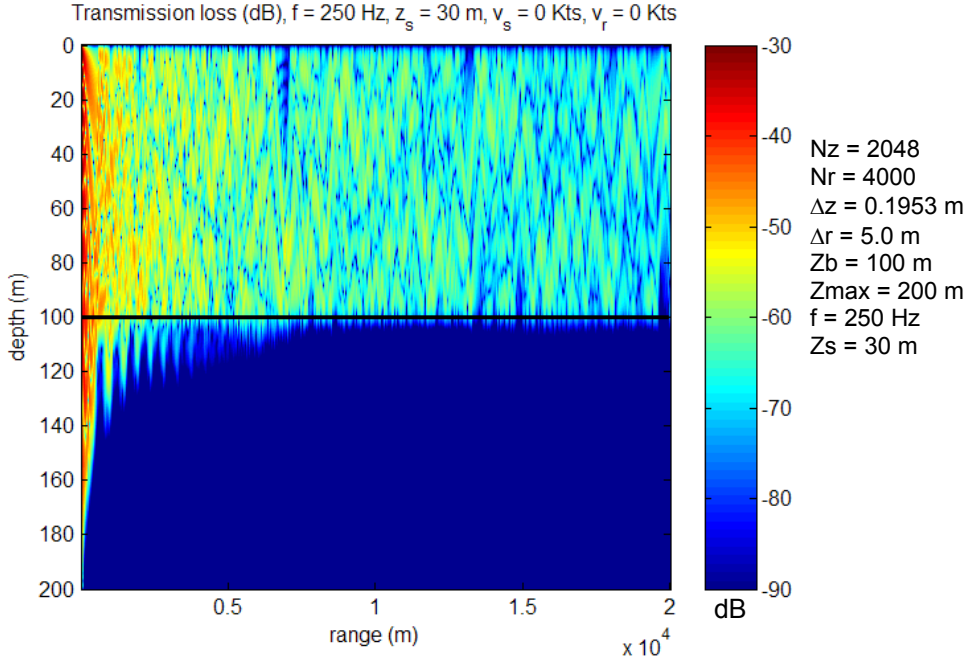


Figure 9. Transmission loss vs range and depth at 250 Hz for the FLATA environment

A comparison of the TL generated by M3PE, MMPE, and the IFD models is plotted in Fig. 10 for a 250 Hz source frequency, a source depth of 30 m, and a receiver depth of 35 m. The top plot in Fig. 10 is TL for the entire 20 km range. The second plot is an expansion of the first 5 km while the third plot is an expansion of the last 5 km. It can be observed in Fig. 10 that the M3PE (blue) and MMPE (red) results are very close in the first 5 km and reasonably close at the latter ranges. Also, all three models follow quite closely out to about 2700 m, but somewhat diverge towards the latter ranges. Still the top plot in Fig. 10 illustrates that the general trend of the TL response is very similar even at the longer ranges.

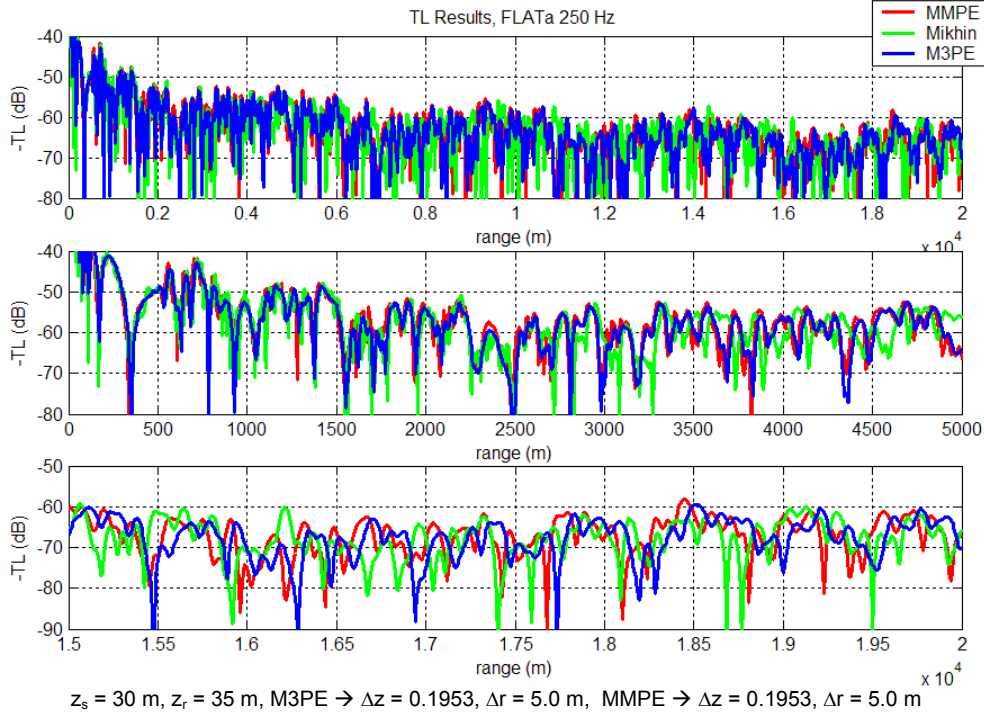


Figure 10. Comparison of transmission loss at 250 Hz between MMPE, Mikhin's IFD, and M3PE PE models for FLATA environment

Figure 11 presents a TL prediction from the M3PE model at 25 Hz. Here $N_z = 256$ and $N_r = 400$, consistent with Smith's guidance regarding grid sizes. It can be observed that significantly more bottom penetration is predicted at this frequency than observed at 250 Hz, as expected. A comparison between TL results generated by the three different models at 25 Hz is plotted in Fig. 12. In this case, the M3PE and MMPE results are quite similar all the way to the maximum range. However, both SSF models differ significantly from the IFD approach after the first 2500 m. Smith¹⁵ explains that this dissimilarity is related to the bottom mixing functions applied to the sound speed and density, which are proportional to either the wavelength or the depth mesh size (see Eqs. (63) and (67)). At low frequencies the mixing functions can be quite wide (in depth) and cause fairly large changes in the actual c_w/c_b and ρ_w/ρ_b parameters near the bottom. For shallow waveguides this can represent a significant deviation. This is a known disadvantage of SSF approaches, and thus limits their effectiveness

when the ocean depth is a very small number of wavelengths.

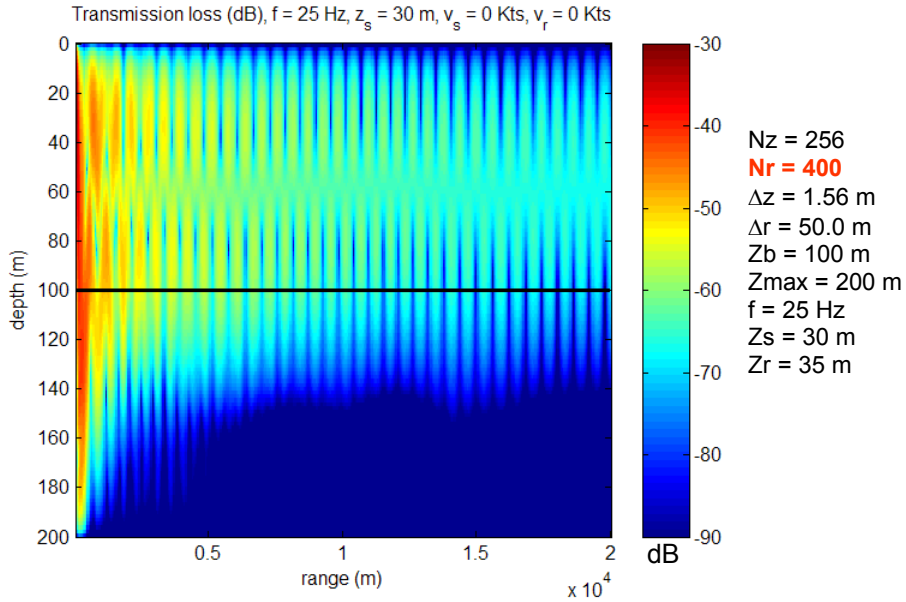


Figure 11. Transmission loss vs range and depth at 25 Hz for the FLATA environment

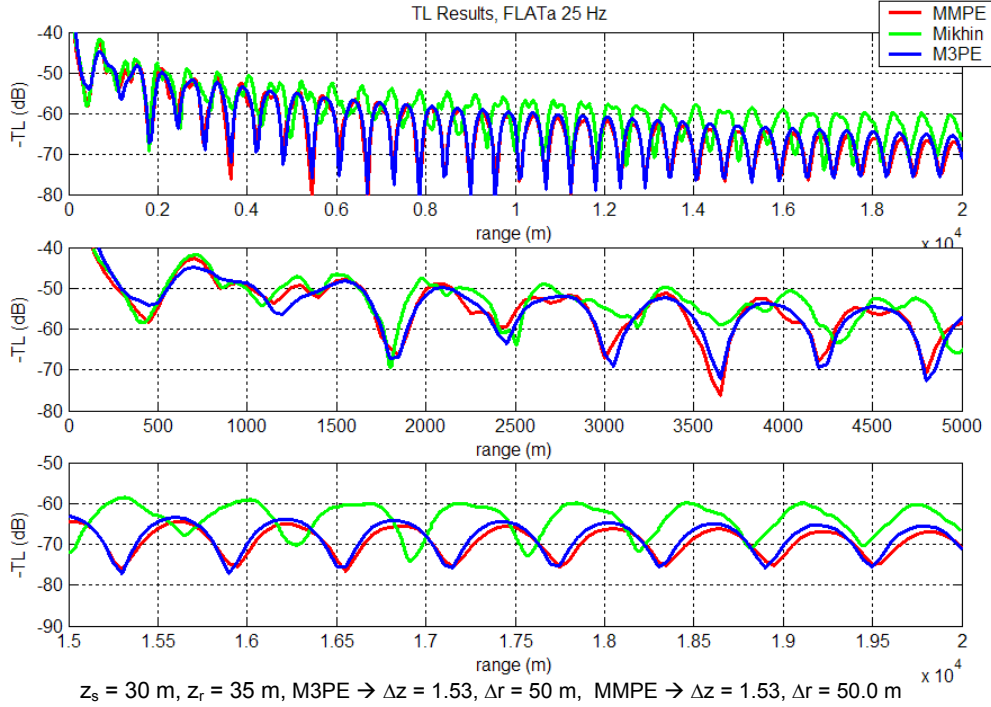


Figure 12. Comparison of transmission loss at 25 Hz between MMPE, Mikhin's IFD, and M3PE PE models for the FLATA environment

Additionally, comparisons were made with the FLATa environment at 1000 Hz. Figure 13 illustrates the 2-D transmission loss and Fig. 14 plots the results at $z_s = 30$ m and $z_r = 35$ m produced by the three different models. Consistent with the 250 Hz case, the TL produced by M3PE and MMPE at 1000 Hz are quite similar, and both follow the general trends generated by the IFD algorithm.

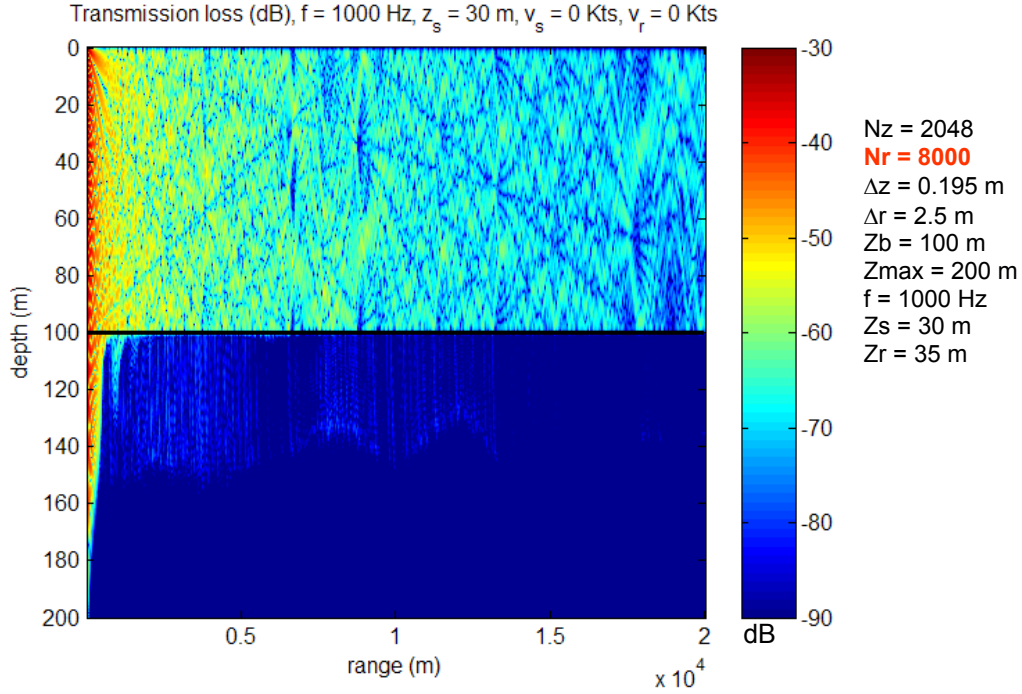


Figure 13. Transmission loss vs range and depth at 1000 Hz for the FLATa environment

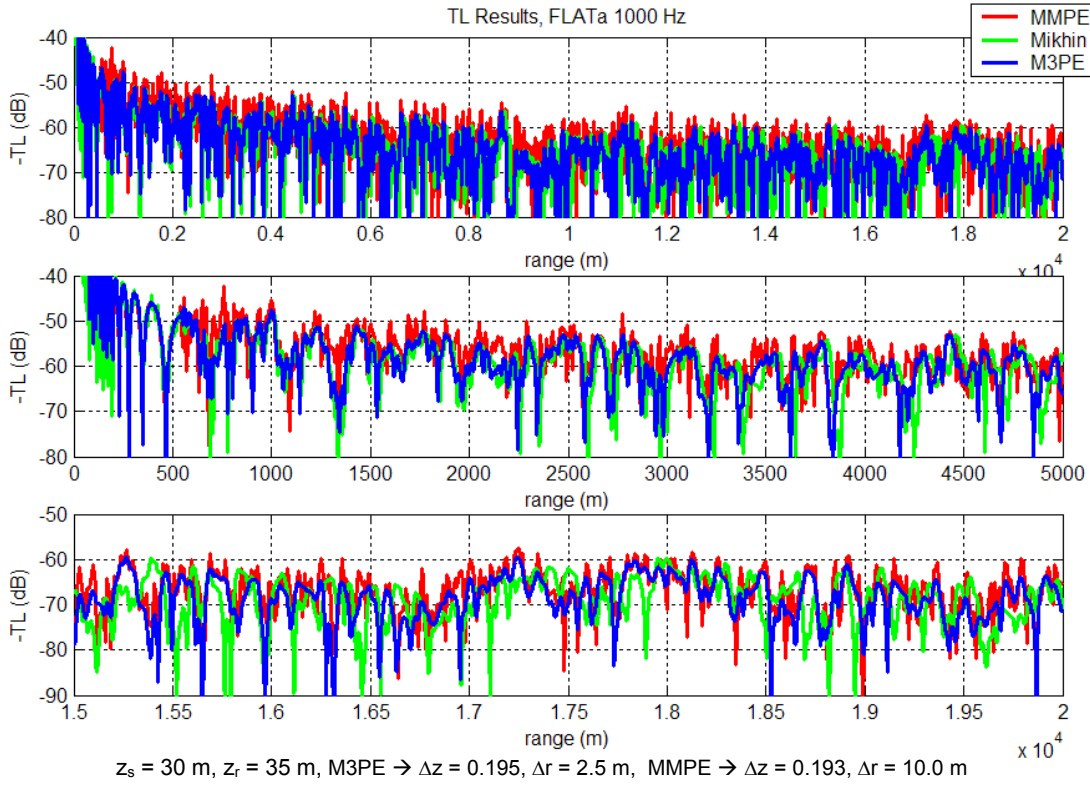


Figure 14. Comparison of transmission loss at 1000 Hz between MMPE, Mikhin's IFD, and M3PE PE models for the FLATA environment

B. CONVERGENCE DEMONSTRATED ON FLATA

The FLATA environment was also used to evaluate the convergence properties of the M3PE code. Here we are specifically interested in the relative performance as a function of the number of range cells (N_r) which determines the range resolution $\Delta r = \frac{R_{\max}}{N_r}$. Smith showed that an SSF PE model can produce significantly different results for various resolutions. This effect is of interest to this study because processor and memory resources can be highly stretched when the number of range cells is large. This is especially important when the model is evaluated across many frequencies, as will be required when we model the effects of source and receiver motion. The following examples demonstrate that the convergence properties of M3PE are similar to the results obtained with

the MMPE implementation. We also show that the guidance provided by Smith²⁰, and restated in Eqs. (81) and (82), is very consistent with the results presented here.

A comparison of TL vs range, in the FLATa environment, using various range resolutions ($\Delta r = 2.5$ m, $\Delta r = 5.0$ m, $\Delta r = 10$ m, $\Delta r = 20$ m) is provided in Fig. 15. Again, the source depth is 30 m and the receiver depth is 35 m. The frequency is 250 Hz, and consequently the wavelength is 6 m. Here we see that a resolution of at least 5 m ($N_r = 2000$) is required for convergence at the longer ranges. This is quite apparent where the TL with the lowest resolution can be several dB different than the TL with the “optimal” resolution. It is interesting that there is not much degradation with lower resolution inside 5 km.

Figure 16 contains a second test case with the FLATa environment at 1000 Hz. The transmission loss is again plotted for the same four resolutions. Here we see that at this higher frequency, with $\lambda = 1.5$ m, there is quite a bit of difference between the TL response using the four different range resolutions. Presumably the more accurate result is when the range resolution closely matches the wavelength (i.e. $N_r = 8000$). Similar to the 250 Hz case, it appears there is a loss of energy when the resolution is less than required. However, there isn’t a dramatic difference until resolution is more than 2-3 times the wavelength.

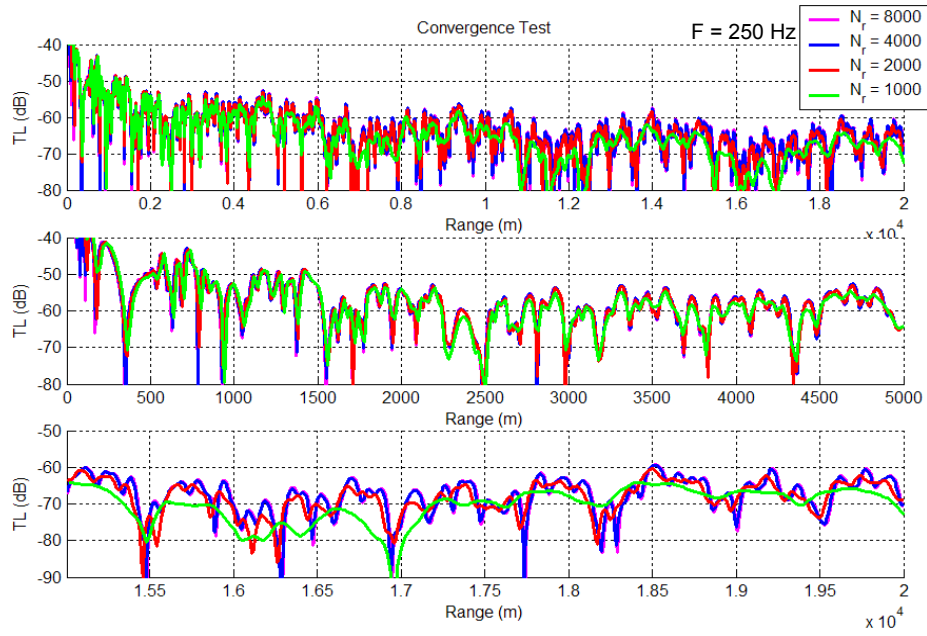


Figure 15. Comparison of M3PE results at 250 Hz for the FLATa environment, $\Delta r = 2.50$ m (magenta), $\Delta r = 5.0$ m (blue), $\Delta r = 10.0$ m (red), $\Delta r = 20.0$ m (green)

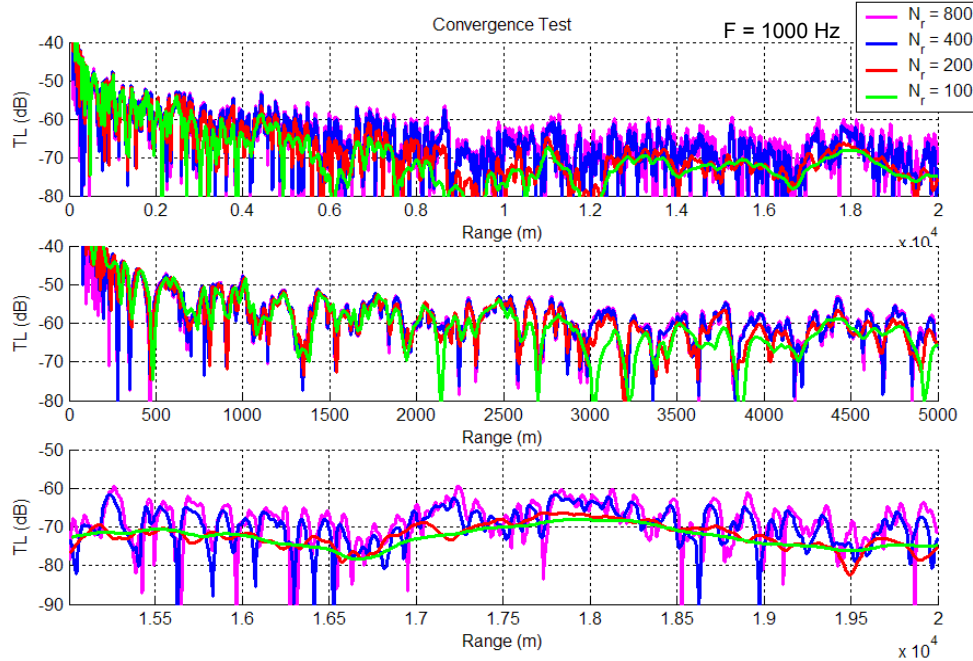


Figure 16. Comparison of M3PE results at 1000 Hz for the FLATa environment, $\Delta r = 2.50$ m (magenta), $\Delta r = 5.0$ m (blue), $\Delta r = 10.0$ m (red), $\Delta r = 20.0$ m (green)

C. RECIPROCITY DEMONSTRATED ON FLATA

The FLATA environment was also used to evaluate the reciprocity characteristics of the M3PE model. Here we evaluated the TL beginning with a source at 30 m and a receiver 20 km away at a depth of 35 m. The frequency is 250 Hz, the depth resolution is 0.1953 m, and the range resolution is 5 m. Here, the TL is propagated from “left to right” across the environment illustrated in Fig. 8. Conversely, another TL is computed starting at a 35 m depth and propagating from right to left across the environment to be received at a depth of 30 m. The TL (level and phase) associated with the last km of distance is plotted on the same axis in Fig. 17. The level and phase at 20 km resulting from propagation across reciprocal paths is practically identical. The performance demonstrated here is fairly similar to the results generated by Smith²⁰.

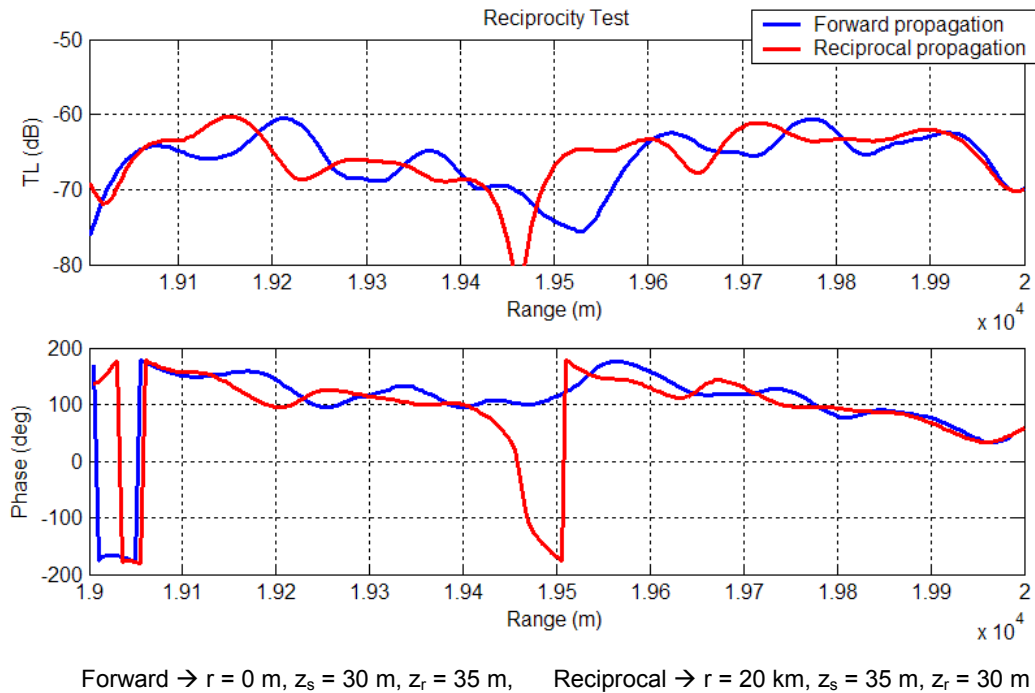


Figure 17. Results of a reciprocity test for the FLATA environment, $f = 250 \text{ Hz}$.
Magnitude of TL (upper) and phase (lower)

D. TRANSMISSION LOSS FOR DOWNa

The second benchmark is called DOWNa. This environment is

characterized by an increasing ocean depth versus range, and a constant sound speed (c_w) and density (ρ_w) in the water column. A ray trace illustrating iso-speed propagation in the water column in a range-dependent waveguide is shown in Fig. 18 with a source depth equal to 30 m. Except for ocean depth, the other bottom parameters such as bottom sound speed (c_b), gradient of bottom sound speed ($\frac{\partial c_b}{\partial z}$), and bottom density (ρ_b) are constant versus range. Also, the attenuation is zero in the water column (α_w), and is a constant 0.1 dB/λ in the bottom (α_b). Again the shear sound speed (c_s) and attenuation (α_s) are zero. A color coded representation of sound speed, density and attenuation versus range and depth for this environment is provided in Fig. 19. As before, the attenuation values follow the shape of the bottom sound speed to maintain a constant loss per wavelength. A summary of all parameters for the DOWNa environment is given in Table 2.

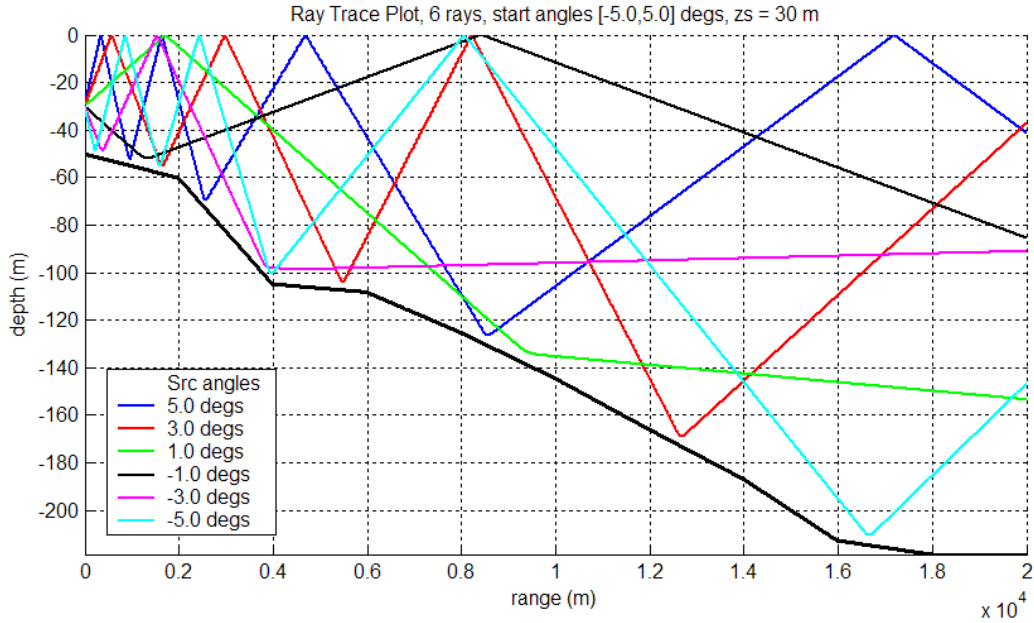


Figure 18. Ray trace in water column for the DOWNa environment, $z_s = 30$ m

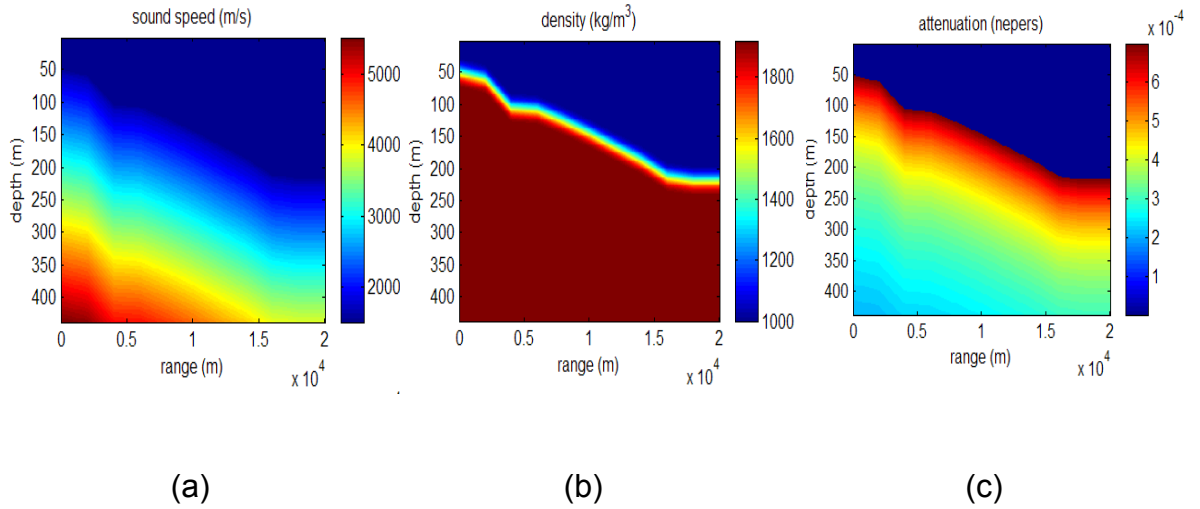


Figure 19. Sound speed (a), density (b), and attenuation (c) vs range and depth for the DOWNa environment

Table 2. Environmental parameters for the DOWNa environment

Bottom depth (m)	c_b m/s	ρ_w (kg/m ³)	α_w dB/λ	c_b m/s	$\partial c_b / \partial z$ m/s/m	ρ_b (kg/m ³)	α_b dB/λ	c_s m/s	α_s dB/λ
variable	1500	1000	0.0	1650	10	1920	0.1	0.0	0.0

An example TL from the M3PE model against the DOWNa environment at 250 Hz is shown in Fig. 20. The operating parameters N_z and N_r are listed beside the TL plot. In this case, the range resolution meets the criterion of Eq. (82), but the depth resolution is approximately double the recommended guidance from Eq. (81). A comparison of the TL at 250 Hz generated by M3PE, MMPE, and the IFD models is plotted in Fig. 21. It can again be observed that the M3PE (blue) and MMPE (red) results are very close in the first 5 km and reasonably close at the latter ranges. Also, the general trend of the TL response from the two SSF methods follows the trend of the IFD approach out to 12 km, except for a few anomalous ranges.

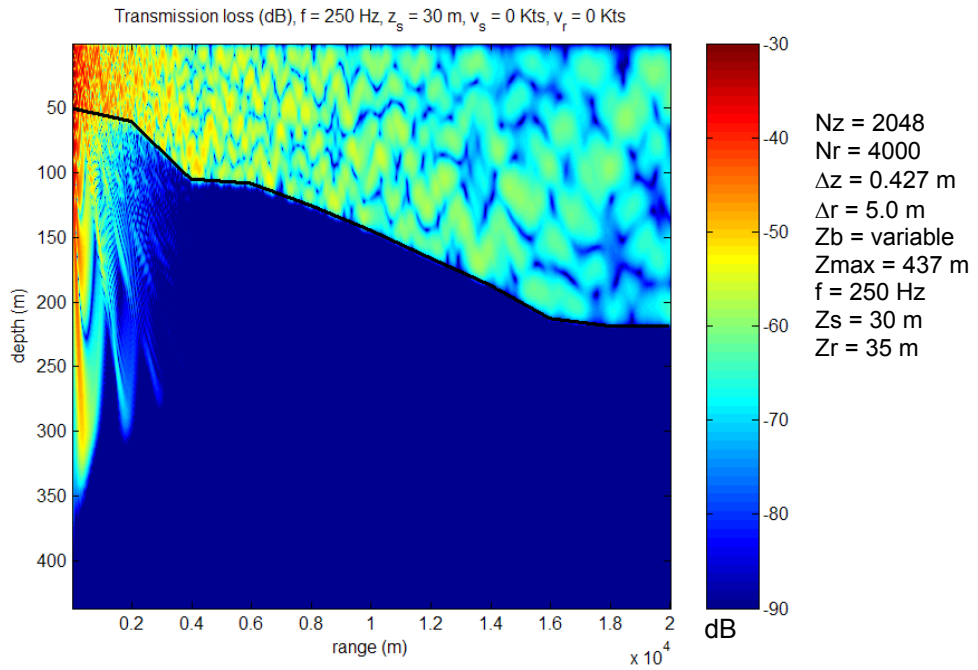


Figure 20. Transmission loss vs range and depth at 250 Hz for the DOWNa environment

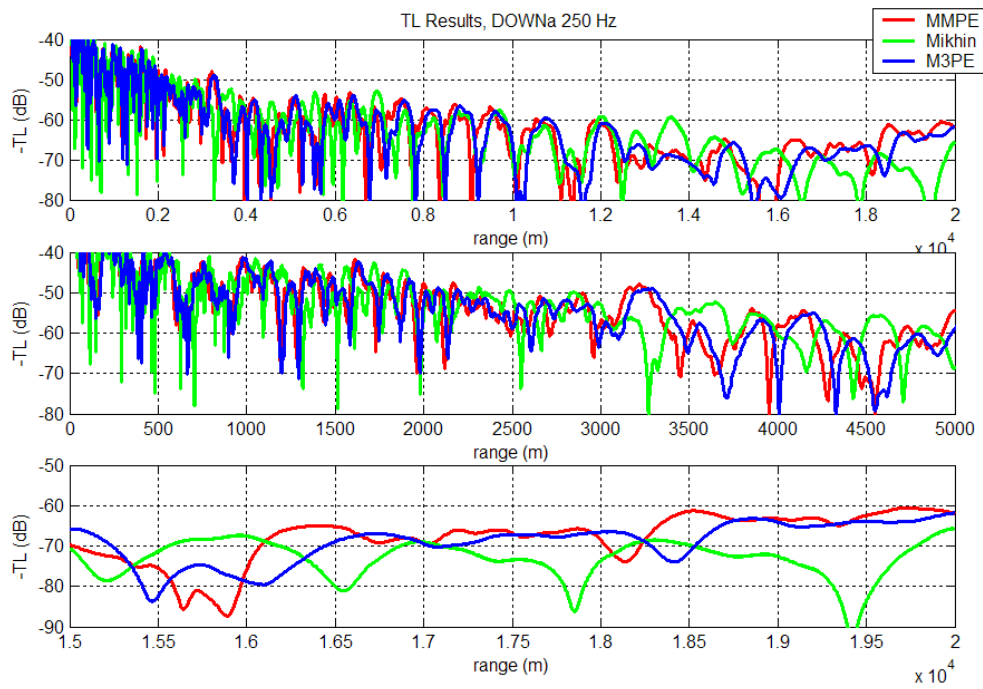


Figure 21. Comparison of transmission loss at 250 Hz between MMPE, Mikhin's IFD, and M3PE PE models for the DOWNa environment

E. TRANSMISSION LOSS FOR IWa

The final benchmark is characterized by a constant ocean depth and density (ρ_w) in the water column, but a highly variable water sound speed (c_w). Since the range- and depth-dependent sound speed profile is intended to represent the possible effects from internal waves, the environment is labeled IWa. A ray trace illustrating propagation in the water column is shown in Fig. 22 (again $z_s = 30$ m). All the other environmental parameters, such as bottom sound speed (c_b), gradient of bottom sound speed ($\partial c_b / \partial z$), and bottom density (ρ_b) are constant versus range. Again, the attenuation is zero in the water column (α_w) and 0.1 dB/ λ in the bottom (α_b). The shear sound speed (c_s) and attenuation (α_s) are also zero. A color coded representation of sound speed, density and attenuation versus range and depth for this environment is illustrated in Fig. 23. A summary of all parameters for the IWa environment is given in Table 2.

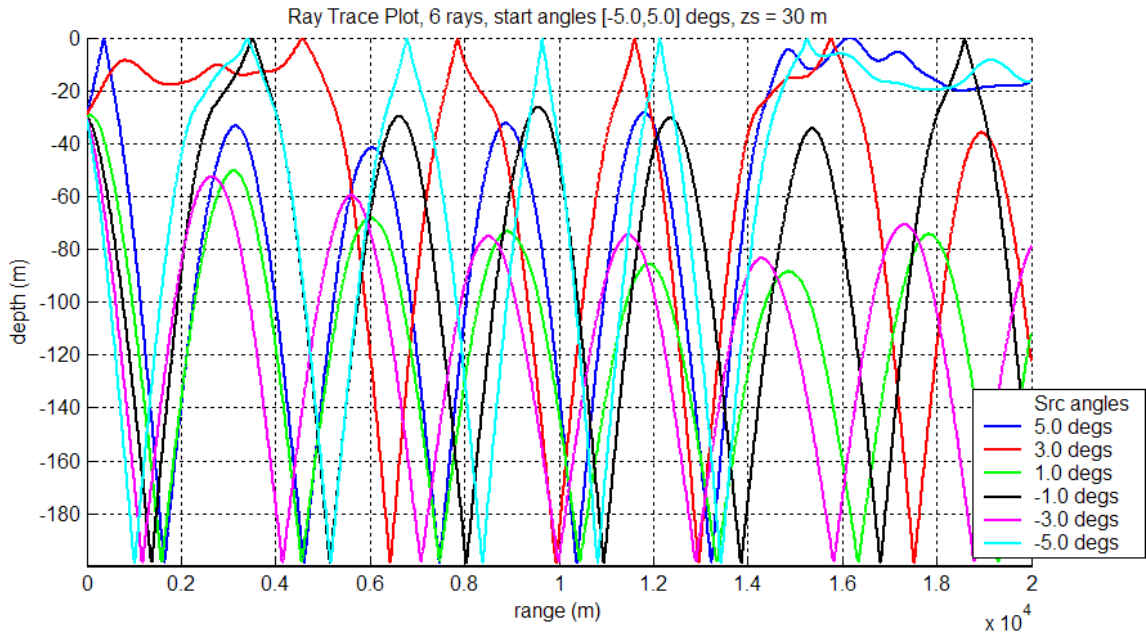


Figure 22. Ray trace in water column for the IWa environment, $z_s = 30$ m

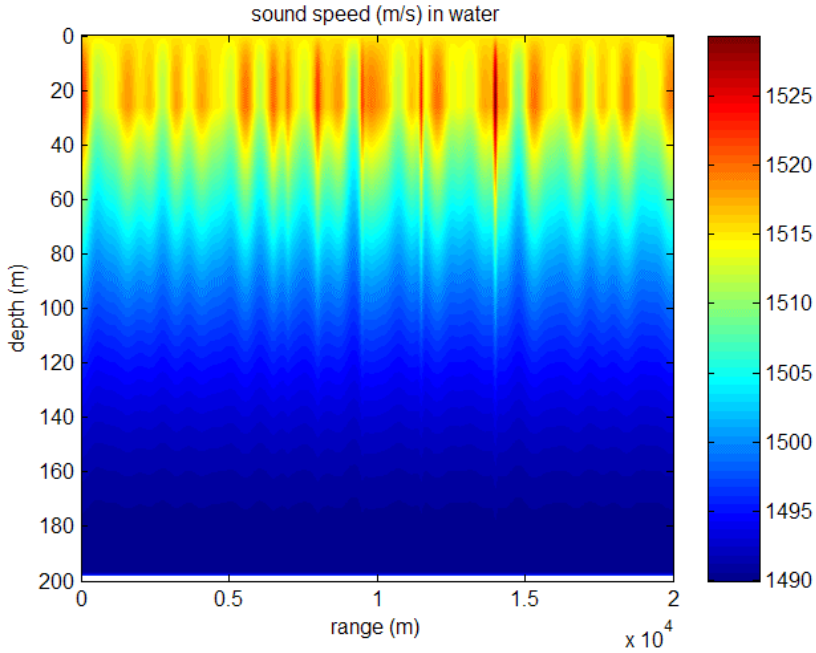


Figure 23. Sound speed vs range and depth for the IWa environment

Table 3. Environmental parameters for the IWa environment

Bottom depth (m)	c_w m/s	ρ_w (kg/m ³)	α_w dB/λ	c_b m/s	$\frac{\partial c_b}{\partial z}$ m/s/m	ρ_b (kg/m ³)	α_b dB/λ	c_s m/s	α_s dB/λ
200	variable	1000	0.0	1700	0	1500	0.1	0.0	0.0

The ray trace in Fig. 22 shows a very complicated propagation environment with multiple bottom bounce propagation without many surface interactions due to the high sound speeds near the surface. However, a weak surface duct is also supported for small range sections. An example TL versus range and depth plot is provided in Fig. 24.

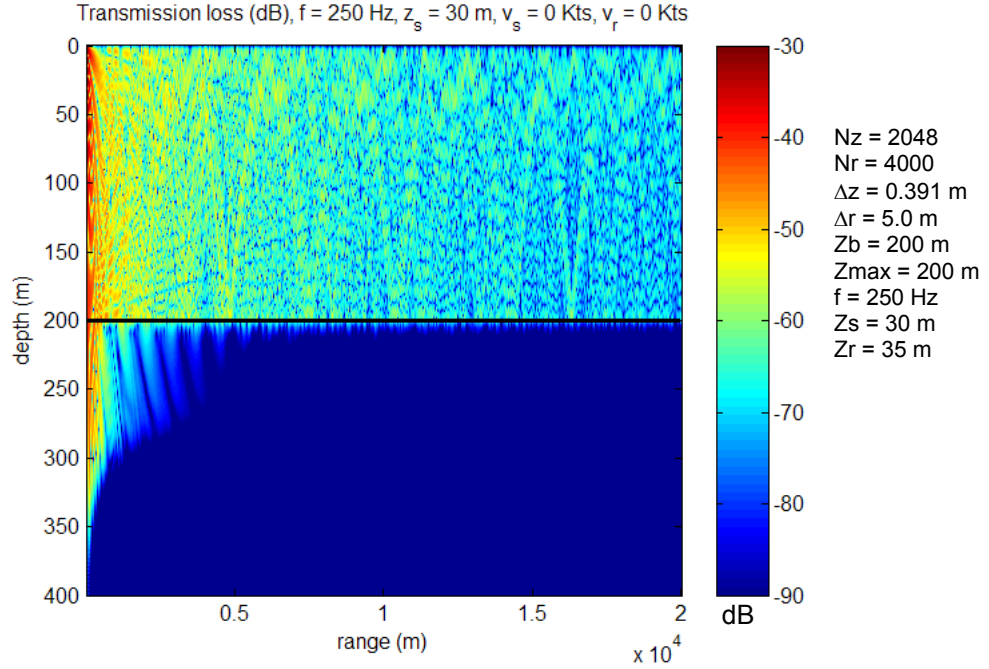


Figure 24. Transmission loss vs range and depth at 250 Hz for the IWA environment

A comparison between the TL generated by the M3PE, MMPE and the IFD model for the IWA environment is shown in Fig. 25. Again z_s is 30 m and z_r is 35 m. It can be observed that, in this case, all three models produce similar results out to about 4000 m. Also, the dissimilarities at the longer ranges are fairly modest. However, the complexity of the sound speed makes it difficult to draw any conclusions regarding the closeness of detailed fluctuations at the longer ranges. It suffices to say that the general trend of all three models across the 20 km propagation distance is fairly similar.

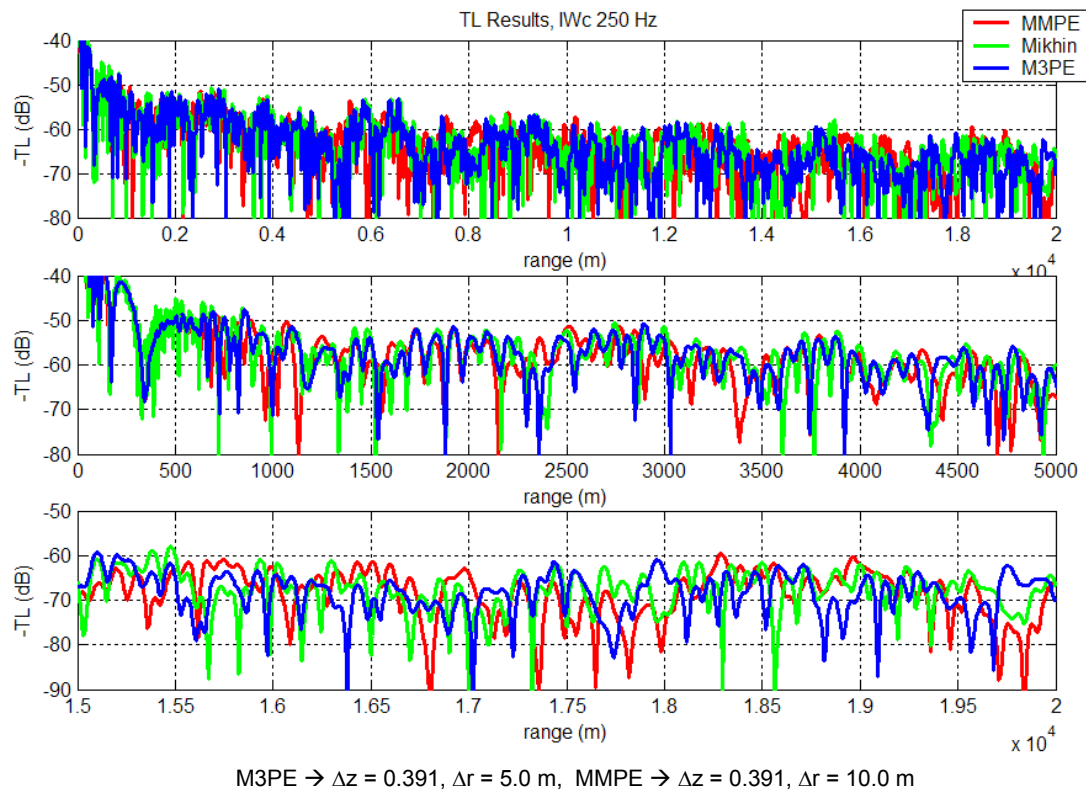


Figure 25. Comparison of transmission loss at 250 Hz between MMPE, Mikhin's IFD, and M3PE PE models for the IWa environment

V. BANDWIDTH ESTIMATION AND STATISTICAL CHARACTERIZATION

The linear magnitude of the transmission loss distributed across range, depth and frequency associated with a moving source and receiver serves as the domain from which the received signal bandwidth is estimated. The bandwidth parameter is designed to represent the spreading of the TL across frequency with a single parameter. There are several accepted methods for defining bandwidth. For example the effective bandwidth equation used to characterize the transfer function of digital filters is a common method.³⁹ The formulation for this estimator is given as

$$\delta_B = \frac{\Delta f \left(\sum_{i=1}^N p_i \right)^2}{\sum_{i=1}^N p_i^2} \quad . \quad (83)$$

Here p_i is the magnitude of the evaluated magnitude response across (in our case) frequency and the constant Δf is the discrete separation of each frequency bin. Other definitions of the bandwidth parameter are also used in the literature, such as treating the frequency dependent pressure magnitude as a probability density function (PDF), and representing the sample standard deviation as a bandwidth.⁴⁰ The bandwidth parameter for this method would be

$$\delta_B = \Delta f \left(\frac{\sum_{i=1}^N (i - \mu_i)^2 p_i}{\sum_{i=1}^N p_i} \right)^{1/2} \quad , \quad (84)$$

where μ refers to the sample mean, $\mu = \frac{1}{N} \sum_{i=1}^N p_i$.

Still other methods use an iterative search algorithm to find the frequency limits that satisfy some objective function such as the rate of change of a normalized

boxcar integration statistic, or the deflection between the pressure magnitude at its peak and the lower values along the skirts.

For our study, we choose the bandwidth parameter described by Eq. (83) since our experience has shown this equation to give intuitively appealing results regardless of the shape of the underlying function. For example, the statistic equates to unity when the spectrum function is perfectly flat. An example of results generated with this equation on three different magnitude responses are shown in Fig. 26 below. It can be observed that the algorithm computes an “effective” bandwidth representing the fractional magnitude enclosed by the magnitude response across the evaluated area. Thus, the same bandwidth value can result from curves with remarkably different shapes. However, the statistic can provide reasonable parameter estimates even when the shape is fairly complicated.

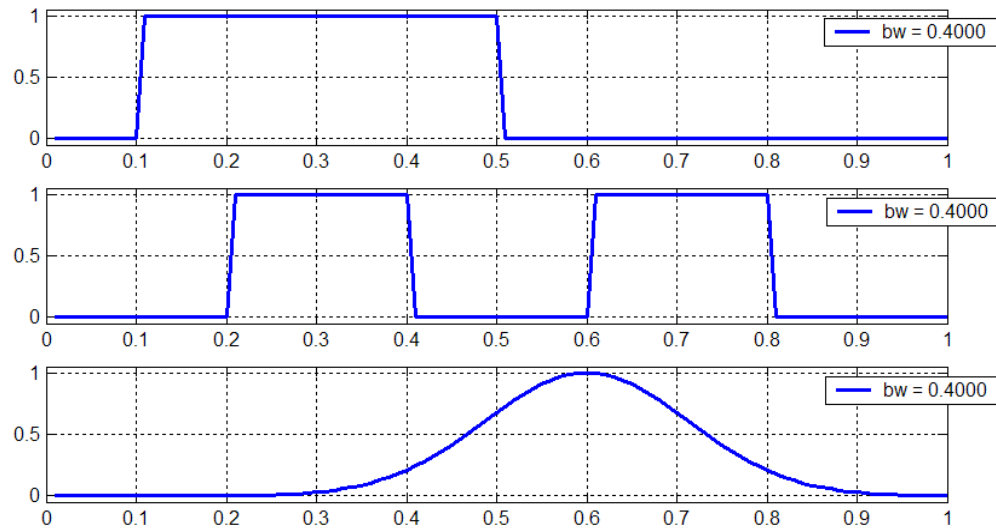


Figure 26. Example Bandwidths Computed for Three Different Functions

In the next section, we compute the BW parameter from the frequency variant transmission loss represented on a discrete grid of range and depth cells associated with several different ocean environments. The results are plotted as an aggregate histogram including estimates of the sample mean and standard

deviation. Additionally, the bandwidth variables are marginalized over one independent variable (e.g., range or depth) and plotted against the other. Finally, scatter plots of bandwidth versus the normalized linear magnitude of the minimum transmission loss across frequency are generated. The histogram describes the overall behavior of the random variable across the entire range-depth space. The marginalized plots show the behavior versus range or depth, averaged across the other independent variable. Finally, the two-dimensional scatter plots portray the parameter as a function of normalized TL. Any general dependencies upon local TL level are highlighted in this plot.

The bandwidth statistic is a measure of the properties of the received signal. It is assumed that the signal being measured has sufficient signal to noise ratio (SNR) to support detection and accurate parameter estimation. Thus in all cases where we use the response of the transmission loss to estimate bandwidth, we are assuming that sufficient SNR remains after the TL is accumulated with the source level (SL), noise level (NL) and other components of the sonar equation. When the TL is so high to preclude detection of even the loudest known sources at nominal ranges, the predicted bandwidth parameters have little practical value. We shall see a case in the next section where this situation becomes important.

THIS PAGE INTENTIONALLY LEFT BLANK

VI. NUMERICAL EXPERIMENTS WITH A MOVING SOURCE AND RECEIVER

In this section, we demonstrate the model on a set of notional ocean environments. Our intention is to explore the way in which transmission loss varies across frequency as a function of range and depth when both the source and receiver are in motion. The bandwidth parameter is used to quantify the shape of the TL vs frequency, including the dependencies of this shape on range, depth, and TL magnitude. A description of the acoustic parameters associated with the ocean environments is given in Section A. The results obtained from the TL model are given in Section B.

A. DESCRIPTION OF ENVIRONMENTS

Four different environments were evaluated. We describe these according to the following general characteristics. The first two environments have range-independent ocean bottom depths, while the third and fourth environments have range-dependent bottom depths. All environments have range-independent sound speed profiles with a bilinear shape. Also, the first three environments are specified as a single, angle-independent radial, of maximum range equal to 15000 m. The fourth environment is specified out to 40000 m.

The first environment has a constant 600 m water depth, and an SSP with a positive (downward refracting) upper layer and a negative (upward refracting) lower layer. The second environment has a constant 120 m water depth, and an SSP with both layers having a negative (upward refracting) slope. The third environment has a range-dependent bottom depth of 600 m at the source position, and ends with a 200 m bottom depth at 15000 m. The final environment is intended to represent a deeper water ocean having a 3000 m depth at the source position, and ending with a 500 m depth at 40000 m. These environments are intended to represent a variety of conditions such as a very shallow water littoral, medium depth coastal shelf, and deep water transition region.

The density of the water in all environments was set at 1024 kg/m^3 . The water absorption was specified by the Fisher-Simmons model where the salinity = 35 ppm, temperature = 15.6°C , and pH = 8. In all cases, the bottom was specified as a single fluid layer with no shear properties. The bottom parameters were specified as $c_b = 1600 \text{ m/s}$, $\frac{\partial c_b}{\partial z} = 0.2 \text{ s}^{-1}$, $\rho_b = 1700 \text{ kg/m}^3$, $\alpha_b = 0.1 \text{ dB/}\lambda$.

The bottom roughness was produced with the Fox-Hayes approach, where $\sigma = 1 \text{ m}$, $L_{\text{cor}} = 100 \text{ m}$, and $\beta = 3.5$ (see Eq. (77)). In all cases, the frequency of transmission was 100 Hz. Also, the source velocity $v_s = 15 \text{ kts}$, and the receiver velocity $v_r = -5 \text{ kts}$ (indicating a receiver traveling in the opposite direction of the source). In each numerical experiment, the source depth was run at both $z_s = 50 \text{ m}$ and $z_s = 3 \text{ m}$ in order to compare the impact of source depth.

A ray trace of each environment was computed using the method described in Appendix B. The implementation supports a range-dependent SSP and bottom depth, and assumes perfect surface and bottom reflection. Appendix B includes a derivation of the method along with a User's Guide supporting its operation.

The horizontal and vertical mesh sizes, along with the frequency resolution associated with each environment, are listed in Table 4.

Table 4. Mesh sizes used for each environment

Environment	1	2	3	4
N_r	512	512	512	512
Δr	29.3 m	29.3 m	29.3 m	78.13 m
N_z	1024	512	1024	2048
Δz	1.17 m	0.47 m	1.17 m	2.93 m
N_f	60	60	60	60
Δf	0.0132 Hz	0.0132 Hz	0.0132 Hz	0.0132 Hz

It is recognized that the above parameters provide a somewhat courser range and (in some cases) depth resolution than the recommendations given in

Section III.E. In the first three environments, at 100 Hz, this represents about a factor of two more than the recommended mesh sizes in Eqs. (81) and (82). However, our analysis in Section IV showed that the degradation is relatively minor out to moderate ranges when the mesh size is one half of what might be considered optimal. In our fourth environment, the mesh sizes are quite coarser than recommended. However, it is felt that the resolution is sufficiently adequate to characterize the shape of the TL response in frequency versus range and depth, and that the absolute magnitude values are of secondary interest. Limitations on memory and computational throughput dominated our rationale for the mesh size selected in this case.

The acoustic propagation for each environment and the two source depths is described by a ray trace plot, source k - f (wavenumber-frequency) contour plot, and a TL versus range and depth plot representing the minimum TL across frequency. Also, the TL versus frequency response for various ranges and a fixed depth was plotted for each experiment.

The bandwidth (BW) parameter described by Eq. (84) was computed for each environment and source depth case, and at each range and depth cell. The aggregate behavior is described by a histogram of BW variables from all cells in the water column. The density of BW is plotted along a horizontal axis that spans a zero to a six- σ range. Also, the BW versus the normalized magnitude of relative pressure at each cell is plotted on a 2-D scatter plot. The normalization refers to multiplying the PE pressure field by \sqrt{r} to remove the effects of cylindrical spreading on the statistics. Thus, the scatter plots represent the dependency of BW on the local interference structure, vice the absolute transmission loss. Finally, the average BW across depth for each range cell, and across range for each depth cell is plotted. These plots show the variability of a marginalized BW with range and depth.

B. DESCRIPTION OF RESULTS

This section describes the results associated with each environment.

1. Environment #1

The depth dependent acoustical parameters (SSP, density and attenuation) for the first environment are illustrated in Fig. 27. A set of ray traces projected within $\pm 10^\circ$ vertical angle limits, at a source depth of 50 m, is illustrated in Fig. 28. At the source depth of 50 m, the rays show a combination of refracted direct paths and bottom bounce propagation.

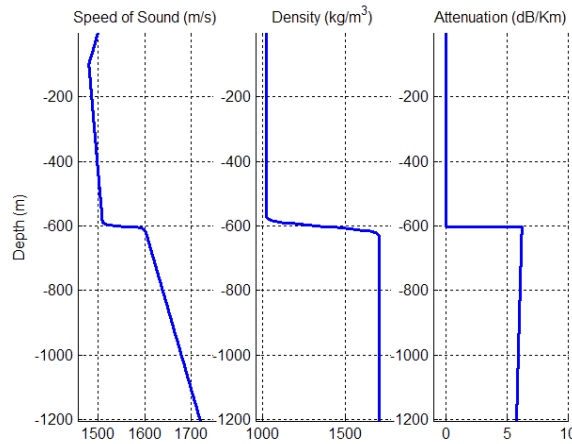


Figure 27. Acoustic parameters for environment #1

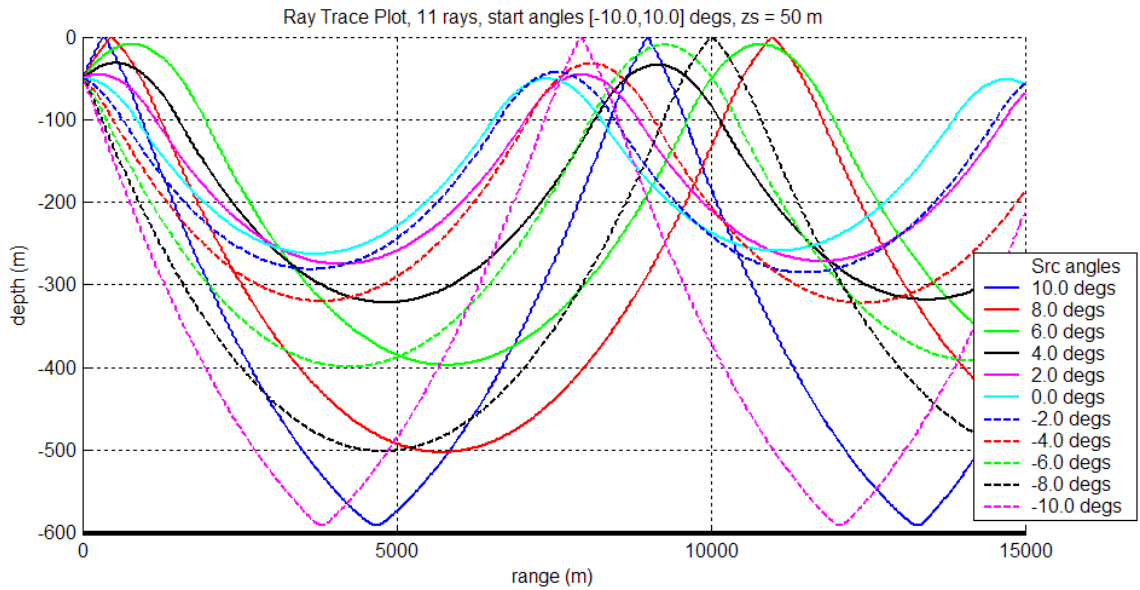


Figure 28. Ray trace for environment #1, $z_s = 50$ m

Figure 29 is a contour plot of the distribution of source magnitude across wavenumber and frequency. The figure represents the distribution of the energy caused by a 15 knot source speed at 100 Hz, and a 0° vertical direction. The original CW source is transmitted into the medium with a min-max bandwidth of about 0.52 Hz due to source motion-induced Doppler spreading. The magnitudes of the source function vary with wavenumber due to the Thomson-Bohun²² taper function described previously in Eq. 32.

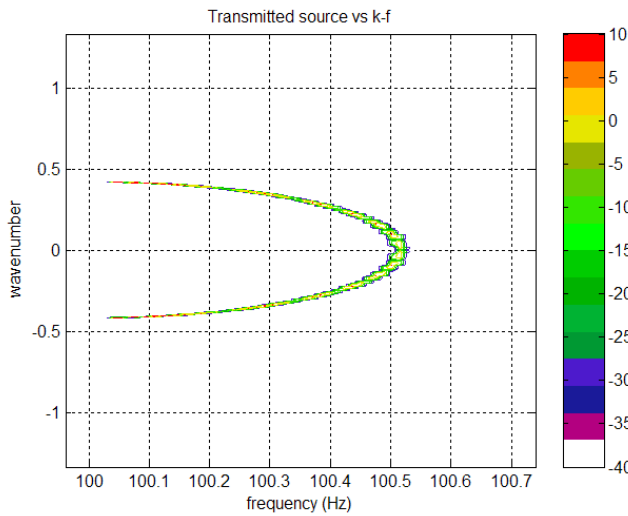


Figure 29. k-f spectrum of source in environment # 1, $z_s = 50$ m, $v_s = 15$ kts

Figure 30 illustrates the range and depth-dependent transmission loss computed by the M3PE implementation for environment #1 out to 15,000 m with the source at 50 m. The plot represents the minimum loss at each range-depth cell for all frequencies evaluated. It can be observed that dominant energy is propagated at fairly shallow angles. High angle propagation is also apparent in the interference pattern, but with higher transmission loss. Figure 31 plots a 2-D slice of the TL vs range at the depth of 50 m.

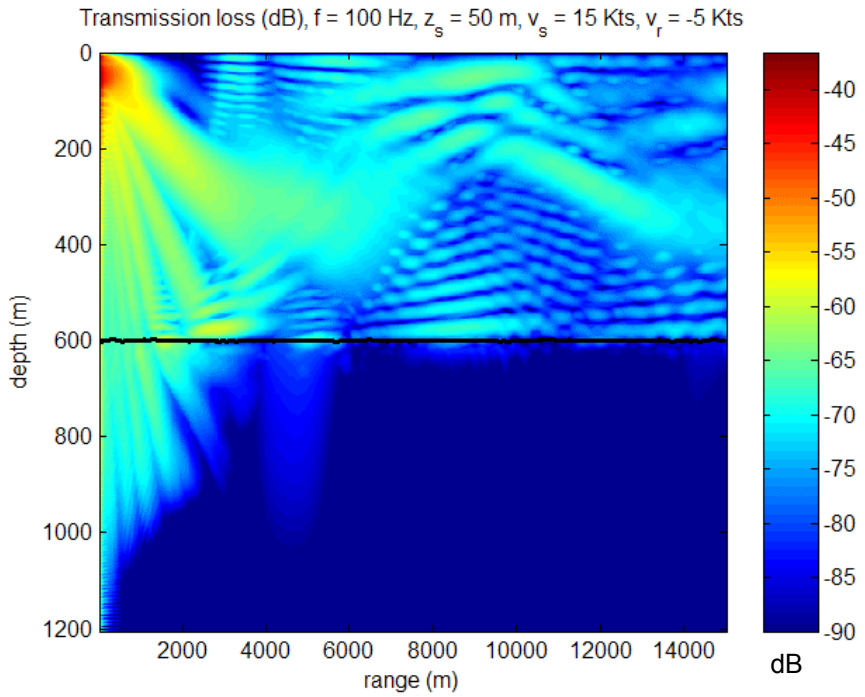


Figure 30. Minimum transmission loss across frequency vs range and depth for environment # 1, $z_s = 50$ m, $v_s = 15$ kts, $v_r = -5$ kts

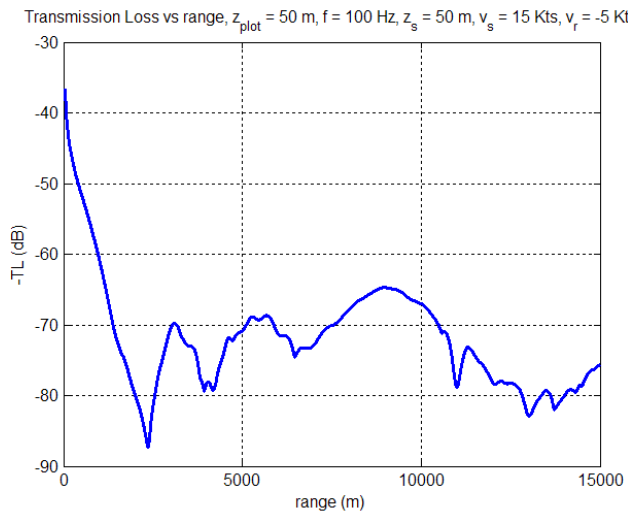


Figure 31. Minimum transmission loss across frequency vs range for environment # 1, $z_s = 50$ m, $z_r = 50$ m

Figure 32 is an example plot of the transmission loss at all frequencies, evaluated at the discrete ranges between 5000 m and 5300 m, at a depth of 50 m. From the range resolutions provided in Table 4, this translates into about 10 separate response curves overlaid on the same plot. Interestingly, it can be observed that most of the energy exists above the maximum transmitted frequency indicated by Fig. 29. This is because the receiver motion (-5 knots), in the opposite direction of the source motion, imparts an extra Doppler shift to the TL distribution towards the right. Thus, the dominant energy now exists about a frequency of 100.65 Hz. It can also be observed that the main lobe has a width of about 0.08 Hz at the 10 dB down points. Also, there is significant “structure” at other frequencies (namely a set of local maxima around 100.55 Hz) although at a much lower level (~40 dB below the peak).

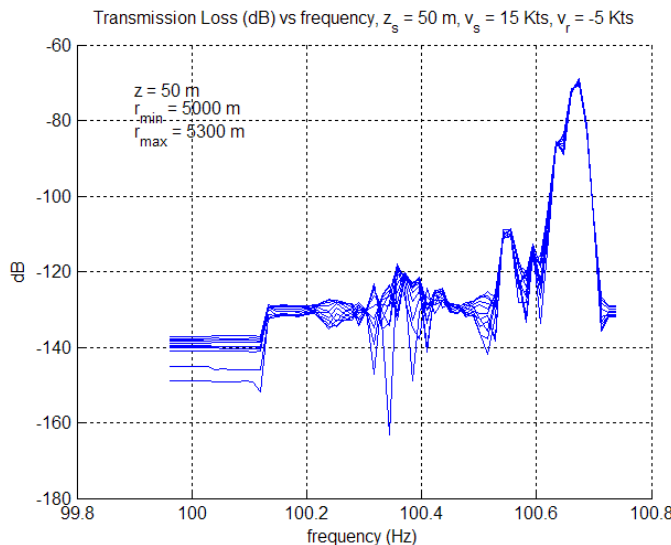


Figure 32. Transmission loss vs frequency, environment #1, $z_s = 50$ m, $z_r = 50$ m, $5000 \text{ m} < r < 5300 \text{ m}$, $v_s = 15 \text{ kts}$, $v_r = -5 \text{ kts}$

Figure 33 illustrates TL distribution across frequency for all ranges between 0-15000 m, at the constant received depth of 50 m. In this 3-D plot, it can be seen that the TL response is fairly broadband at short ranges, but rapidly tapers to a steady state narrow shape after about 1-2 km. This near-field broad bandwidth is probably caused by the predominance of high angle

propagation that still has significant energy close to the source. This effect is likely also amplified by the Thomson and Bohun high wavenumber correction factor incorporated into the source function. This energy rapidly attenuates after high angle boundary interactions, causing the shape of the TL response to concentrate around a single local maximum after a few thousand meters.

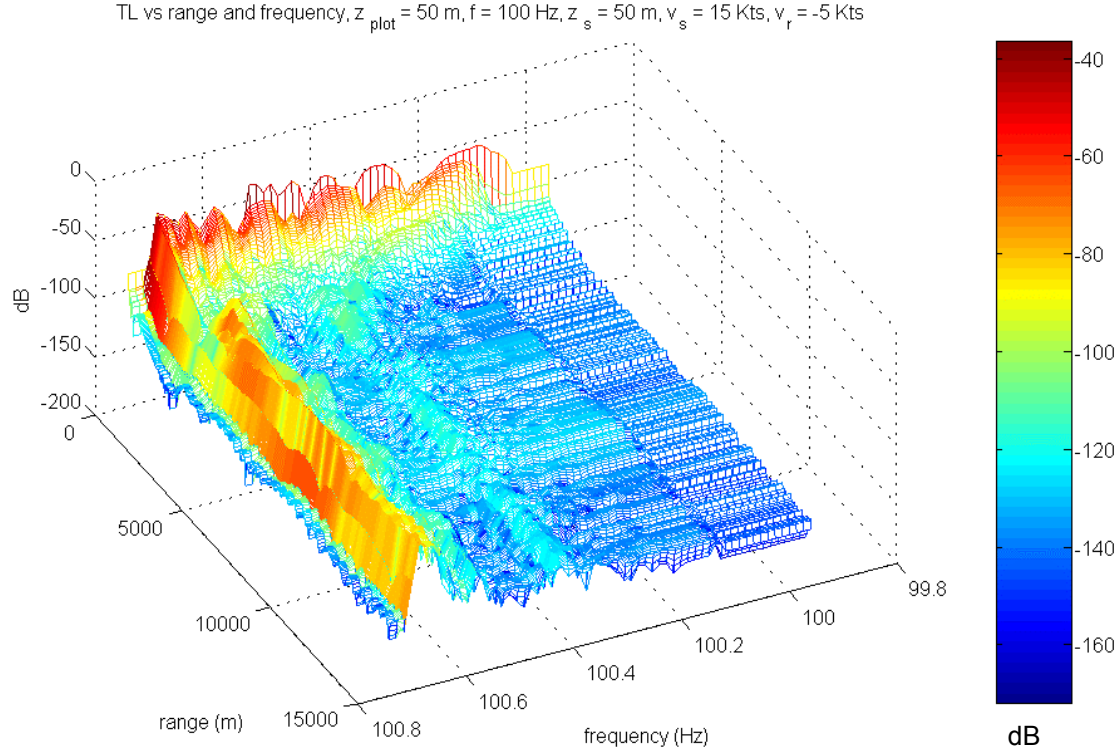


Figure 33. Transmission loss vs frequency and range, environment #1, $z_s = 50 \text{ m}$, $z_r = 50 \text{ m}$, $v_s = 15 \text{ kts}$, $v_r = -5 \text{ kts}$

The aggregate behavior of the bandwidth (BW) estimates at each range and depth cell, for environment 1 with the source at 50 m, is depicted in Figs. 34 and 35. Recall that the bandwidth parameters are computed on the linear PE pressure magnitudes with the frequency-independent cylindrical spreading term removed. Figure 34a shows the average BW at each range across all depths in the water column. Figure 34b shows the average BW at each water depth across all range cells. It can be seen that the BW depends somewhat on range, but not

as much on depth in this environment. Figure 34a is simply a parametric representation of the frequency response characteristics observed in the 3-D TL distribution shown in Fig. 33.

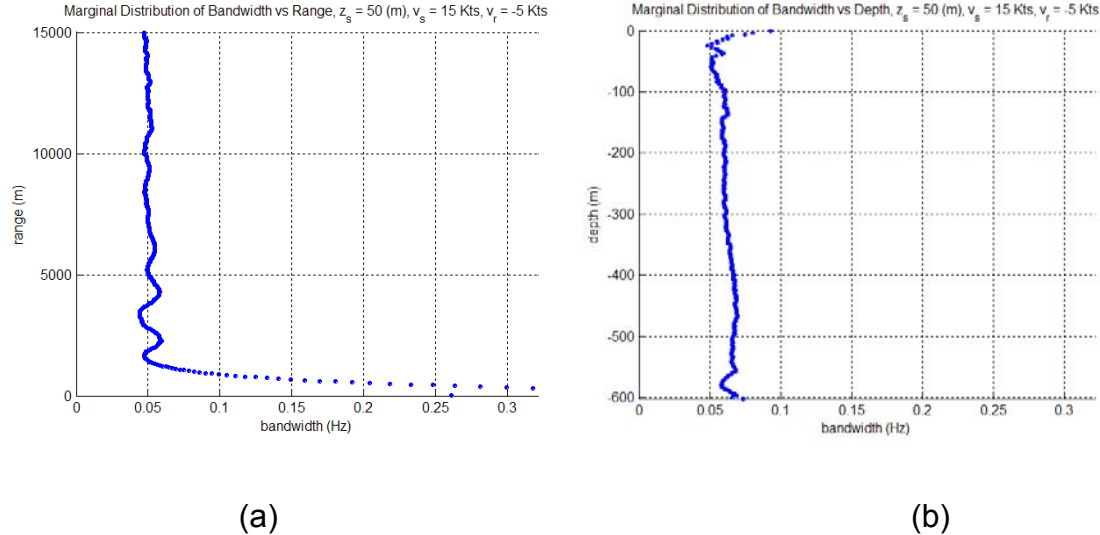


Figure 34. Marginalized bandwidth vs range (a), and depth (b) , environment #1, $z_s = 50$ m, $v_s = 15$ kts, $v_r = -5$ kts

Figure 35a shows an overall histogram of bandwidths for all ranges and depths (above the bottom). From this plot, a sample mean BW of about 0.06 Hz, and a standard deviation of about 0.05 Hz has been computed. Finally, the dependency of BW on the local peak pressure magnitudes across frequency is provided in Fig. 35b. At first glance, this plot might seem to contradict the behavior shown in Figs. 33 and 34a, where shorter ranges (and lower TL) provide for larger bandwidths. That is, the overall trend in Fig. 35b is for cells with high pressure magnitudes to have smaller bandwidths than cells with lower magnitudes. However, a second look at this figure indicates that there is a segment of samples with high bandwidth at the larger pressure magnitudes. These bandwidths are likely from the closer ranges. Thus it is concluded that two contradictory influences are in play. We can summarize this by stating that the bandwidth values are generally proportional to absolute TL level, except at short ranges where high bandwidths are caused by high angle propagation, even when

the overall TL is low.

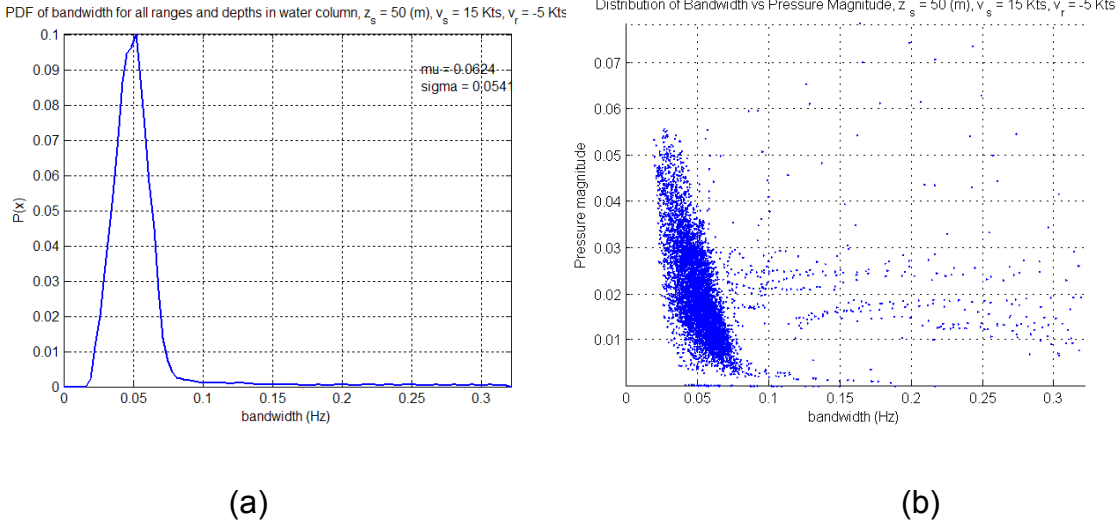


Figure 35. Aggregate histogram (a) and scatter plot vs normalized linear TL (b), environment #1, $z_s = 50$ m, $v_s = 15$ kts, $v_r = -5$ kts

The next set of Figs. 36-42 repeat the results presented in Figs. 28-35 for the same environment (#1), but with the source positioned at 3 m instead of 50 m. Here, the ray trace (Fig. 36) and minimum TL plots (Figs. 37 and 38) show a TL response that is much more dominated by high angle propagation and boundary interactions. The shape of the frequency response shown in Figs. 39 and 40 is similar, but the dominant frequency component is a bit wider. Also, a secondary propagation mode at about 100.37 Hz is more dominant for the shallow source. Figures 41 and 42 show a very similar behavior as for the deeper source, except that all plots are shifted towards higher bandwidths by about 0.02 Hz. Thus, the shallower source demonstrates a marginally higher aggregate bandwidth than the deeper source in this environment. An interesting difference between the two sets of results is that the average minimum TL at the outer ranges is about 5-10 dB greater for the shallow source than the deeper one. As expected, the higher angle propagation also results in more TL.

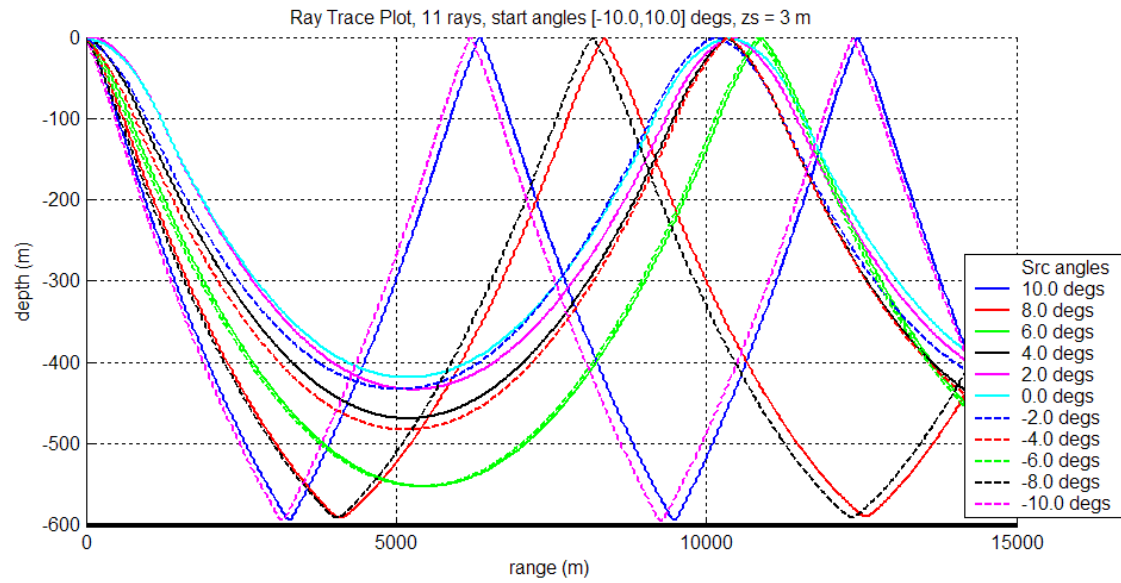


Figure 36. Ray trace for environment #1, $z_s = 3$ m

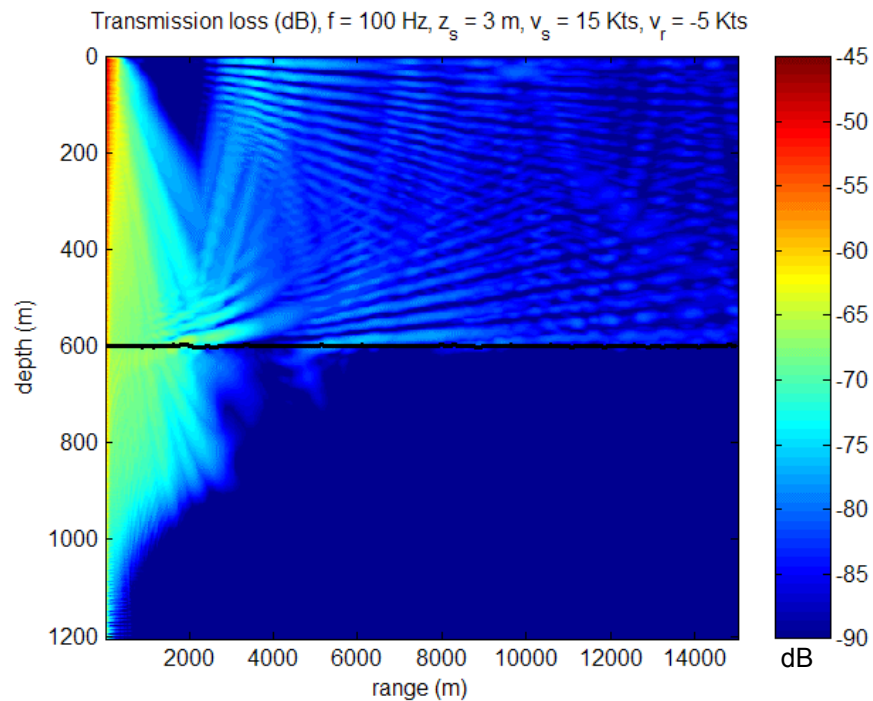


Figure 37. Minimum transmission loss across frequency vs range and depth for environment # 1, $z_s = 3$ m, $v_s = 15$ kts, $v_r = -5$ kts

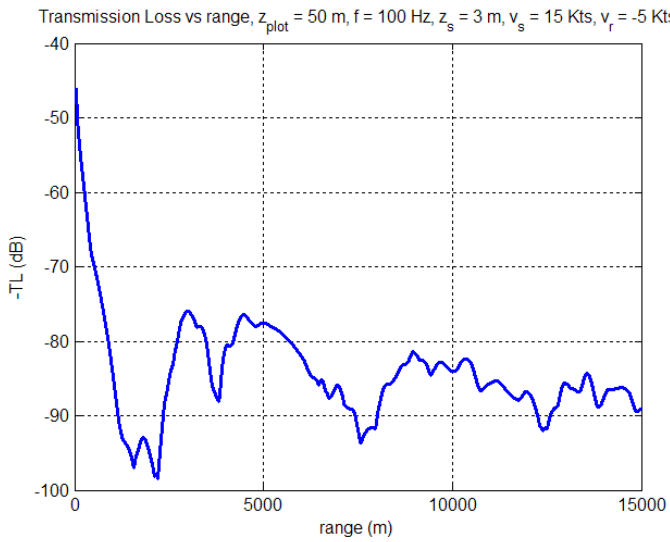


Figure 38. Minimum transmission loss across frequency vs range for environment # 1, $z_s = 3 \text{ m}$, $z_r = 50 \text{ m}$, $v_s = 15 \text{ kts}$, $v_r = -5 \text{ kts}$

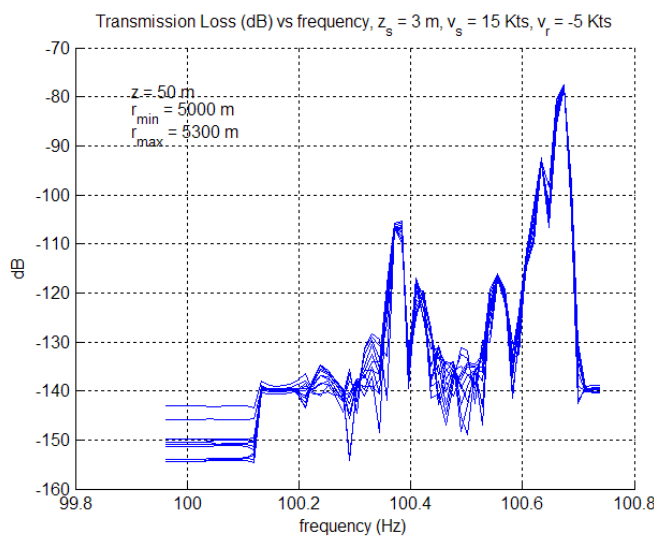


Figure 39. Transmission loss vs frequency, environment #1, $z_s = 3 \text{ m}$, $z_r = 50 \text{ m}$, $5000 \text{ m} < r < 5300 \text{ m}$, $v_s = 15 \text{ kts}$, $v_r = -5 \text{ kts}$

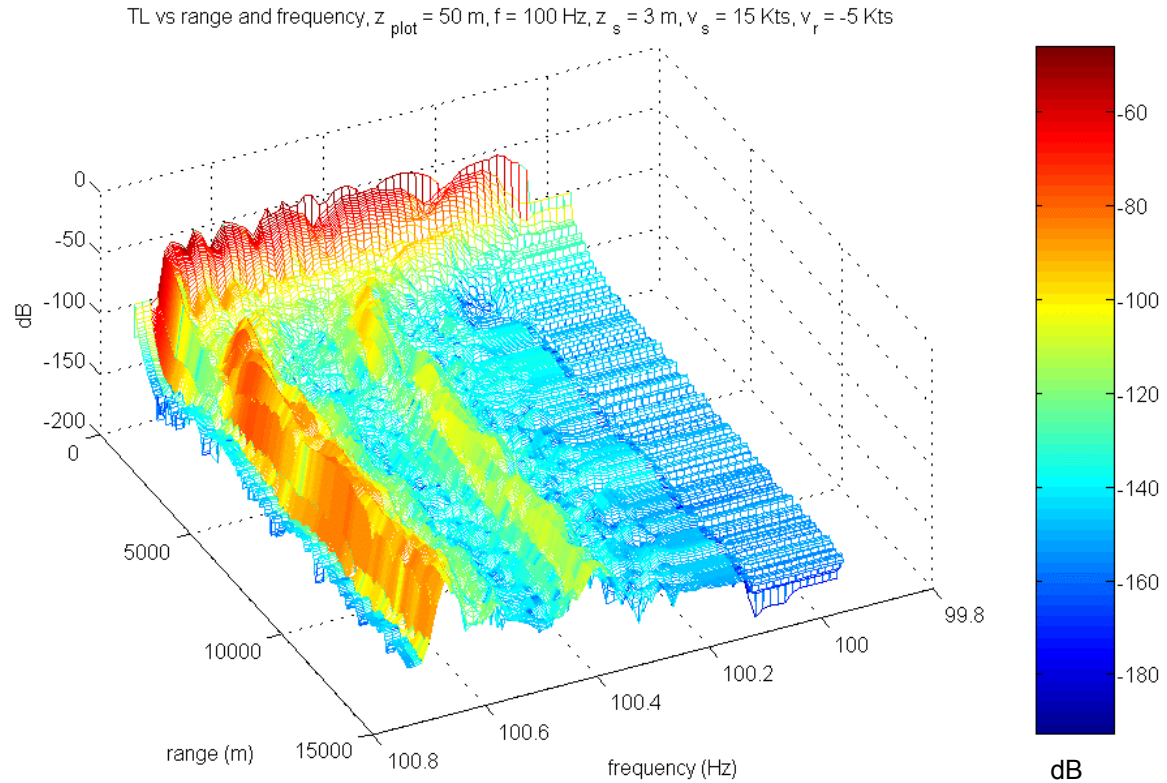


Figure 40. Transmission loss vs frequency and range, environment #1, $z_s = 3 \text{ m}$, $z_r = 50 \text{ m}$, $v_s = 15 \text{ kts}$, $v_r = -5 \text{ kts}$

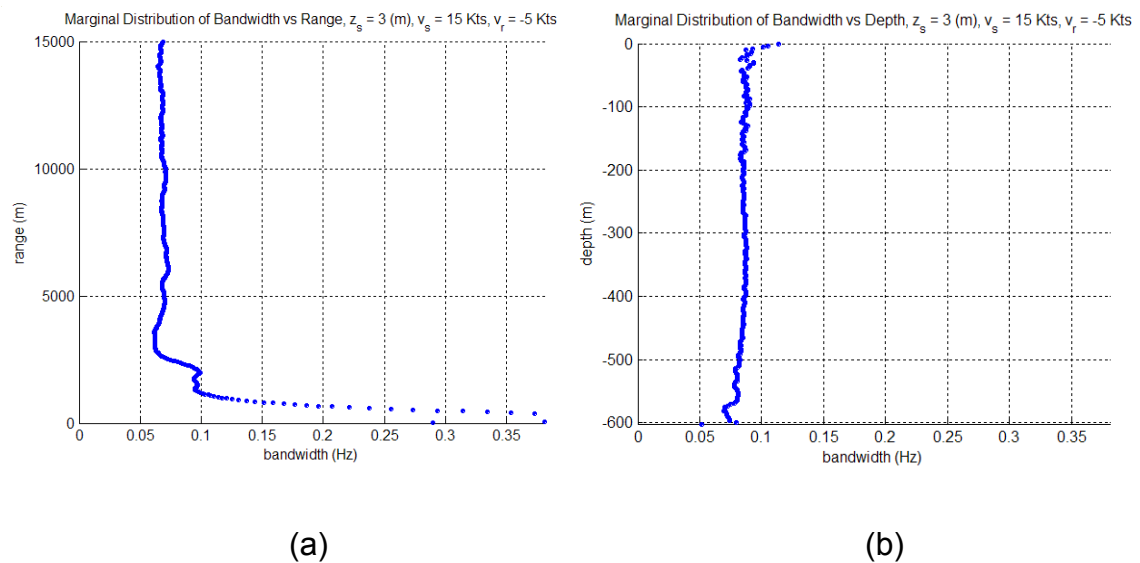


Figure 41. Marginalized bandwidth vs range (a), and depth (b) , environment #1, $z_s = 3 \text{ m}$, $v_s = 15 \text{ kts}$, $v_r = -5 \text{ kts}$

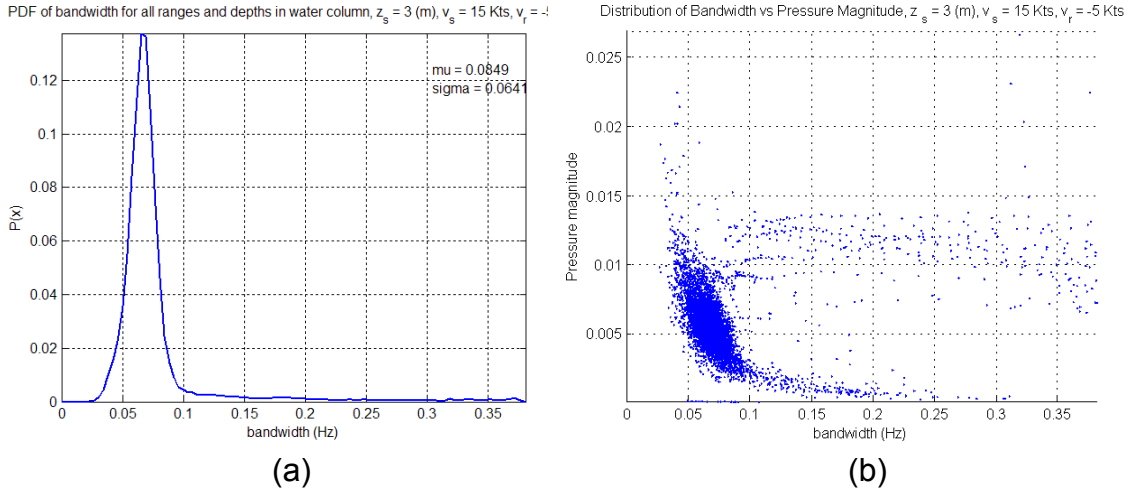


Figure 42. Aggregate histogram (a) and scatter plot vs normalized linear TL (b), environment #1, $z_s = 3$ m, $v_s = 15$ kts, $v_r = -5$ kts

2. Environment #2

The depth-dependent parameters associated with environment #2 are illustrated in Fig. 43. The ray trace in Fig. 44 indicates that this environment is a very shallow water waveguide with upward refracting propagation. The source spectrum versus wavenumber is shown in Fig. 45. The transmission loss results versus range and depth for a source at 50 m are shown in Figs. 46-47. It can be observed that relatively low TL values occur in the surface duct even at long ranges when the source is deep. This is confirmed by the ray trace which shows that propagation at narrow angles from a source at 50 m can occur with large skip distances between surface interactions. The TL versus frequency and range is shown in Figs. 48 and 49. As a side note, Fig. 46 also allows one to observe an example of the rough bottom generated for all environments. In this plot (vice the other environments), the ocean is sufficiently shallow such that the scale allows sufficient bottom structure to be observable.

The bandwidth parameters are illustrated in Figs. 50 and 51. The mean bandwidth is about 0.06 Hz and the standard deviation was 0.03 Hz. Figures 49 and 50a illustrate that the transition between wide bandwidths at short range, and the steady state narrow bandwidths, which occur much more quickly in

environment #2 than environment #1. However, the dependence of bandwidth on receiver depth is more significant in this environment than the previous one. Specifically, the bandwidths are wider when the receiver is near the boundaries, vice towards the middle of the water column. This is corroborated by the fact that there is generally more TL near the boundaries than in the middle of the waveguide in this environment. Figure 51b also indicates that the bandwidths are generally wider when the pressure magnitude is lower (i.e., higher TL).

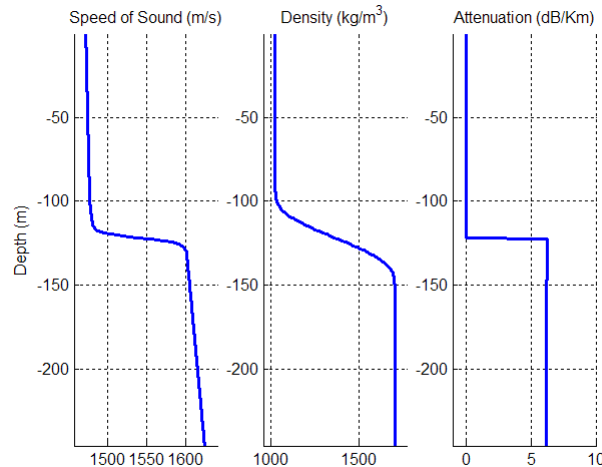


Figure 43. Acoustic parameters for environment #2

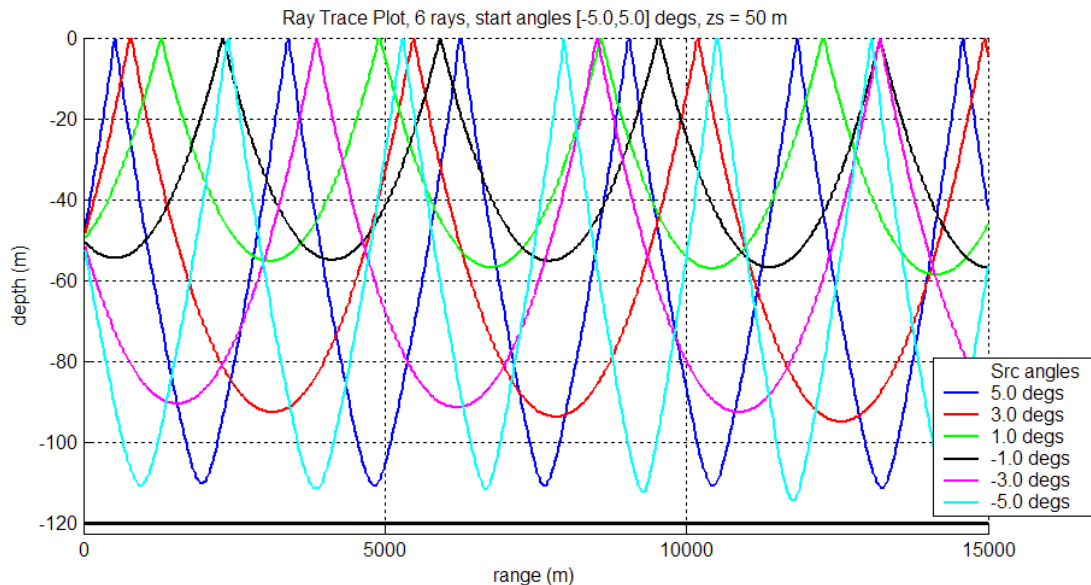


Figure 44. Ray trace for environment #2, $z_s = 50$ m

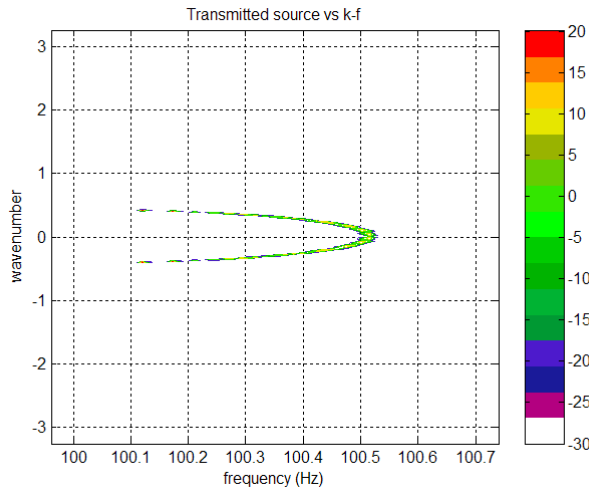


Figure 45. k-f spectrum of source in environment # 2, $z_s = 50$ m, $v_s = 15$ kts

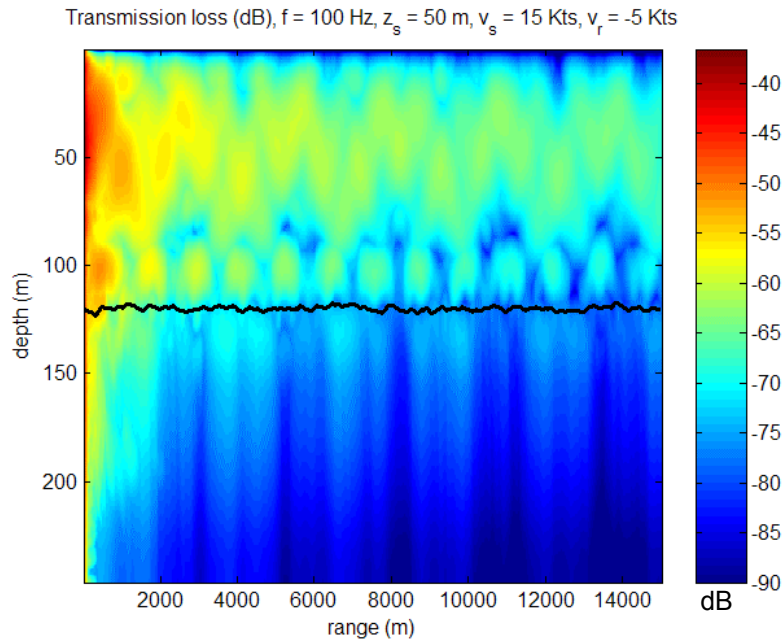


Figure 46. Minimum transmission loss across frequency vs range and depth for environment # 2, $z_s = 50$ m, $v_s = 15$ kts, $v_r = -5$ kts

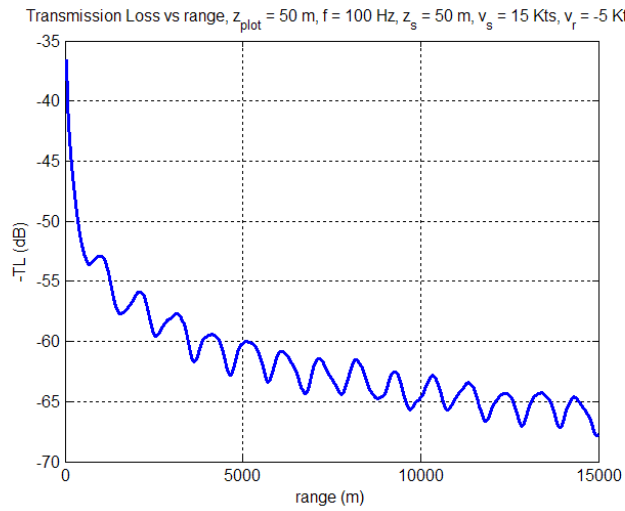


Figure 47. Minimum transmission loss across frequency vs range for environment # 2, $z_s = 50 \text{ m}$, $z_r = 50 \text{ m}$, $v_s = 15 \text{ kts}$, $v_r = -5 \text{ kts}$

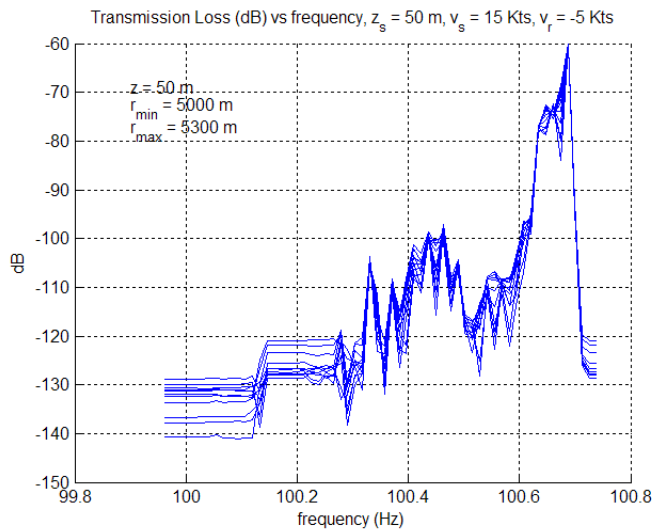


Figure 48. Transmission loss vs frequency, environment #2, $z_s = 50 \text{ m}$, $z_r = 50 \text{ m}$, $5000 \text{ m} < r < 5300 \text{ m}$, $v_s = 15 \text{ kts}$, $v_r = -5 \text{ kts}$

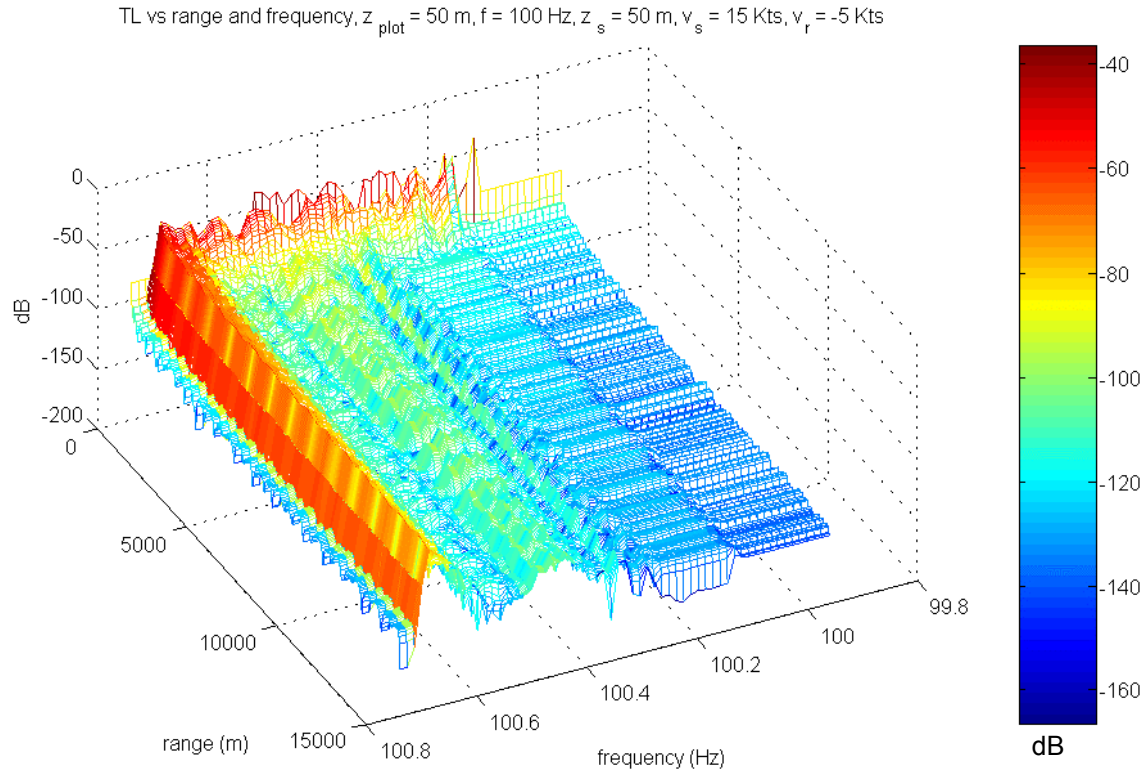


Figure 49. Transmission loss vs frequency and range, environment #2, $z_s = 50 \text{ m}$, $z_r = 50 \text{ m}$, $v_s = 15 \text{ kts}$, $v_r = -5 \text{ kts}$

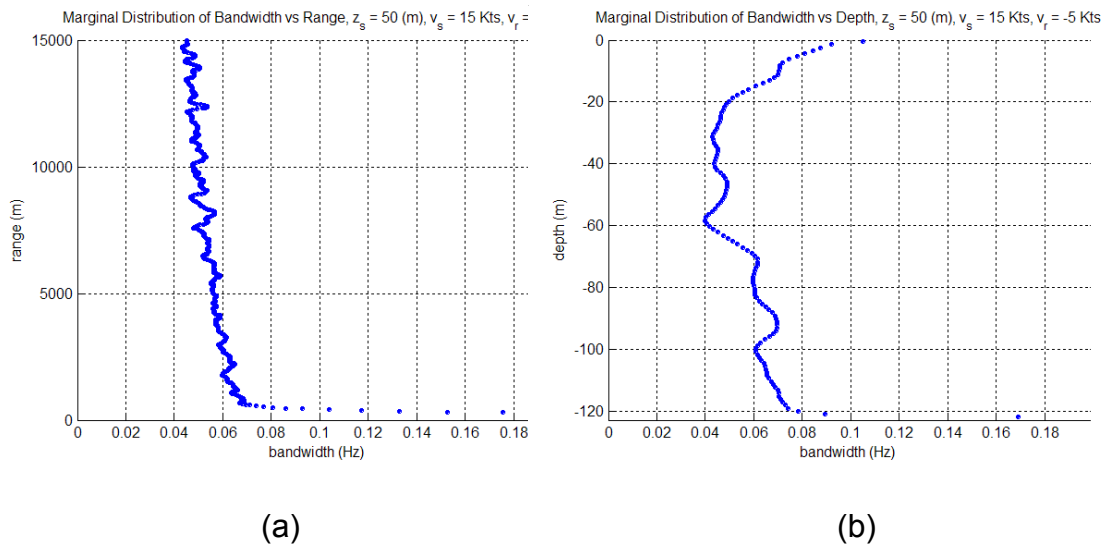


Figure 50. Marginalized bandwidth vs range (a), and depth (b), environment #2, $z_s = 50 \text{ m}$, $v_s = 15 \text{ kts}$, $v_r = -5 \text{ kts}$

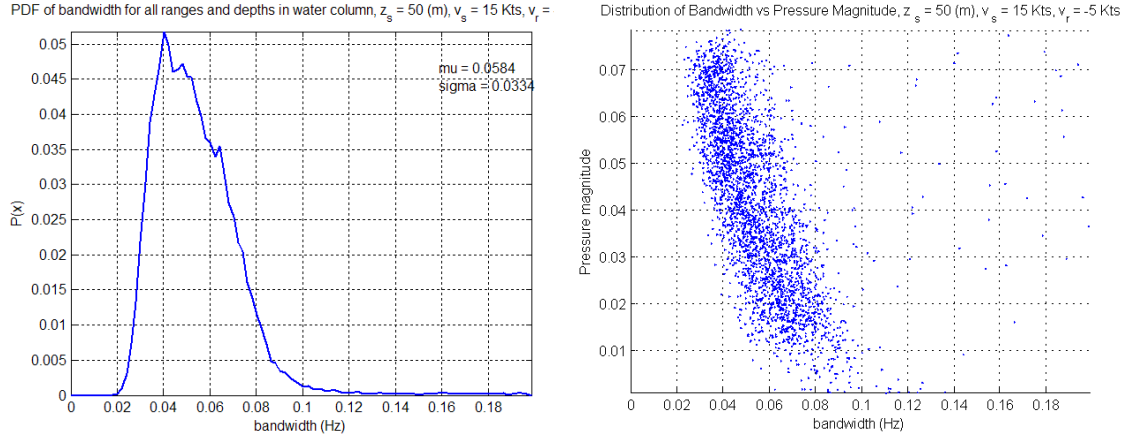


Figure 51. Aggregate histogram (a) and scatter plot vs normalized linear TL (b), environment #2, $z_s = 50$ m, $v_s = 15$ kts, $v_r = -5$ kts

Figures 52-58 repeat the numerical experiments associated with environment #2 for a source at 3 m. Again we observe (in Figs. 53 and 54) that a source at the shallow depth has generally more TL (at comparable ranges) than a deeper source. Also, Figs. 55 and 56 indicate that more relative energy is distributed across frequency when the source depth is shallow. Interestingly, the secondary contributions at the lower frequencies, for the 3 m source depth, are only about 12 dB down from the main peak, while they are almost 40 dB down for the 50 m source depth case. The average BW estimates plotted in Fig. 57(a,b) with a source at 3 m are generally about 0.05 Hz greater than the BW values from a source at 50 m, for environment #2. This could again be due to a greater tendency toward high angle propagation, as indicated by the TL versus range and depth plot in Fig. 53. The results for environments #1 and #2 demonstrate how two very different sets of acoustic conditions (i.e., one with downward refraction and the other with upward refraction) can still have similar effects on the characteristics of received signal bandwidth.

Also, the relationship between bandwidth and normalized pressure, plotted in Fig. 58b, is less dispersed for the shallow source than the deeper one. This is likely due to the fact that the range normalized transmission loss is less

variable (i.e., more uniform across depth) when the source is shallow than for the deeper source in this particular environment. This is also supported by Fig. 57b which indicates very consistent bandwidth parameters across depth, in contrast to the plot in Fig. 50b for the deep source.

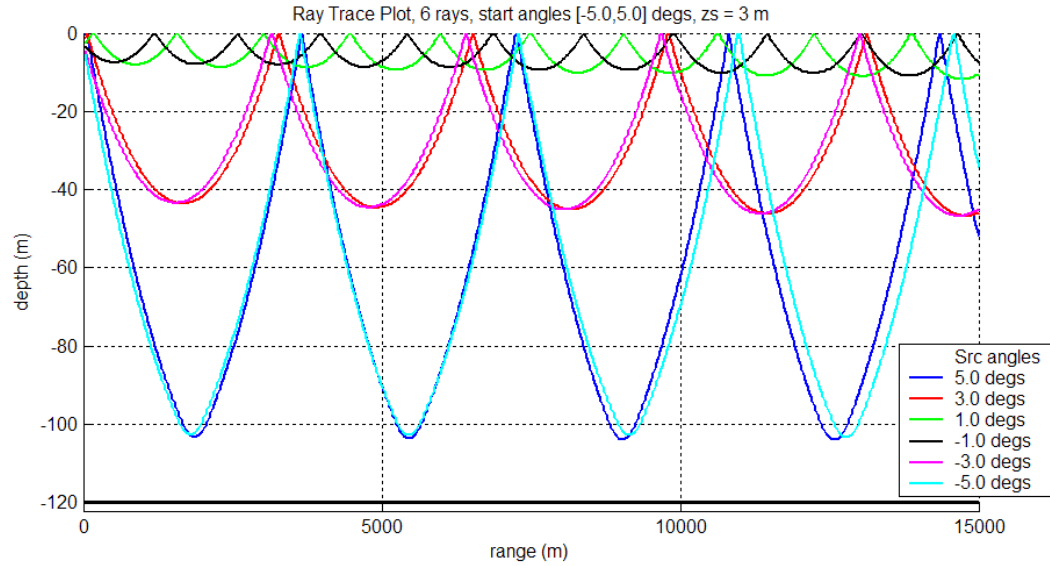


Figure 52. Ray trace for environment #2, $z_s = 3$ m

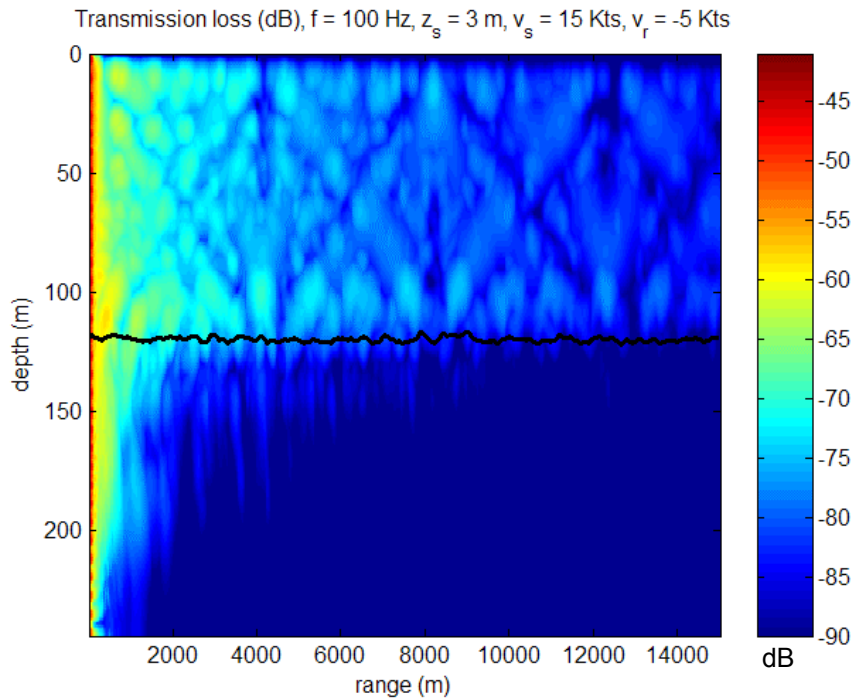


Figure 53. Minimum transmission loss across frequency vs range and depth for environment # 2, $z_s = 3$ m, $v_s = 15$ kts, $v_r = -5$ kts

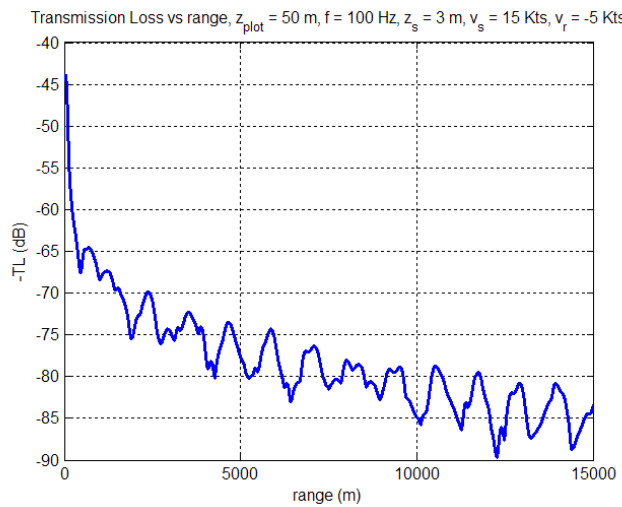


Figure 54. Minimum transmission loss across frequency vs range for environment # 2, $z_s = 3$ m, $z_r = 50$ m, $v_s = 15$ kts, $v_r = -5$ kts

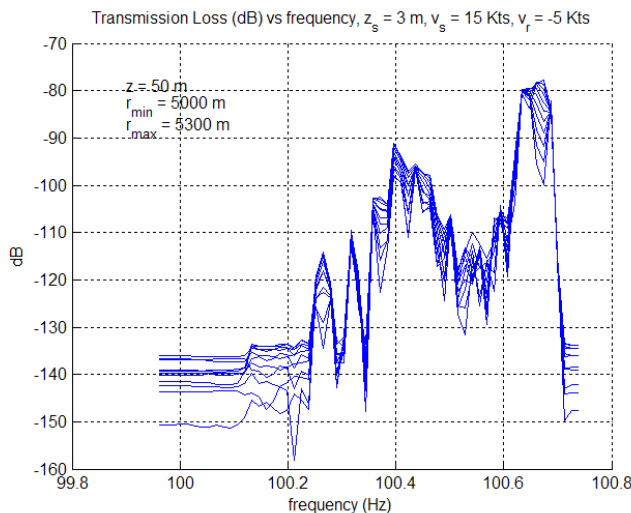


Figure 55. Transmission loss vs frequency, environment #2, $z_s = 3$ m, $z_r = 50$ m, $5000 \text{ m} < r < 5300 \text{ m}$, $v_s = 15$ kts, $v_r = -5$ kts

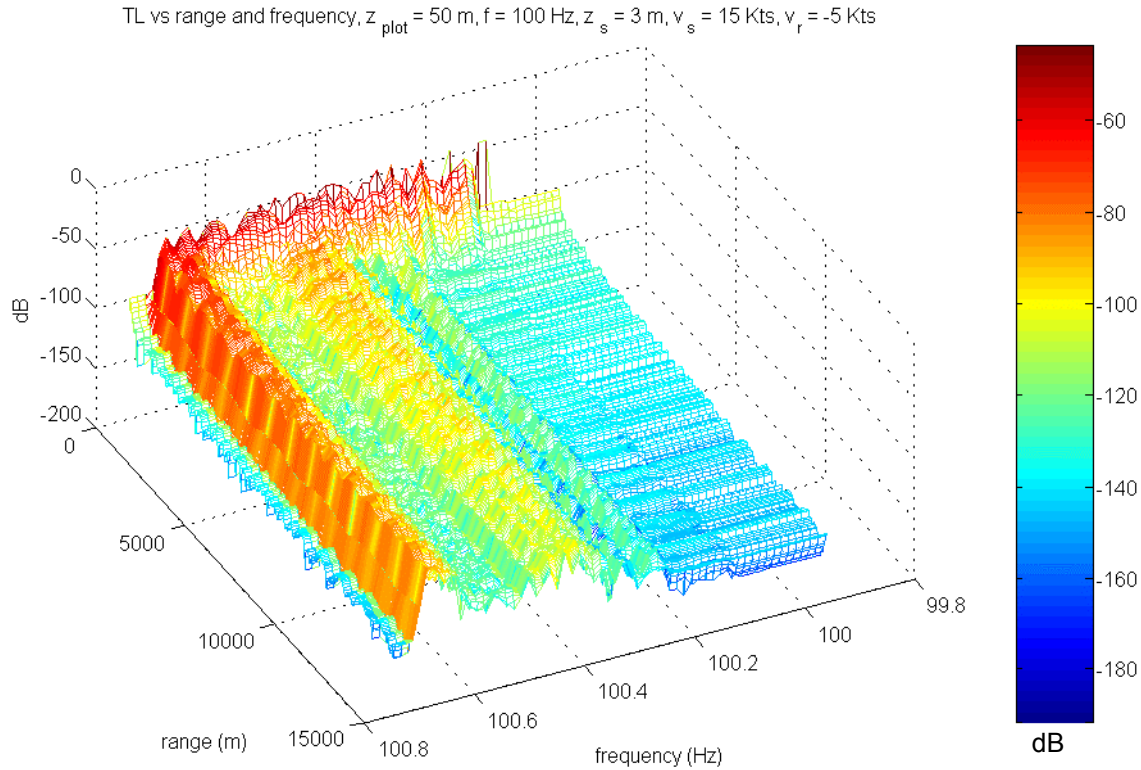


Figure 56. Transmission loss vs frequency and range, environment #2, $z_s = 3 \text{ m}$, $z_r = 50 \text{ m}$, $v_s = 15 \text{ kts}$, $v_r = -5 \text{ kts}$

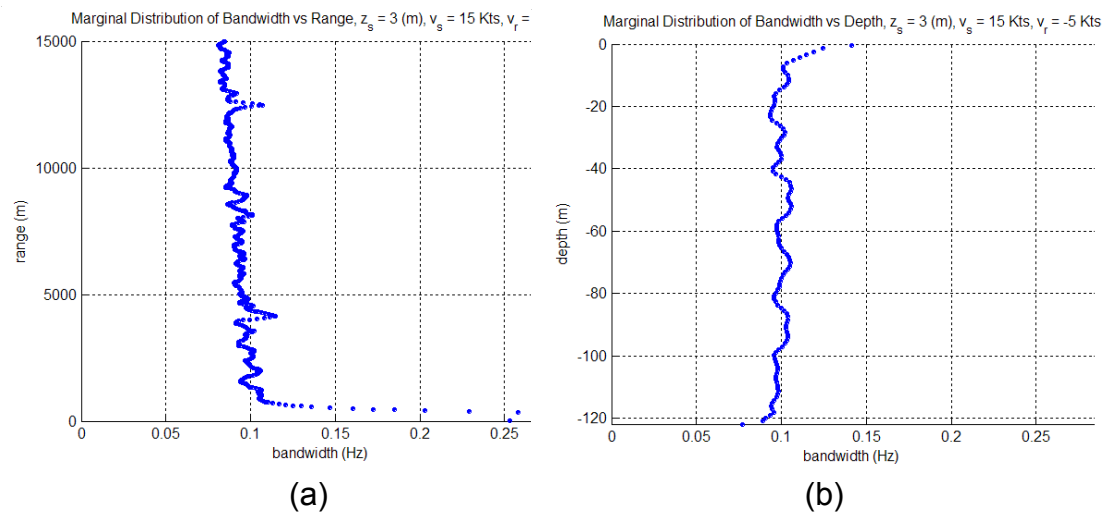


Figure 57. Marginalized bandwidth vs range (a), and depth (b) , environment #2, $z_s = 3 \text{ m}$, $v_s = 15 \text{ kts}$, $v_r = -5 \text{ kts}$

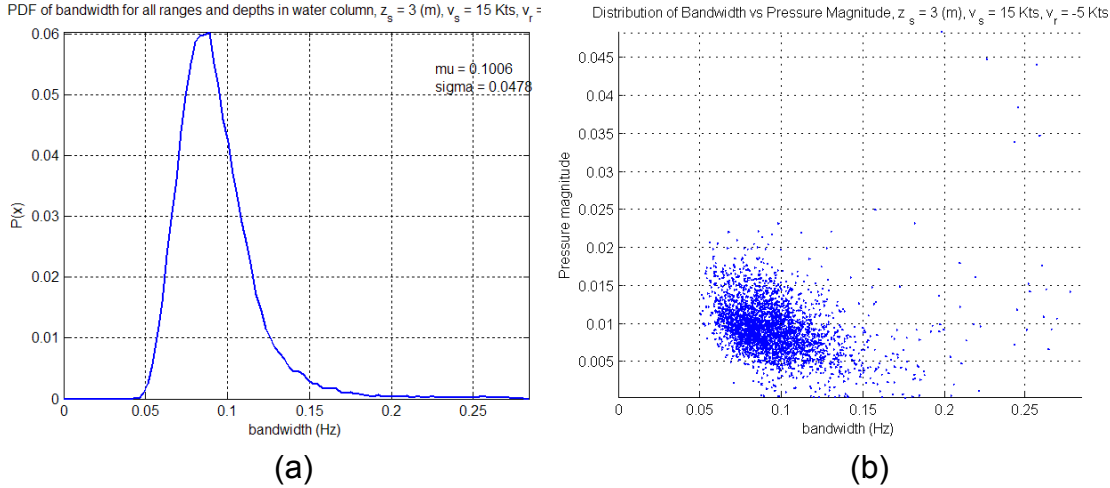


Figure 58. Aggregate histogram (a) and scatter plot vs normalized linear TL (b), environment #2, $z_s = 3$ m, $v_s = 15$ kts, $v_r = -5$ kts

3. Environment #3

The next two environments demonstrate the characteristics of received bandwidth when the ocean depth is range-dependent. The depth-dependent acoustic parameters for environment #3 are plotted in Fig. 59. Figures 60-67 contain results when the source depth is 50 m. Figures 68-74 provide the results when the source depth is 3 m. The ray trace in Fig. 60 shows a mini convergence zone (with some bottom bounce at steeper angles) in the first 8-9 km, followed by multiple bottom bounces in the last 5 km when the ocean depth becomes shallow. Figure 68 demonstrates bottom bounce propagation at smaller launch angles when the source is shallow. The TL versus range and depth plot in Fig. 62 again indicates fairly shallow angle propagation when the source is deep. This contrasts with the much steeper propagation illustrated in Fig. 69 in the first 10000 m.

The frequency versus range TL response given in Figs. 64-65 (deep source) and 71-72 (shallow source) possess a wider main component and more consistent broadband pedestal when the source is shallow than when it is deep. In Fig. 67a, the mean BW for the deep source has been computed to be about 0.06 Hz. When the source is shallow, Fig. 74a indicates a slightly larger mean

BW of about 0.09 Hz, consistent with the behavior observed in the first two environments. The scatter plots in Figs. 67b and 74b indicate a unimodal dependence upon local magnitude when the source is deep, but a somewhat bimodal structure when the source is shallow. This will be discussed in more detail below.

A unique characteristic of this range-dependent environment is related to a fairly substantial dependence of the BW parameter on range and depth. This can be observed in Figs. 66 and 73, regardless of the source depth. Specifically, the BW undergoes a significant decrease after a range of about 10000 m, and above a depth of 200 m. This corresponds to propagation above the shallow plateau during the last 5000 m of range. The TL responses in Figs. 62 and 69 indicate that acoustic propagation above this shelf occurs with fairly low grazing angles, even though the ray trace in Fig. 60 might suggest otherwise. It is possible that propagation angles increased past the critical angle once the wave-front passed over the shallow shelf, and thus rapidly attenuated. Thus, in this environment, the bottom profile actually appears to filter high angle propagation at the long ranges causing the bandwidth to decrease during this latter segment of range. The differences noted in the mean BW (across all range and depth cells), in Figs. 67 and 74, are likely due to the preponderance of high angle propagation in the first 10000 m that occurs when the source is shallow.

The marked difference in propagation angles during the first 10000 m and the latter 5000 m when the source is shallow is probably the cause of the bimodality in the histogram and scatter plots noted above. When the source is deep, the propagation angles are more consistent over range, resulting in a more unimodal density function. This numerical experiment has allowed us to observe several interesting impacts on the characteristics of the bandwidth parameter, when the environment has more complicated range-dependent attributes.

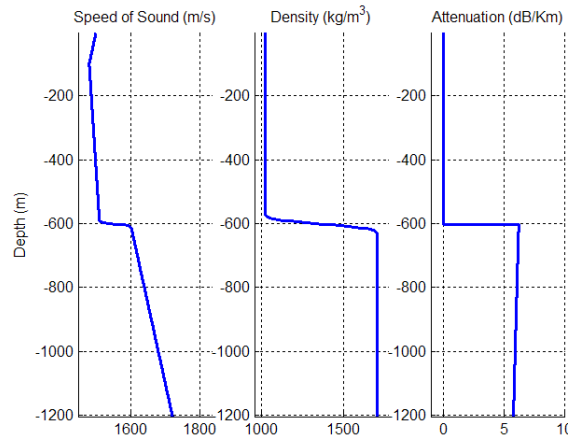


Figure 59. Acoustic parameters for environment #3

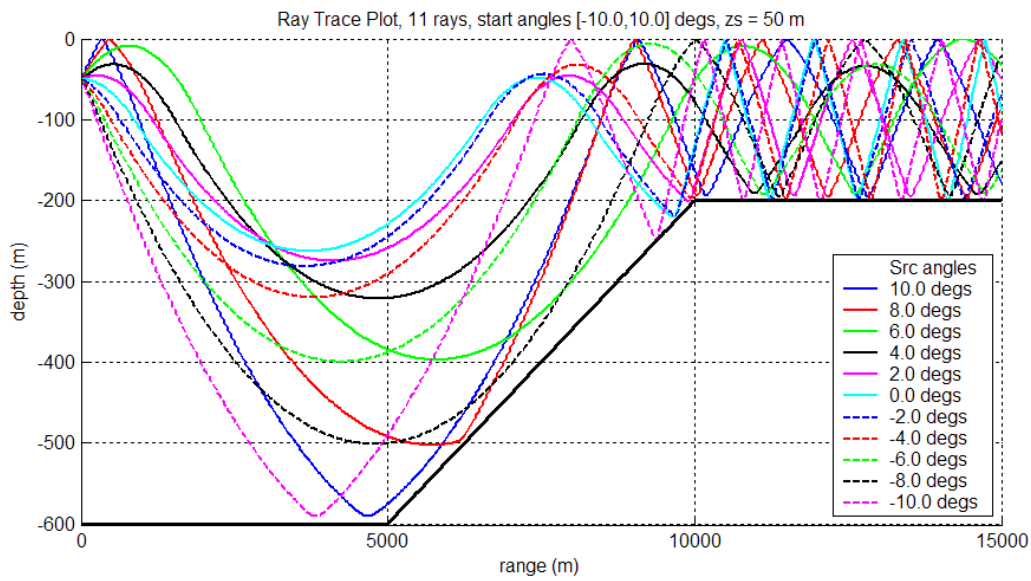


Figure 60. Ray trace for environment #3, $z_s = 50$ m

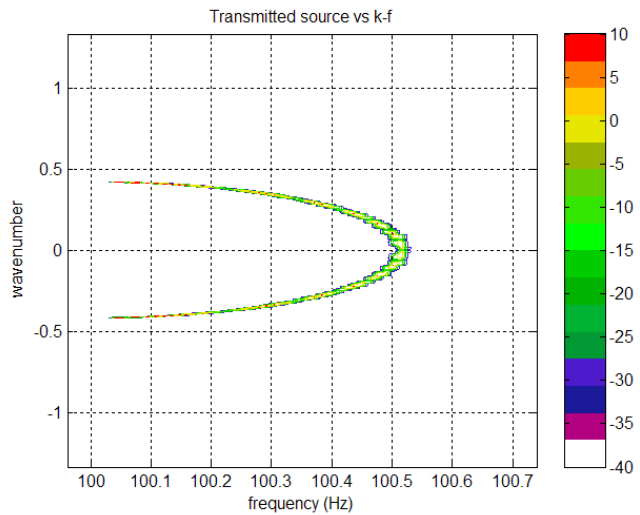


Figure 61. k - f spectrum of source in environment # 3, $z_s = 50$ m, $v_s = 15$ kts

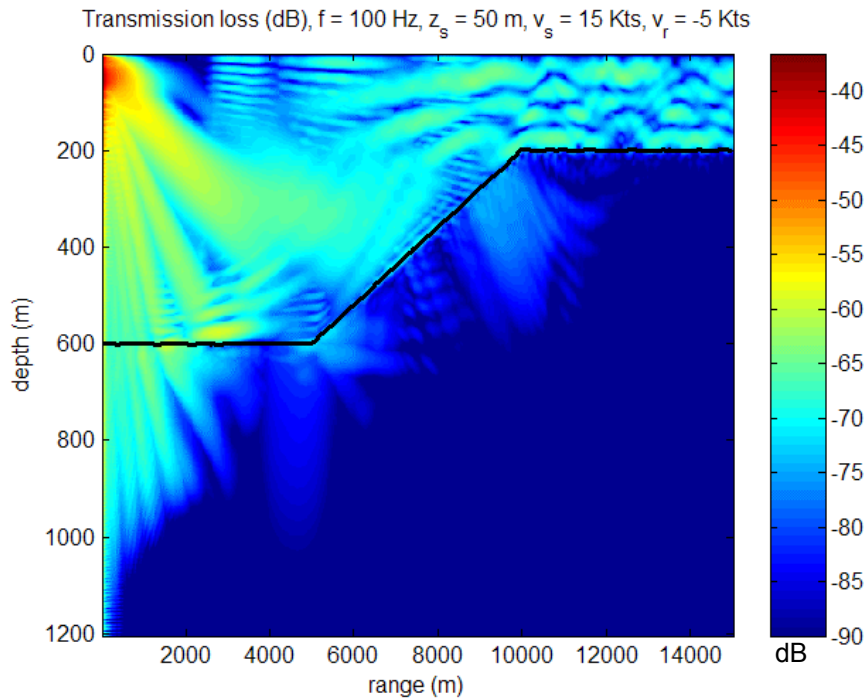


Figure 62. Minimum transmission loss across frequency vs range and depth for environment # 3, $z_s = 50$ m, $v_s = 15$ kts, $v_r = -5$ kts

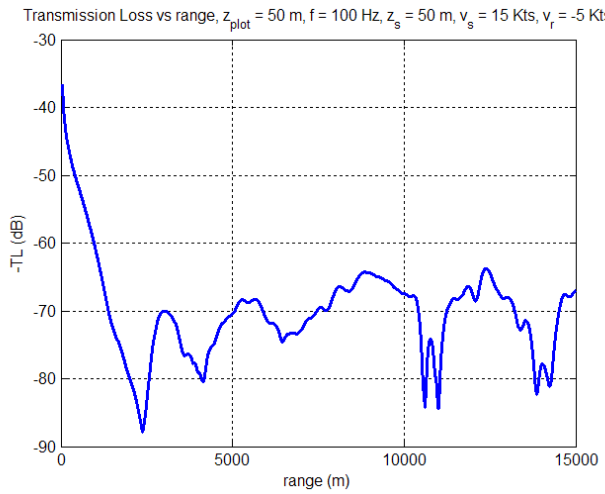


Figure 63. Minimum transmission loss across frequency vs range for environment # 3, $z_s = 50 \text{ m}$, $z_r = 50 \text{ m}$, $v_s = 15 \text{ kts}$, $v_r = -5 \text{ kts}$

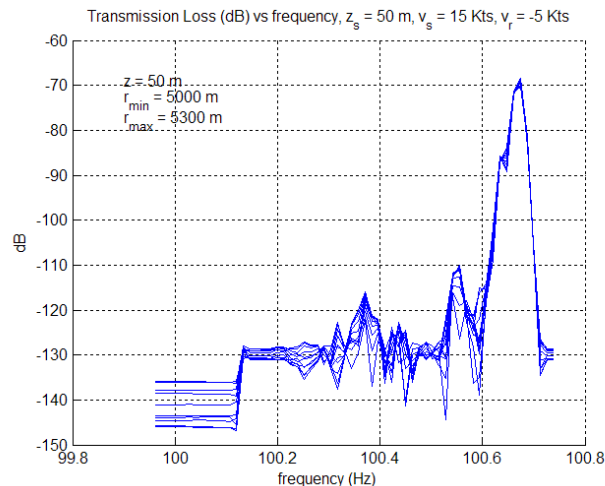


Figure 64. Transmission loss vs frequency, environment #3, $z_s = 50 \text{ m}$, $z_r = 50 \text{ m}$, $5000 \text{ m} < r < 5300 \text{ m}$, $v_s = 15 \text{ kts}$, $v_r = -5 \text{ kts}$

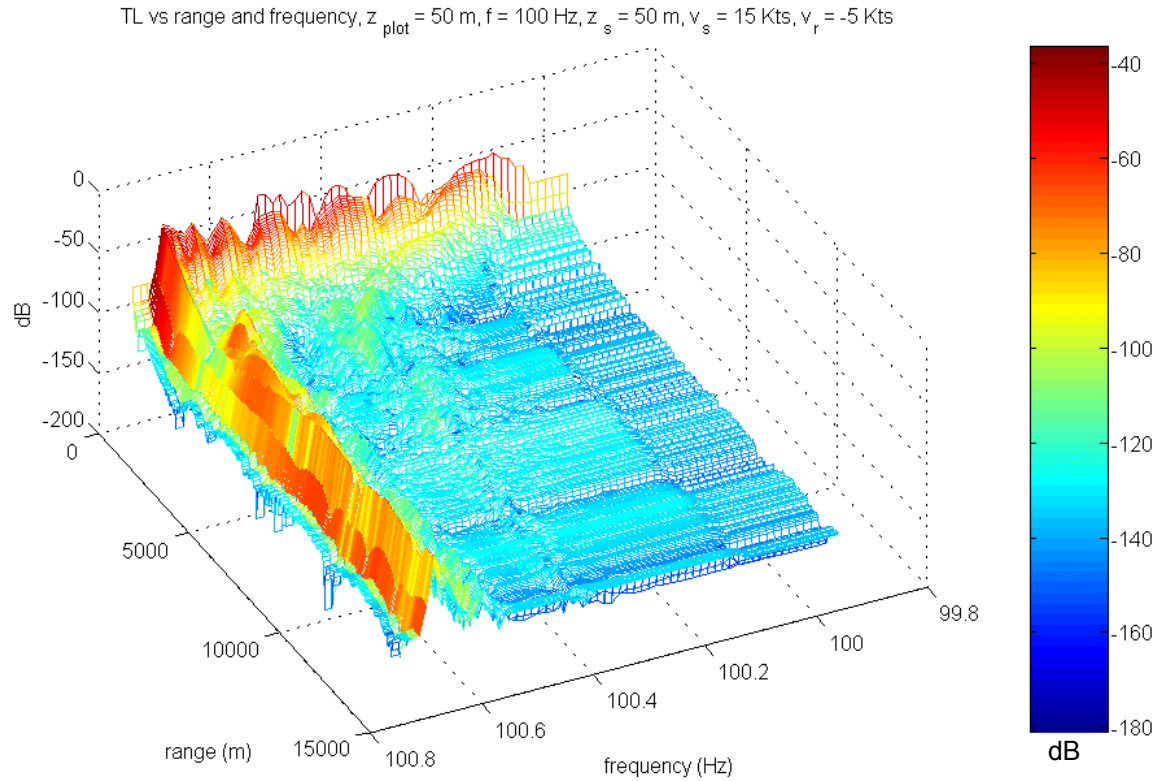


Figure 65. Transmission loss vs frequency and range, environment #3, $z_s = 50 \text{ m}$, $z_r = 50 \text{ m}$, $v_s = 15 \text{ kts}$, $v_r = -5 \text{ kts}$

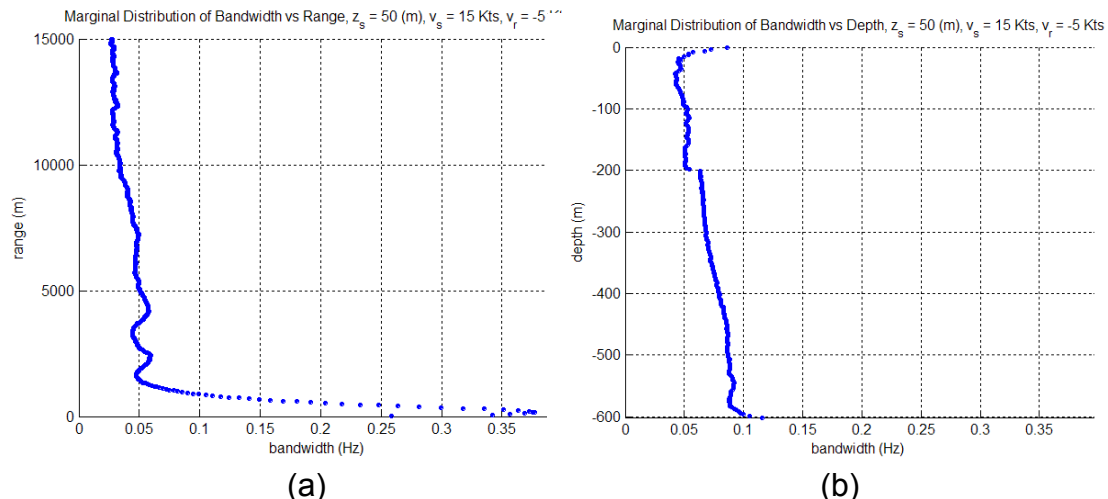


Figure 66. Marginalized bandwidth vs range (a), and depth (b), environment #3, $z_s = 50 \text{ m}$, $v_s = 15 \text{ kts}$, $v_r = -5 \text{ kts}$

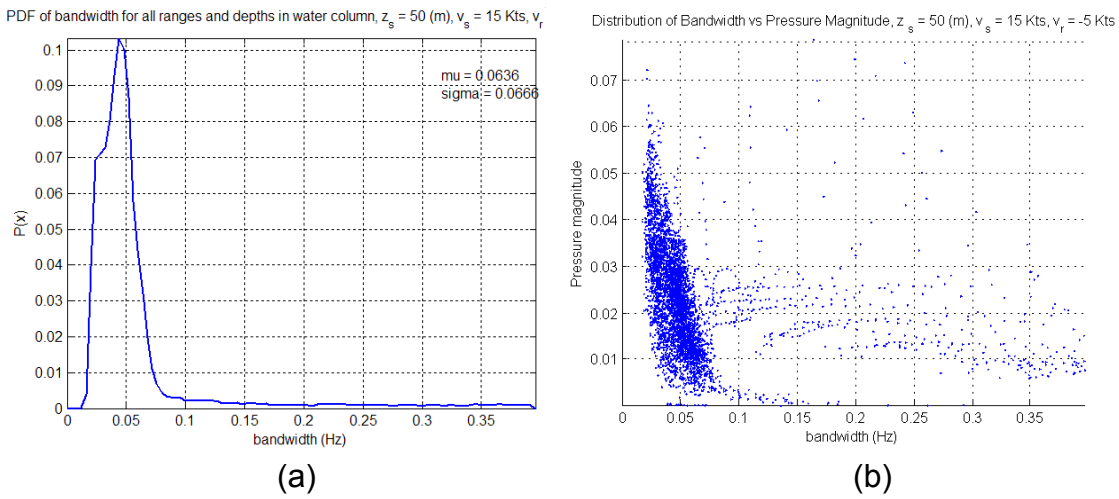


Figure 67. Aggregate histogram (a) and scatter plot vs normalized linear TL (b), environment #3, $z_s = 50$ m, $v_s = 15$ kts, $v_r = -5$ kts

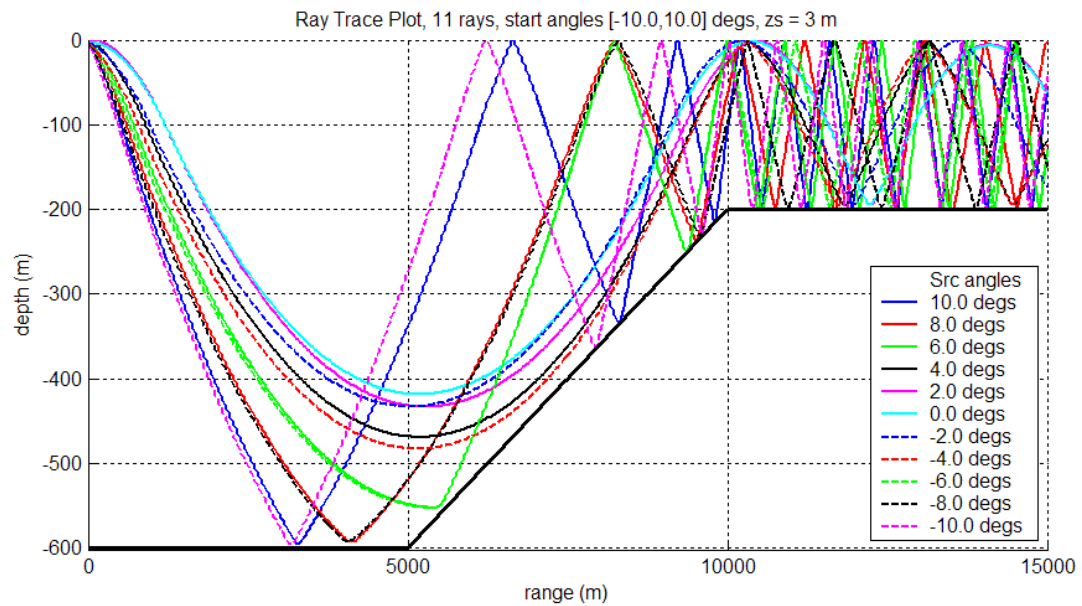


Figure 68. Ray trace for environment #3, $z_s = 3$ m

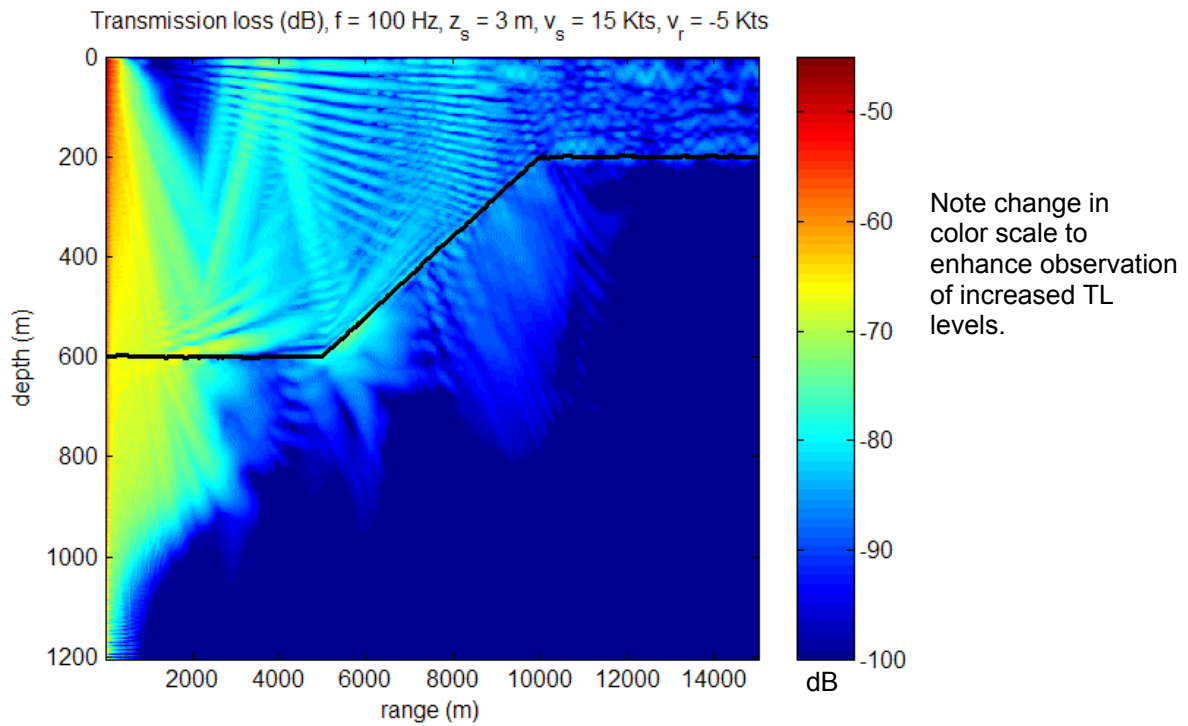


Figure 69. Minimum transmission loss across frequency vs range and depth for environment # 3, $z_s = 3$ m, $v_s = 15$ kts, $v_r = -5$ kts

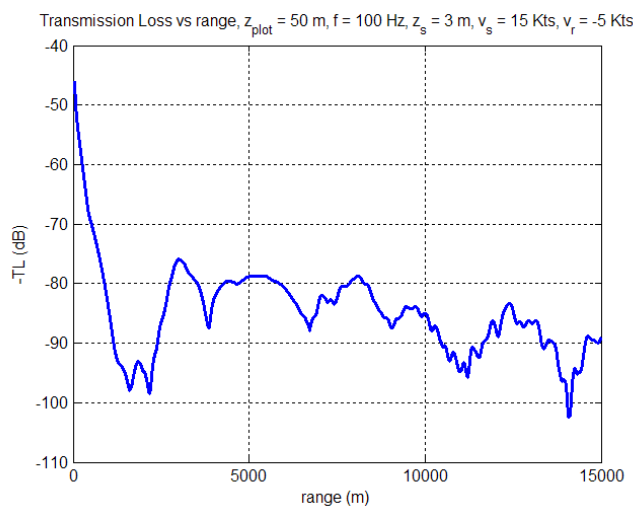


Figure 70. Minimum transmission loss across frequency vs range for environment # 3, $z_s = 3$ m, $z_r = 50$ m, $v_s = 15$ kts, $v_r = -5$ kts

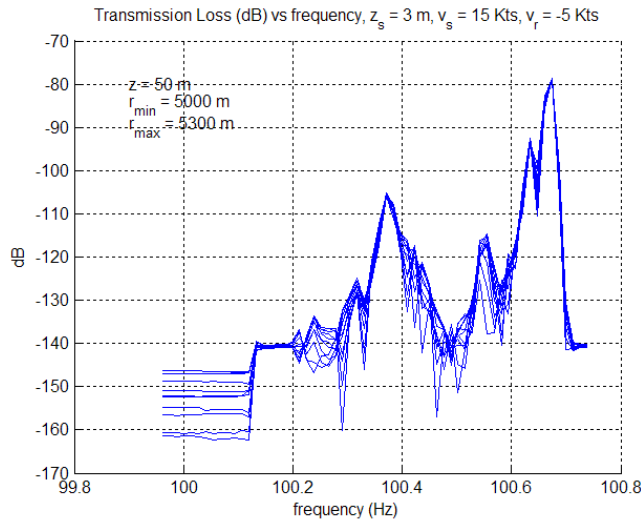


Figure 71. Transmission loss vs frequency, environment #3, $z_s = 3 \text{ m}$, $z_r = 50 \text{ m}$, $5000 \text{ m} < r < 5300 \text{ m}$, $v_s = 15 \text{ kts}$, $v_r = -5 \text{ kts}$

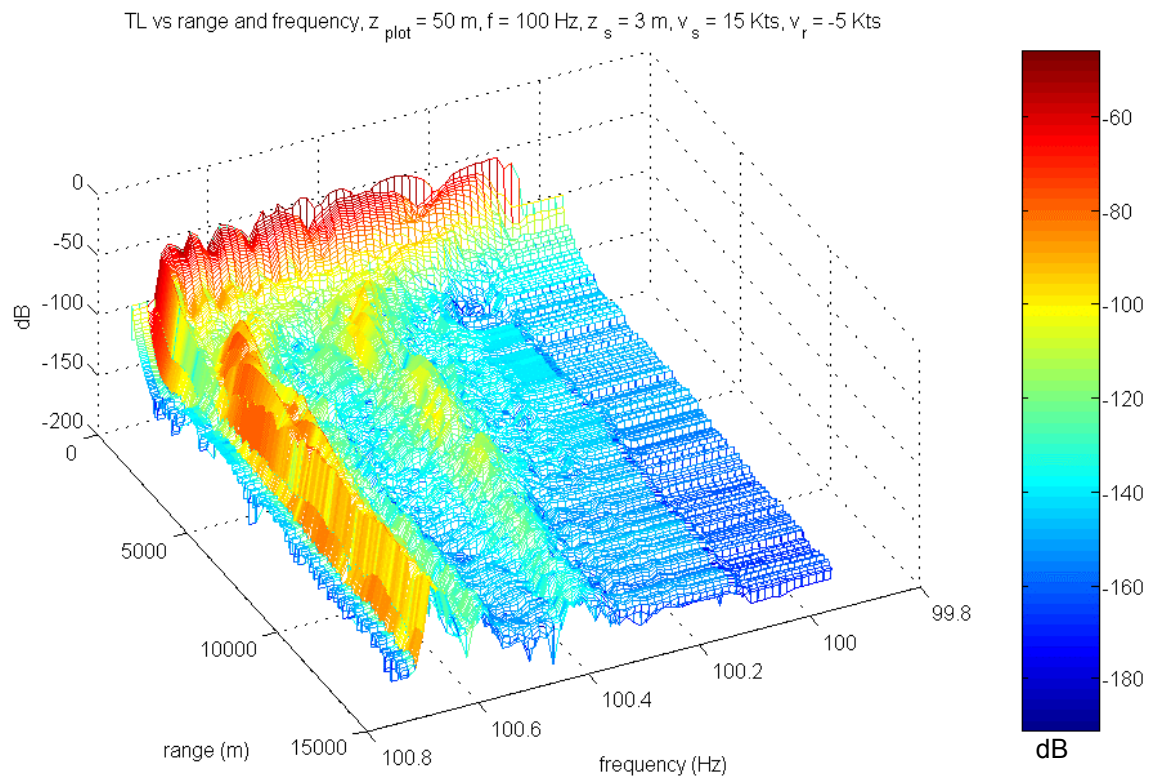


Figure 72. Transmission loss vs frequency and range, environment #3, $z_s = 3 \text{ m}$, $z_r = 50 \text{ m}$, $v_s = 15 \text{ kts}$, $v_r = -5 \text{ kts}$

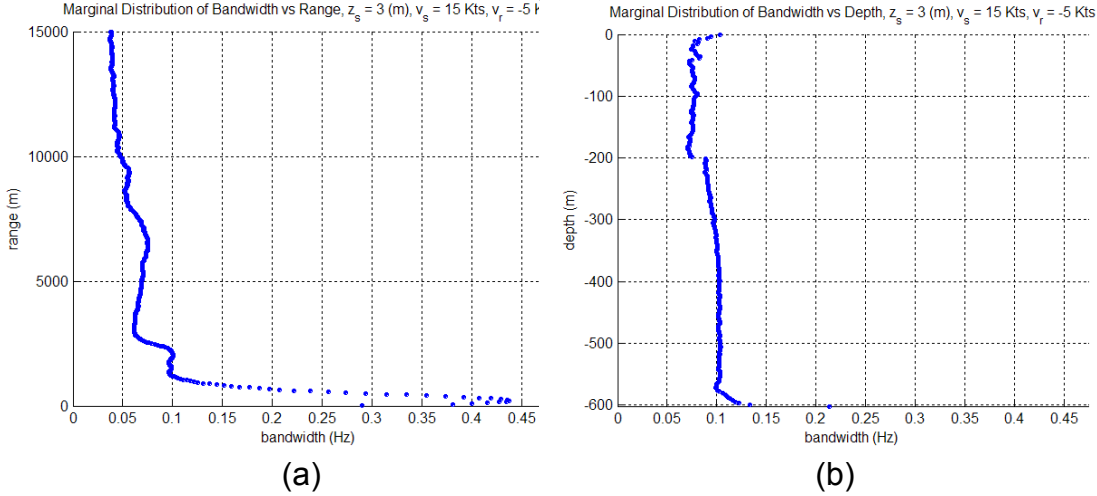


Figure 73. Marginalized bandwidth vs range (a), and depth (b), environment #3, $z_s = 3$ m, $v_s = 15$ kts, $v_r = -5$ kts

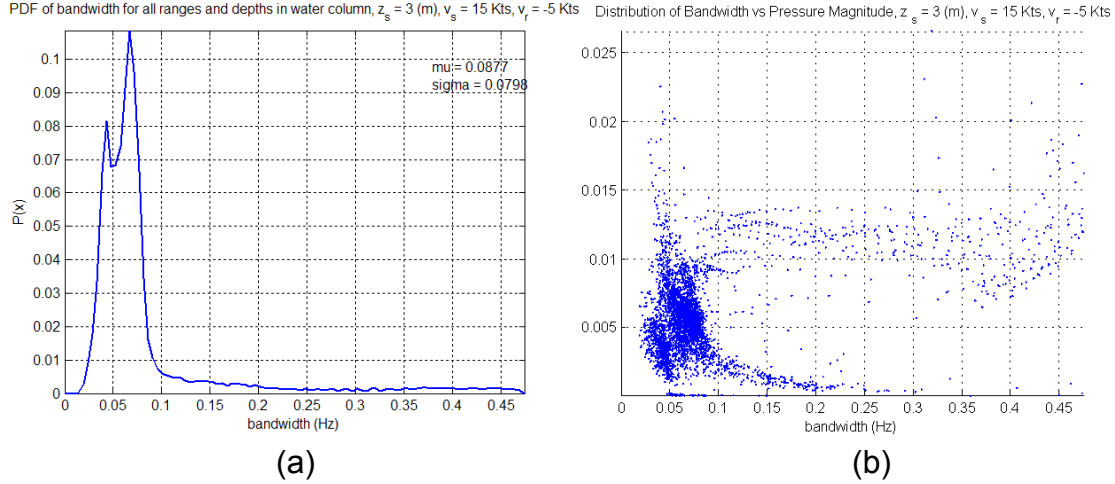


Figure 74. Aggregate histogram (a) and scatter plot vs normalized linear TL (b), environment #3, $z_s = 3$ m, $v_s = 15$ kts, $v_r = -5$ kts

4. Environment #4

The final environment is designed to demonstrate the characteristics of received bandwidth in a fairly deep, but range-dependent ocean, such as may be encountered near shelf break regions. The depth dependent acoustic parameters for this environment are illustrated in Fig. 75. A ray trace from a source depth of 50 m, depicted in Fig. 76, shows convergence zone (CZ) propagation in the first 30000 m, followed by multiple bottom bounces above the shallow shelf. When

the source is shallow, Fig. 84 indicates that the CZ is augmented with a deep bottom bounce path. The minimum TL response, given in Figs. 77 (for the deep source), and 85 (for the shallow source), are consistent with the ray traces. Similar to the other environments, propagation with higher vertical angles can be observed when the source is shallow vice deep. Figures 78 and 86 illustrate a fairly deep shadow zone at the shallow depths between a range of about 5000 and 18000 m for both the deep and shallow source cases.

The transmission loss versus frequency and range is presented in Figs. 81 (for the deep source) and 88 (for the shallow source). In this deep ocean environment, these plots are very similar. They show significant structure at the short ranges, followed by a pronounced dip in magnitude at the shadow zone; and then a resurgence of narrowband structure at the longer ranges. The level versus frequency plots in Figs. 80 and 87 (for the deep and shallow sources, respectively) illustrate a flat TL response within the shadow zone.

The bandwidth estimates versus range and depth are plotted in Figs. 82 for the deep source. A similar set of plots is contained in Fig. 89 for the shallow source. Comparison of Figs. 83a and 90a show that the mean bandwidth is approximately 0.07 Hz when the source is shallow, and 0.05 Hz when the source is deep. Thus, the shallow source is again associated with an increase in bandwidth, although the increase is modest in this deep water environment. The scatter plots in Figs. 83b and 90b also illustrate significant differences in the dependency of BW on normalized pressure magnitude. Although it is difficult to attribute a physical meaning to this characteristic, it is possible that the differences could be exploited by an automatic classification scheme.

An interesting feature of the marginalized plots (Figs. 82 and 89) is that the BW tends to decrease at the longer ranges, while increasing at shallower depths. This behavior is counter-intuitive because the bottom profile requires that the shallower depths occur at long ranges. The reason for this can be understood by observing a color coded presentation of bandwidth for all ranges and depths, produced for the case when the source is at 3 m. This plot, in Fig. 91, shows that

a concentration of high bandwidth occurs in the entire shadow zone, consistent with the plots shown in Figs. 80 and 87. Thus, average bandwidth over all depths versus range will tend to be higher at the shorter ranges. However, when averaging over range, the bandwidth will be higher at the shallower depths. This also shows that even though the model predicts significant bandwidths in particular parts of the ocean, sometimes the TL is so high that signals with this bandwidth will only be observable when the levels of the radiating source are extremely high.

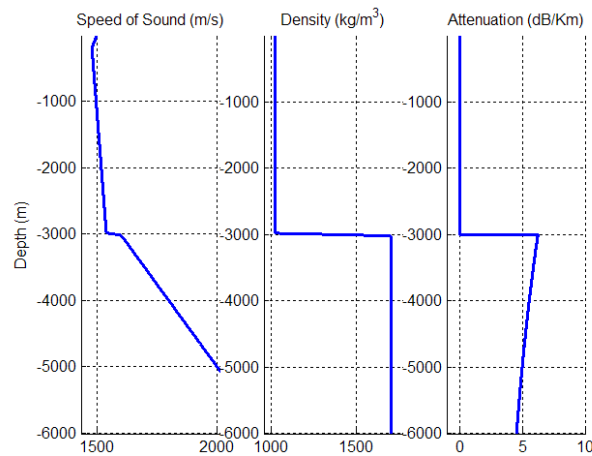


Figure 75. Acoustic parameters for environment #4

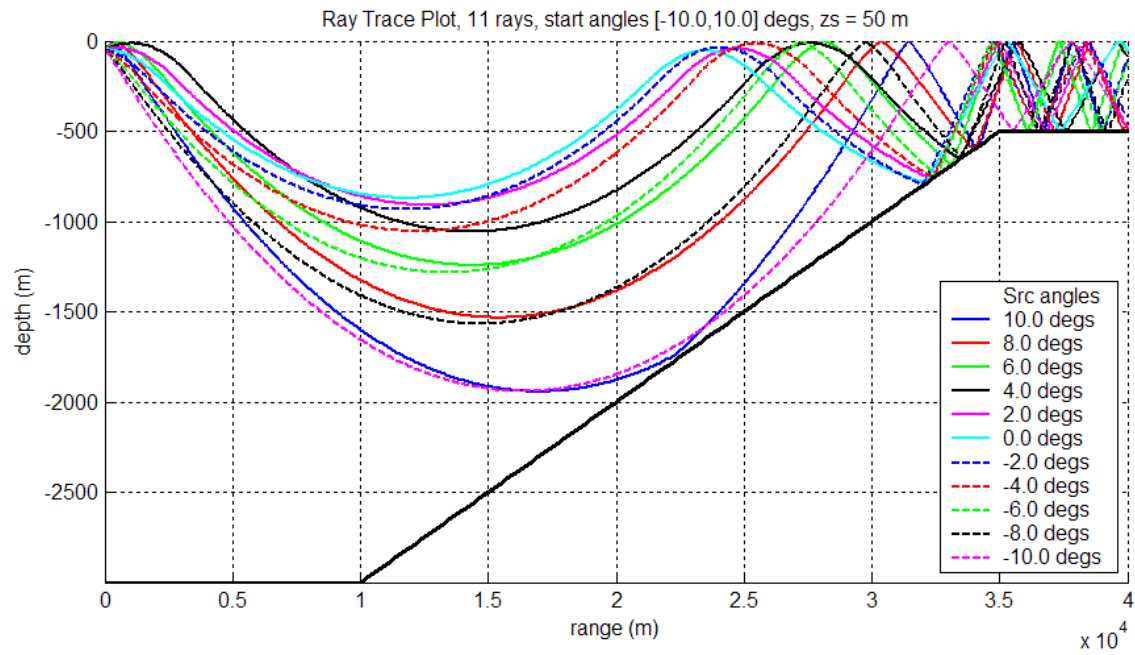


Figure 76. Ray trace for environment #4, $z_s = 50$ m

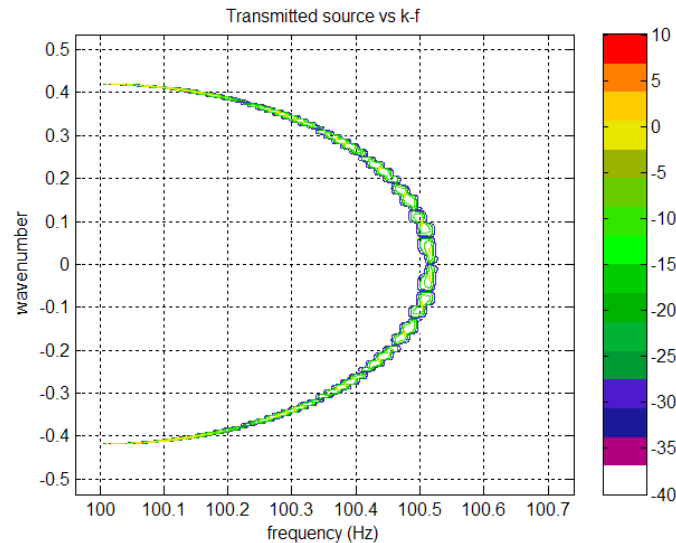


Figure 77. k-f spectrum of source in environment # 4, $z_s = 50$ m, $v_s = 15$ kts

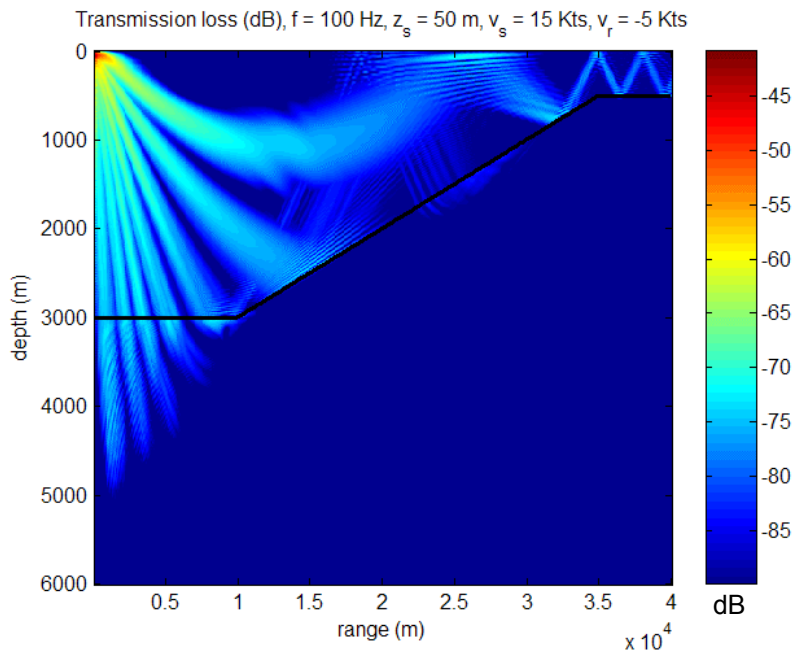


Figure 78. Minimum transmission loss across frequency vs range and depth for environment # 4, $z_s = 50$ m, $v_s = 15$ kts, $v_r = -5$ kts

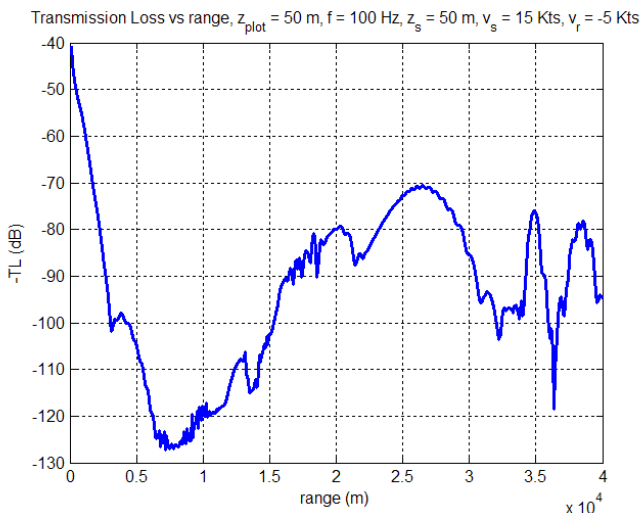


Figure 79. Minimum transmission loss across frequency vs range for environment # 4, $z_s = 50$ m, $z_r = 50$ m, $v_s = 15$ kts, $v_r = -5$ kts

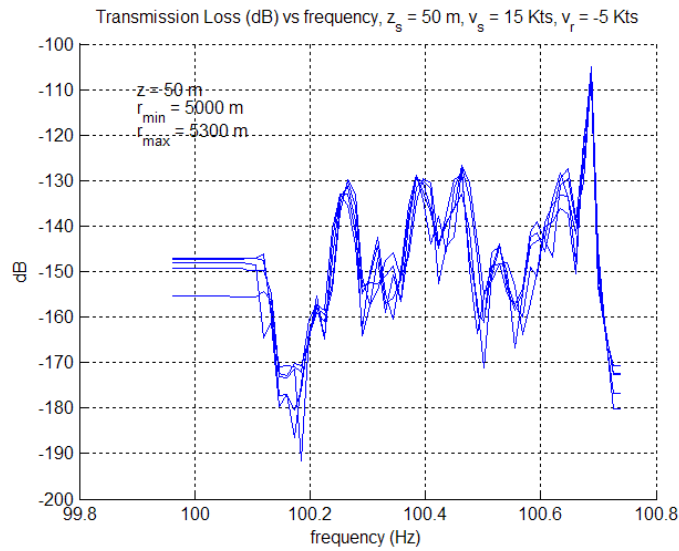


Figure 80. Transmission loss vs frequency, environment #4, $z_s = 50$ m, $z_r = 50$ m, $5000 \text{ m} < r < 5300 \text{ m}$, $v_s = 15$ kts, $v_r = -5$ kts

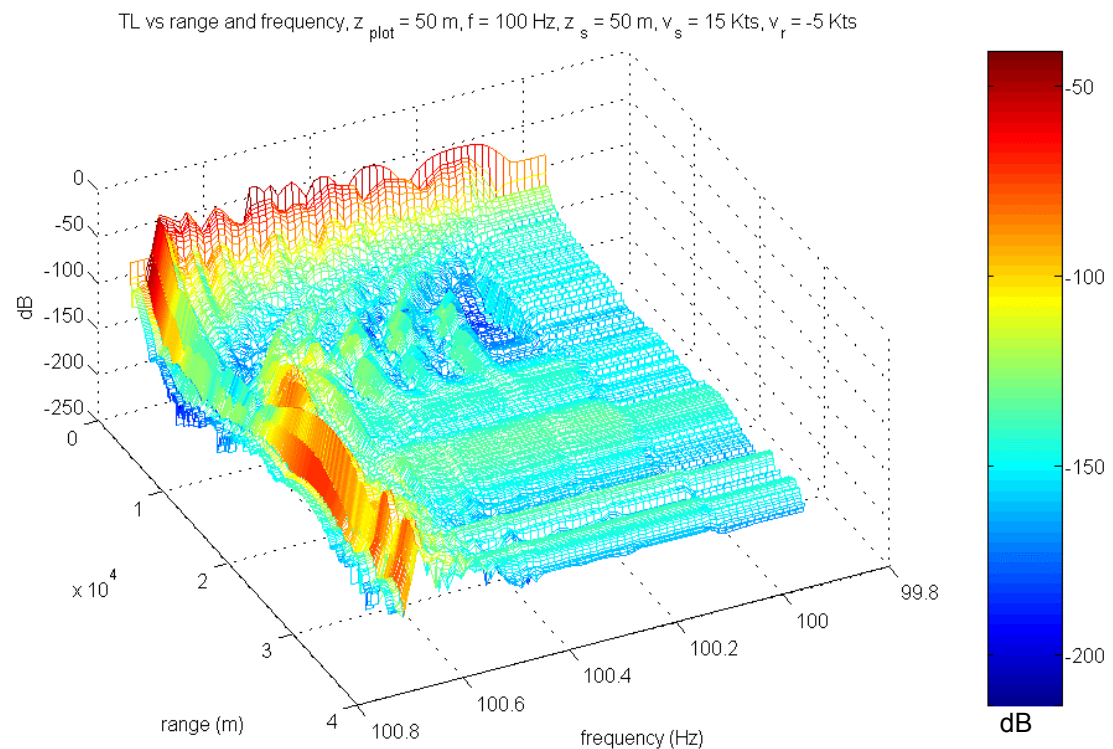


Figure 81. Transmission loss vs frequency and range, environment #4, $z_s = 50$ m, $z_r = 50$ m, $v_s = 15$ kts, $v_r = -5$ kts

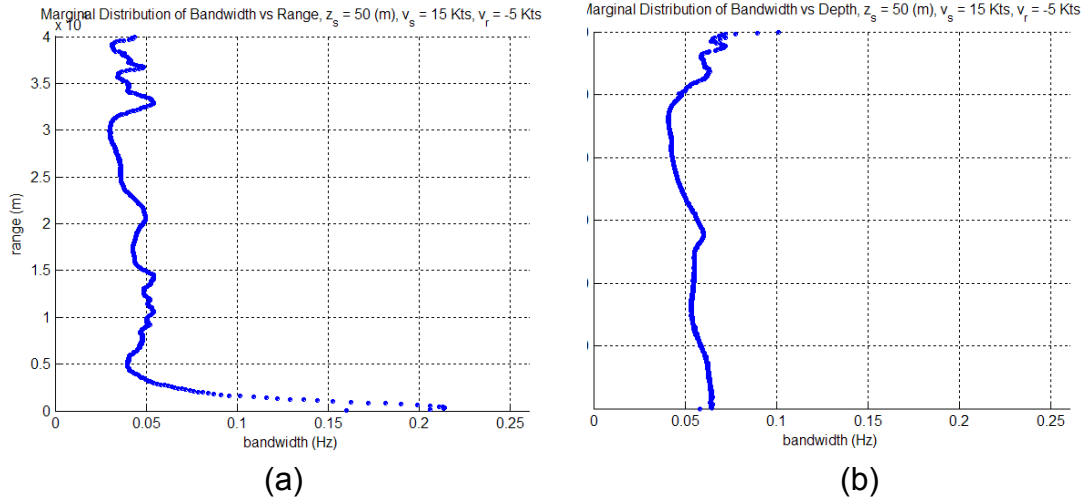


Figure 82. Marginalized bandwidth vs range (a), and depth (b), environment #4, $z_s = 50$ m, $v_s = 15$ kts, $v_r = -5$ kts

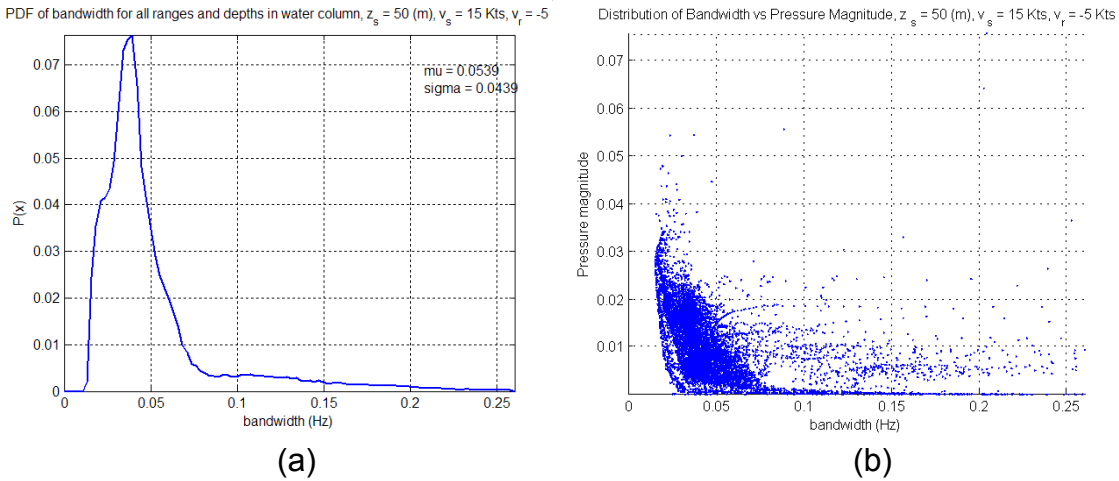


Figure 83. Aggregate histogram (a) and scatter plot vs normalized linear TL (b), environment #4, $z_s = 50$ m, $v_s = 15$ kts, $v_r = -5$ kts

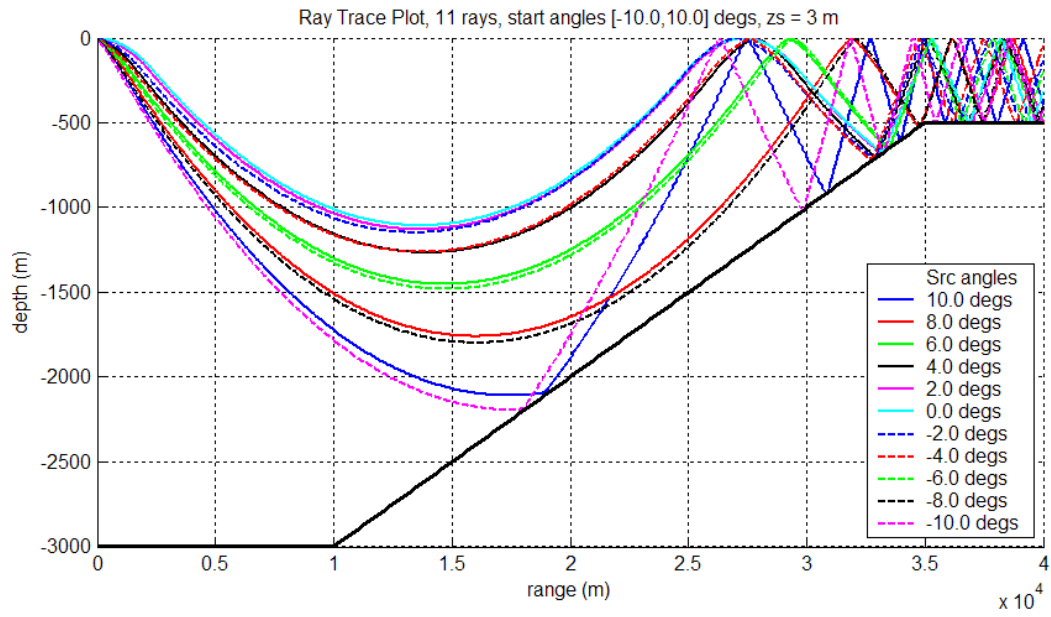


Figure 84. Ray trace for environment #4, $z_s = 3$ m

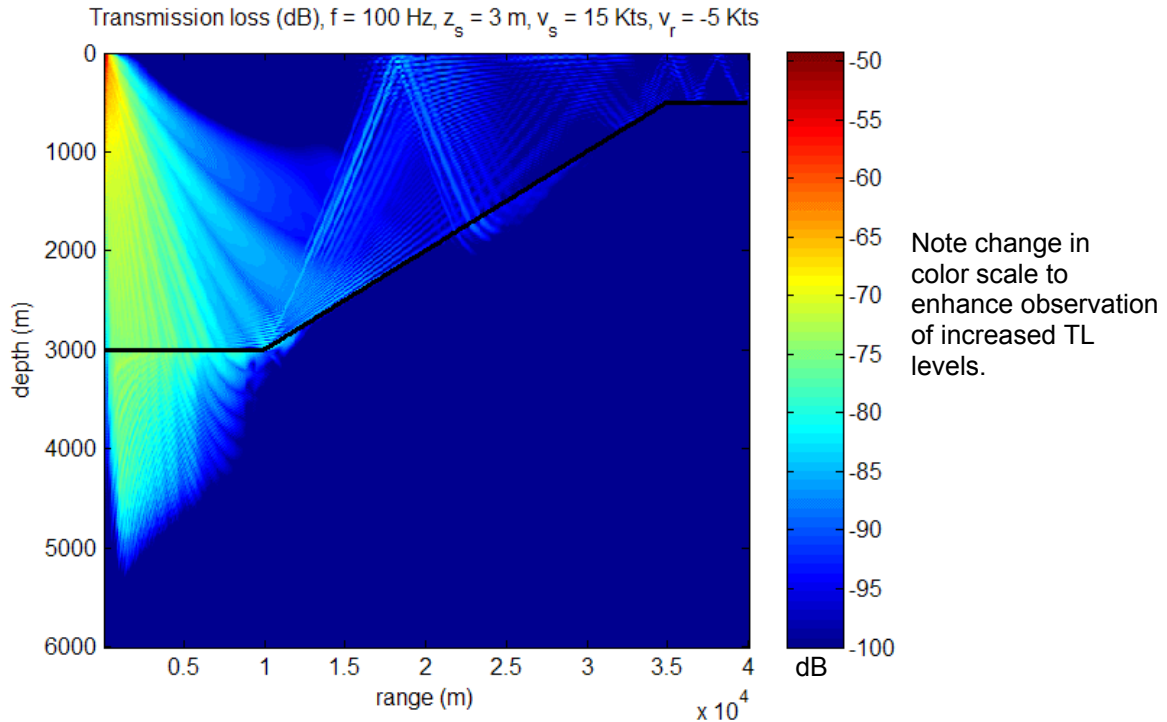


Figure 85. Minimum transmission loss across frequency vs range and depth for environment # 4, $z_s = 3$ m, $v_s = 15$ kts, $v_r = -5$ kts

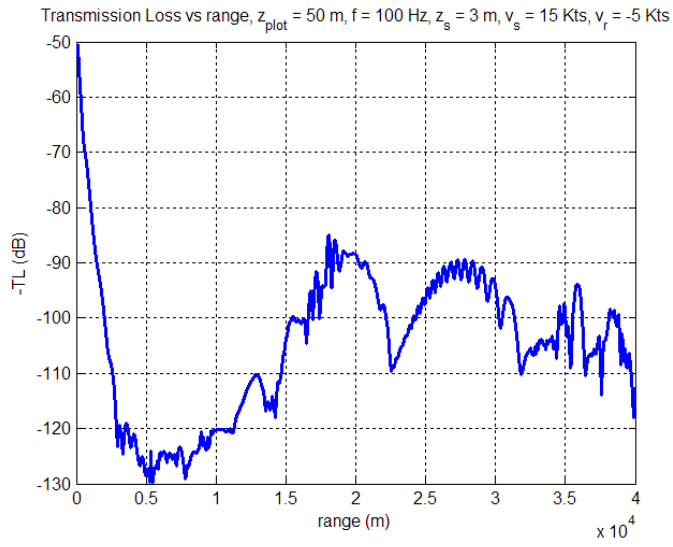


Figure 86. Minimum transmission loss across frequency vs range for environment # 4, $z_s = 3 \text{ m}$, $z_r = 50 \text{ m}$, $v_s = 15 \text{ kts}$, $v_r = -5 \text{ kts}$

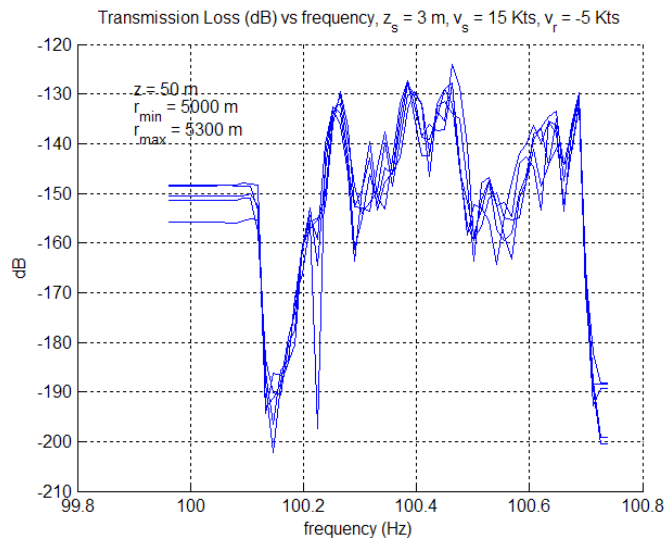


Figure 87. Transmission loss vs frequency, environment #4, $z_s = 3 \text{ m}$, $z_r = 50 \text{ m}$, $5000 \text{ m} < r < 5300 \text{ m}$, $v_s = 15 \text{ kts}$, $v_r = -5 \text{ kts}$

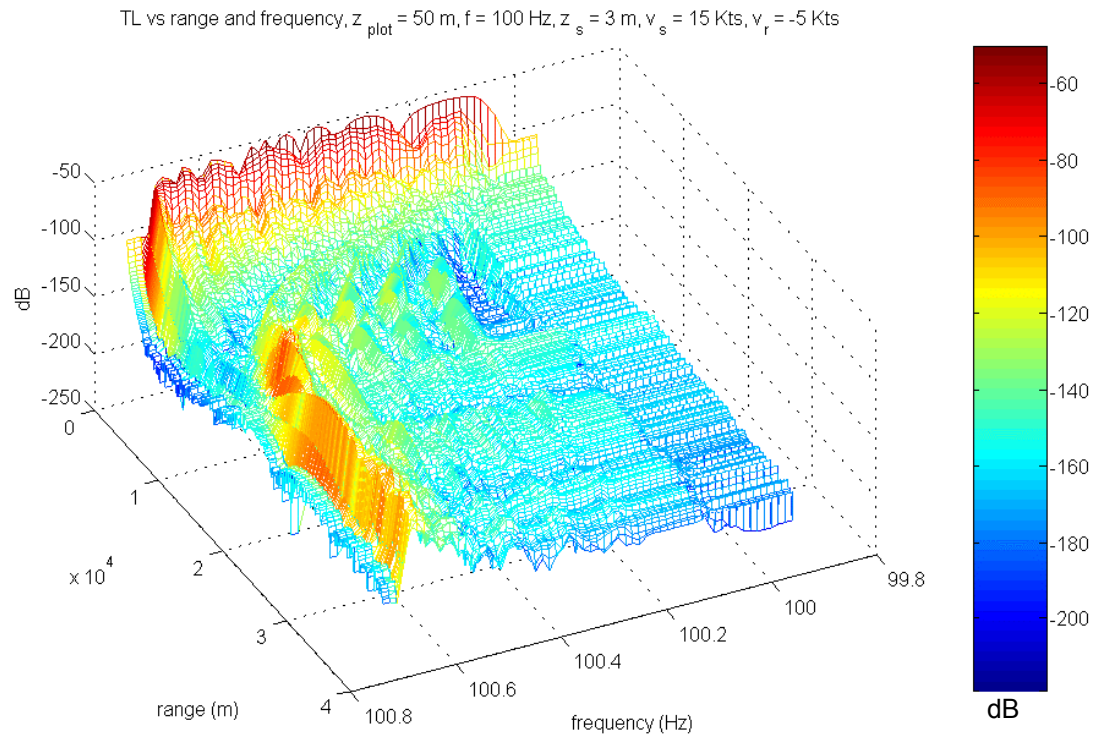


Figure 88. Transmission loss vs frequency and range, environment #4, $z_s = 3 \text{ m}$, $z_r = 50 \text{ m}$, $v_s = 15 \text{ kts}$, $v_r = -5 \text{ kts}$

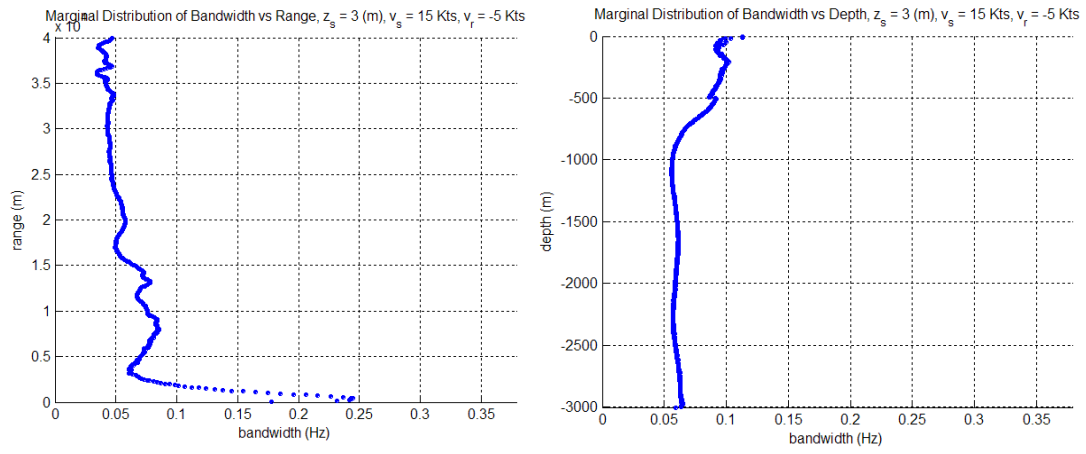


Figure 89. Marginalized bandwidth vs range (a), and depth (b), environment #4, $z_s = 3 \text{ m}$, $v_s = 15 \text{ kts}$, $v_r = -5 \text{ kts}$

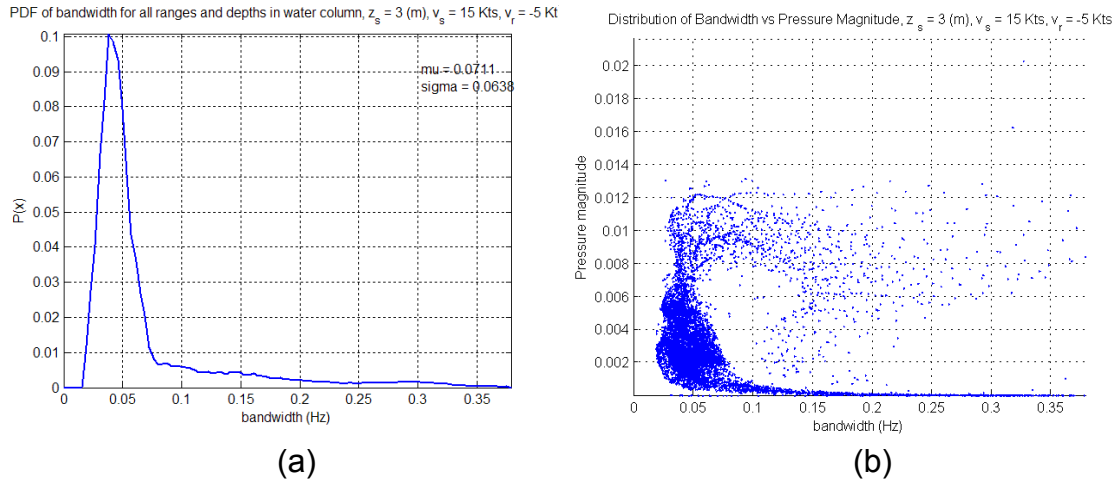


Figure 90. Aggregate histogram (a) and scatter plot vs normalized linear TL (b), environment #4, $z_s = 3$ m, $v_s = 15$ kts, $v_r = -5$ kts

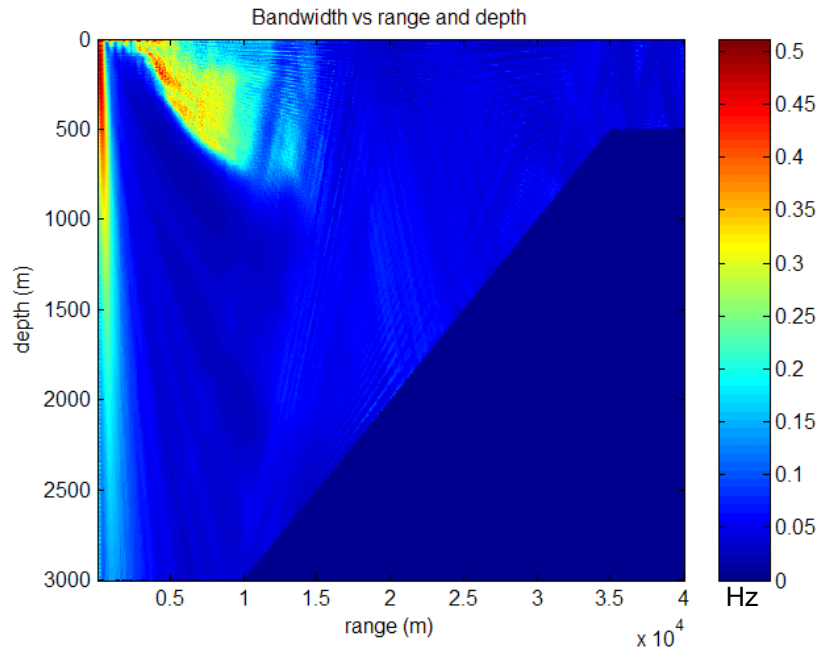


Figure 91. Color coded plot of bandwidth vs range and depth for environment #4, $z_s = 3$ m, $v_s = 15$ kts, $v_r = -5$ kts

VII. CONCLUSIONS

We have developed an implementation of a PE acoustic propagation model, including a set of metrics and statistical tools, to help us understand the characteristics of the bandwidth of a CW signal when transmitted from a moving source and received by a moving receiver. Plots of transmission loss versus frequency and range produced by the model are an instructive way to observe these affects across the entire environment. The automatic method of estimating bandwidth and its marginals across range and depth demonstrated consistent results that were always explainable after manual analysis of the raw data.

Executing the model on several diverse environments (defined by various acoustical parameters) with both deep and shallow source depths allowed observation of several trends. First, it was generally the case that locations within the medium corresponding to higher transmission loss were also correlated with higher bandwidths. This appears to be related to the premise that as the TL increases for the dominant paths, the ordinarily lower amplitude secondary paths (which tend to travel with higher angles of propagation) become more significant in a relative sense. A review of the differences in the main lobe of TL versus frequency plotted in Figs. 48 and 55 demonstrates this.

Next, we observed that it is possible for the shape of the range-dependent ocean depth profile to affect the tendency towards shallow or high angle propagation, and thereby influence the observed bandwidth values. For example, an ocean that transitions from deep to shallow water depths can cause higher angle modes, propagating towards the shallow end, to exceed the critical angle and attenuate rapidly. In this case, the bandwidth marginals versus range or depth will significantly decrease at the transition point. This situation can also be accompanied by a bimodality in the bandwidth versus pressure magnitude scatter plots (where pressure is inversely related to TL). Here, two competing influences are at work. Longer ranges tend to have higher TL and therefore higher bandwidths. However, in ocean environments similar to #2 and #4,

defined in Section VI, the tendency towards high angle propagation can be inversely proportional to the range. Thus we require the numerical model to sort out which type of influence will dominate.

Finally, we observed in all the environments evaluated that a source near the surface will have a higher overall bandwidth than a source located many meters below the surface. Before attaching significance to this, it is important to note that we have not yet studied this influence in its entirety, since only two different depths were evaluated in our examples. For example, it may be possible that a source near the bottom produces bandwidths that are similar to those produced by sources near the surface. We also note that only two types of (bilinear) SSPs were evaluated, and that the shape of the SSP will likely have a significant influence on the bandwidth. In the examples studied in this thesis, the depth of the source had a considerable impact on the likelihood of high angle propagation, due to the competing influences of higher sound speeds near the boundaries. It remains to be seen how robust this affect will be when the model is exercised with actual SSPs and other acoustical parameters corresponding to real oceans. It is also unclear at this time how rough sea surface scattering may affect these results.

However, it is apparent from this thesis that the source depth can have a major influence on the dominant angles of propagation and, as a consequence, bandwidth values. It is then reasonable to conclude that information exists in the measured bandwidth of a received source that might be helpful in determining the likely depth of the transmitting source. Obviously, BW effects could be significantly useful in the design of automatic classification schemes attempting to discriminate between sources on or below the ocean surface.

VIII. LIST OF REFERENCES

- [1] K. V. Mackenzie, "Long-Range Shallow-Water Signal-Level Fluctuations and Frequency Spreading," *The Journal of the Acoustical Society of America*, January 1962, Volume 34, Issue 1, pp. 67-75
- [3] Jack Shooter and Stephen K. Mitchell, "Observations of acoustic sidebands in cw tones received at long ranges," *The Journal of the Acoustical Society of America*, October 1976, Volume 60, Issue 2, pp. 829-832
- [3] John Glattetre, Tor Knudsen and Knut Sostrand, "Mode Interference and mode filtering in shallow water: A comparison of acoustic measurements and modeling," *The Journal of the Acoustical Society of America*, August 1989, Volume 86, Issue 2, pp. 680-690
- [4] William I. Roderick and Benjamin F. Cron, "Frequency Spectra of Forward-Scattered Sound from the Ocean Surface," *The Journal of the Acoustical Society of America*, January 1970, Volume 48, Issue 3, pp. 759-766
- [5] Suzanne T. McDaniel and Arthur D. Gorman, "Spectral spread of sea-surface reverberation," *The Journal of the Acoustical Society of America*, July 1983, Volume 74, Issue 1, pp. 241-248
- [6] J. L. Kays, M. J. Jacobson, and W. L. Siegmann, "Short-range acoustical effects of vertical and horizontal source-motion variations in a deep ocean." *The Journal of the Acoustical Society of America*, January 1981, Volume 69, Issue 1, pp. 95-107
- [7] J. L. Kays, M. J. Jacobson, and W. L. Siegmann, "Analysis of acoustical effects of relative receiver-source motion at intermediate ranges in a deep ocean," *The Journal of the Acoustical Society of America*, August 1980, Volume 68, Issue 2, pp. 613-627

- [8] J. L. Kays, M. J. Jacobson, and W. L. Siegmann, "Analysis of acoustical effects of receiver and source motions at short ranges in a deep ocean," *The Journal of the Acoustical Society of America*, October 1979, Volume 66, Issue 4, pp. 1120-1130
- [9] G. M. Jacyna and M. J. Jacobson, "General treatment of source motion on the total acoustic field with application to an isospeed channel," *The Journal of the Acoustical Society of America*, October 1976, Volume 60, Issue 4, pp. 815-824
- [10] G. M. Jacyna and M. J. Jacobson, "Analysis of source-motion effects on sound transmission in the deep ocean," *The Journal of the Acoustical Society of America*, May 1977, Volume 61, Issue 5, pp. 1153-1162
- [11] G. M. Jacyna and M. J. Jacobson, "Deep-water acoustical analysis of stationary and moving broadband sound sources," *The Journal of the Acoustical Society of America*, May 1978, Volume 63, Issue 5, pp. 1353-1364
- [12] R. P. Flanagan and N. L. Weinberg, "Effects of source motion on an acoustic signal in the frequency, time, and space domains," *The Journal of the Acoustical Society of America*, May 1980, Volume 67, Issue 5, pp. 1532-1544
- [13] R. P. Flanagan and N. L. Weinberg, "Effects of source micromotion on an acoustic signal in the frequency, time, and space domains," *The Journal of the Acoustical Society of America*, May 1980, Volume 67, Issue 5, pp. 1545-1552
- [14] Kenneth E. Hawker, "A normal mode theory of acoustic Doppler effects in the oceanic waveguide," *The Journal of the Acoustical Society of America*, March 1979, Volume 65, Issue 3, pp. 675-681
- [15] Jerome A. Neubert, "The effect of Doppler on long-range sound propagation The Journal of the Acoustical Society of America," December 1977, Volume 62, Issue 6, pp. 1404-1411
- [16] Henrik Schmidt and W. A. Kuperman, "Spectral and modal representations of the Doppler-shifted field in ocean waveguides," *The Journal of the Acoustical Society of America*, July 1994, Volume 96, Issue 1, pp. 386-395

- [17] Hee Chun Song and A. B. Baggeroer, "The resolution of modal Doppler shifts in a dispersive oceanic waveguide," *The Journal of the Acoustical Society of America*, July 1990, Volume 88, Issue 1, pp. 268-282
- [18] K. J. Howell, M. J. Jacobson, and W. L. Siegmann, "Parabolic approximation predictions of underwater acoustic effects due to source and receiver motions," *The Journal of the Acoustical Society of America*, July 1993, Volume 94, Issue 1, pp. 293-301
- [19] Kevin B. Smith, "Computing the Influence of Doppler Due to Source/Receiver Motion in a Parabolic Equation Model," *Journal of Computational Acoustics*, Vol. 10, No. 3, 2002, pp. 295-309.
- [20] Kevin B. Smith, "Convergence, Stability, and Variability of Shallow Water Acoustic Predictions Using a Split-Step Fourier Parabolic Equation Model," *Journal of Computational Acoustics*, Vol. 9, No. 1, 2001, pp. 243-285.
- [21] D. J. Thompson, and N.R. Chapman, "A Wide Angle Split Step Algorithm for the Parabolic Equation", *The Journal of the Acoustical Society of America*, December 1983, Volume 74, Issue 6, pp. 1848-1854
- [22] David Middleton, "Doppler effects for randomly moving scatterers and platforms," *The Journal of the Acoustical Society of America*, May 1977, Volume 61, Issue 5, pp. 1231-1250
- [23] Michael Wild and Robert Joyce, "Three-dimensional modeling of narrow-band pulse spreading using normal modes," *The Journal of the Acoustical Society of America*, October 1993, Volume 94, Issue 4, pp. 2303-2306
- [24] Michael Wild and Robert Joyce, "Modeling the spatial and frequency distribution of narrow-band acoustic signals scattering from the ocean surface," *The Journal of the Acoustical Society of America*, March 1995, Volume 97, Issue 3, pp. 1559-1565

- [25] Guy V. Norton and Jorge C. Novarini, "The effect of sea-surface roughness on shallow water waveguide propagation: A coherent approach," The Journal of the Acoustical Society of America, April 1996, Volume 99, Issue 4, pp. 2013-2021
- [26] Guy V. Norton and Jorge C. Novarini, "Coupling scattering from the sea surface to a one-way marching propagation model via conformal mapping: Validation," The Journal of the Acoustical Society of America, April 1995, Volume 97, Issue 4, pp. 2173-2180
- [27] F.D. Tappert, "The parabolic approximation method," in Lecture Notes in Physics, Vol. 70, Wave Propagation and Underwater Acoustics, eds. J. B. Keller and J.S. Papadakis, Springer Verlag, New York, 1977, p.p. 224-287.
- [28] R. H. Hardin and F.D. Tappert, "Applications of the split-step Fourier method to the numerical solution of nonlinear and variable coefficient wave equations," SIAM Rev. 15, 423, 1973.
- [29] Bellman, R. Perturbation Techniques in Mathematics, Physics, and Engineering, Holt, Rhinehart and Winston, Inc., New York, 1964, pp. 38-39.
- [30] D.J. Thomson, and C.S. Bohun, "A wide angle initial field for the parabolic equation models," The Journal of the Acoustical Society of America, 1988, Volume 83, S118
- [31] Medwin, H, and C. S. Clay, Fundamentals of Acoustical Oceanography, (Academic Press, San Diego, 1998), pp. 119-120.
- [32] Kinsler, Frey, Coppins & Sanders, Fundamentals of Acoustics, Fourth Edition, John Wiley & Sons, New York, 2000, pp 224-228.
- [33] C. G. Fox, and Hayes, D.E., "Quantitative methods for analyzing the roughness of the seafloor," Rev. Geophysics, Vol. 23, 1985, pp. 1-48.
- [34] K. B. Smith, W. Hodgkiss, and F.D. Tappert, "Propagation and analysis issues in the prediction of long-range reverberation," The Journal of the Acoustical Society of America, March 1996, Volume 99, Issue 3, pp. 1387-1404.

- [35] L. B. Dozier, "PERUSE: A numerical treatment of rough surface scattering for the parabolic wave equation," *The Journal of the Acoustical Society of America*, May 1984, Volume 75, Issue 5, pp. 1415-1432.
- [36] Fred Tappert and Lan Nghiem-Phu, "A new split-step Fourier algorithm for solving the parabolic wave equation with rough surface scattering," *The Journal of the Acoustical Society of America*, Spring 1985, Volume 77, Issue 1, pp. S101.
- [37] A. Tolstoy, K. B. Smith, and N. Maltsev, "The SWAM'99 Workshop – an overview," *Journal of Computational Acoustics*, Vol. 9, No. 1, 2001, pp. 1-16.
- [38] D. Mikhin, "Energy-conserving and reciprocal solutions for higher-order parabolic equations," *Journal of Computational Acoustics*, Vol. 9, No. 1, 2001, pp. 183-216.
- [39] Newland, D.E. Introduction to Random Vibrations and Spectral Analysis, Longman House, Essex, 1984, pp. 108.
- [40] Papoulis, A., Probability, Random Variables and Stochastic Processes, McGraw-Hill, New York, 1965, pp. 144.
- [41] Jensen et. al., Computational Ocean Acoustics, Springer-Verlag, New York, 2000, pp. 142-170.
- [42] Kevin B. Smith "Lecture Notes, Sound Propagation in the Ocean", Unpublished, Naval Postgraduate School, Monterey, CA. 2001.
- [43] Robert Kraichnan, "Electromagnetic Analogy to Sound Propagation in Moving Media," *The Journal of the Acoustical Society of America*, May 1955, Volume 27, Issue 3, pp. 527-530.
- [44] James Luscomb, "Classical Mechanics as a Foundation for Quantum Mechanics," (unpublished lecture notes), Department of Physics, Naval Postgraduate School, Monterey, CA, 2001.
- [45] Kevin B. Smith, Michael G. Brown, and Frederick D. Tappert, "Ray Chaos in Underwater Acoustics," *The Journal of the Acoustical Society of America*, April 1992, Volume 91, Issue 4, pp. 1939-1949.

[46] Dahlquist G., and A. Bjorck, Numerical Methods, Prentice-Hall, Englewood Cliffs New Jersey, 1974, pp. 346-347.

APPENDIX A. USER'S GUIDE FOR THE M3PE MODEL

This appendix provides a guide for executing the M3PE model with user defined inputs that define operating modes and environmental acoustic parameters. The first sub-section describes the various MATLAB files for execution, control, and environment definition. A flow diagram indicating the functions performed by the various executable files is described. Next the definition of control parameters and their optional values is described. Finally, the format and content of the environment definition files is described.

A.1 EXECUTABLE FILES

The M3PE model is executed by a series of functions contained in the files listed in alphabetical order in Table 5. All the files in Table 5 are executable by MATLAB.

Table 5. MATLAB file names of functions executing the M3PE model

Number	Filename	Description
1	brough.m	Computes a bottom roughness function that is applied to the mean bottom depth. The approach is based upon Fox & Hayes' definition as described by Smith, Hodgkiss and Tappert ³⁴ .
2	bw_eff.m	Computes the effective bandwidth of data in a three dimensional matrix, along the last dimension. Plots of the overall and conditional histograms of the features are generated if specified.
3	get_env.m	Defines SSPs, bottom depths, and environmental parameters vs range from the options allowed. Applies desired bottom roughness. Applies transition functions at bottom boundary.

4	init_m3pe.m	Defines operating parameters that control the execution of the M3PE code.
5	kfilter.m	Computes a one sided taper function (sponge) for application in k-space.
6	m3pe.m	Main program of the Matlab Monterey-Miami Parabolic Equation model. Computes a transmission loss in range and depth using the Split-Step Fourier PE model.
7	m3pe_src.m	Produces the starting source field for the M3PE model. It creates a source field in k-f space that accounts for source motion. It also creates parameters that are used to implement effects of receiver motion.
8	plot_rkf.m	Plots the wavenumber-frequency response at a particular range.
9	raytrace.m	Traces a bundle of rays from a source position, out to a maximum horizontal range using a Hamilton-Jacobi approach, implemented with the 4th order. Runge-Kutta / Simpson's rule method. Perfect reflection boundaries are included (if desired).
10	read_env.m	Reads the user specified parameters contained in the specified text file.
11	zfilter.m	Computes a one sided taper function (sponge) for application in z-space.

The executable software also interfaces to two other files used for inputting acoustical parameters and outputting the very large three dimensional complex acoustic field computed when source and receiver motion are greater than zero.

Table 6. Input/output files

Number	Filename	Description
1	m3pe_envx.dat	Contains parameters defining the range-dependent ocean acoustic environmental parameters, such as water SSP, density, water absorption characteristics (temperature, salinity, pH), bottom sound speed, gradient of sound speed, density, and attenuation. Also defines the bottom depth versus range.
2	psi.dat	Temporary storage file of the complex acoustic field vs range, depth, and frequency.

The main program is called *m3pe.m*, and serves as the origin for all other functions. A diagram indicating the functional flow of *m3pe.m* including the function dependencies is given in Figs. 92 and 93. The program is designed to repeat its execution on multiple environments. The function *get_env.m* inputs the environmental data and computes all the range-dependent acoustical parameters. These are input to the function *m3pe_src.m* which computes the starting field in wavenumber vs frequency space. Taper functions applied to the wavenumber and depth propagators are computed by the functions *kfilter.m* and *zfilter.m*, respectively. Next, the wavenumber and depth propagator functions are computed for the initial starting range. After transforming the starting field from wavenumber to depth space, via an inverse discrete Fourier transform (IDFT), the depth propagator is applied for the first range cell. In a loop on the remaining range cells, the propagated field is transformed back to k space (via DFT), multiplied by the wavenumber propagator, and inverse transformed back to depth space. Then the depth propagator is applied in two stages, so that the field stored to disk can represent the middle of a range step. If source and/or receiver motion is being modeled, these operations are repeated for all frequency bins. After all range cells are completed, the resulting complex transmission loss is

normalized and plotted versus range, depth, and frequency. The magnitudes of the unnormalized field in three dimensions (r,z,f) are input to the *bw_eff.m* function that computes aggregate and dependent statistics on the bandwidth of TL vs frequency. Finally, a ray trace is computed for the given SSP and bottom profile by the function *raytrace.m*.

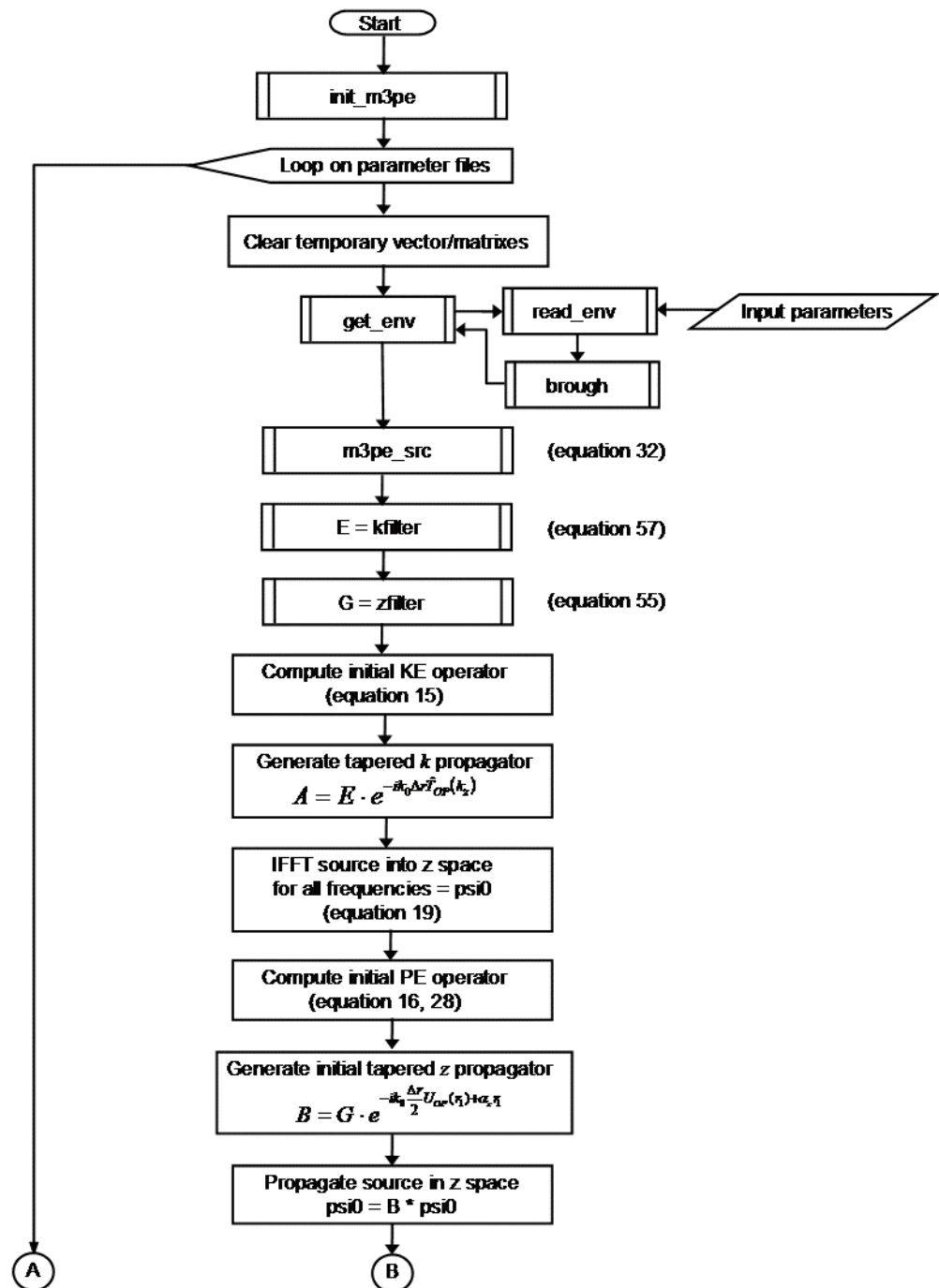


Figure 92. M3PE Functional Flow (part a)

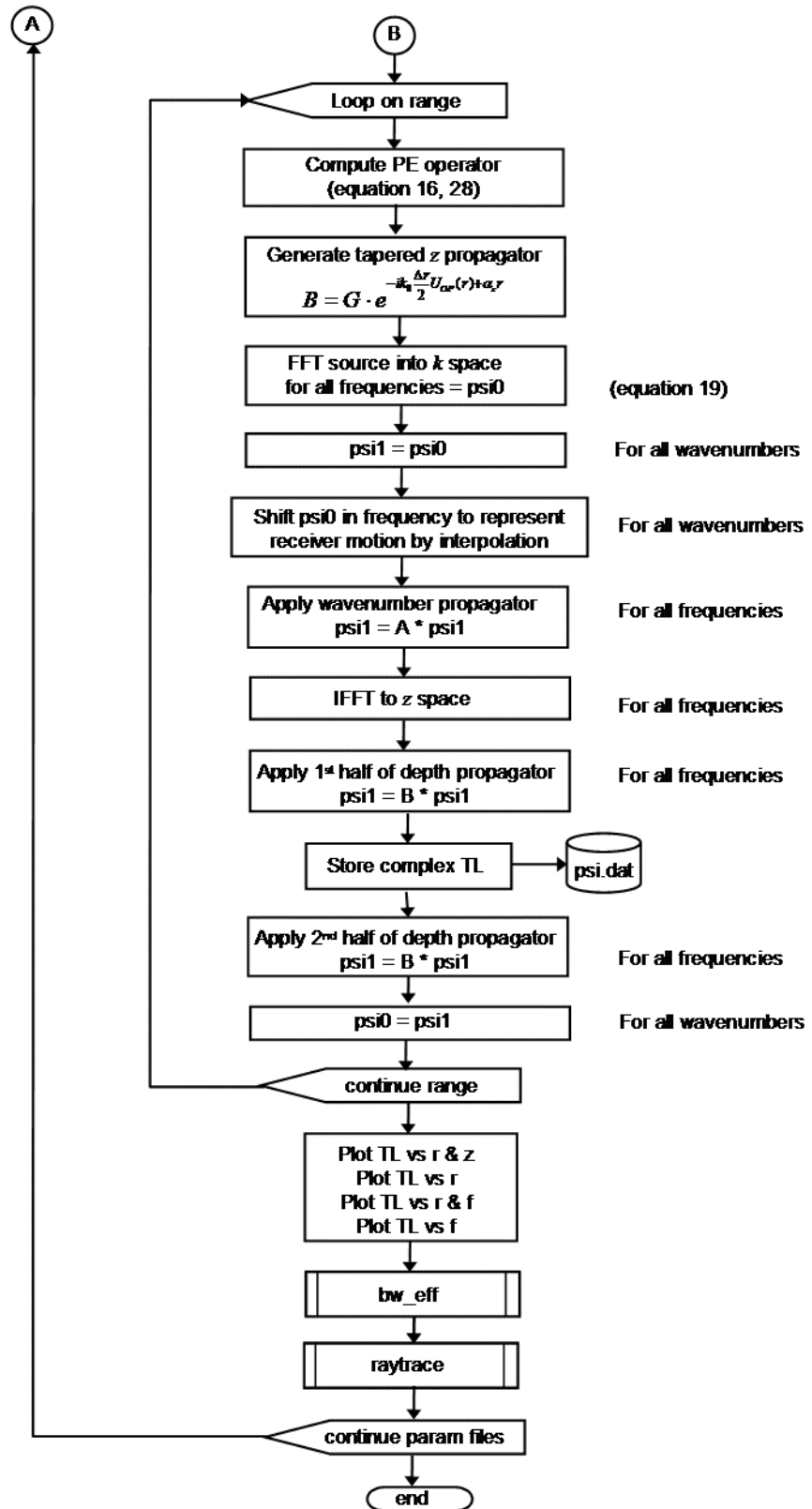


Figure 93. M3PE Functional Flow (part b)

A.2 CONTROL PARAMETER DEFINITIONS

The values of parameters that control operation of the M3PE model, including selection of various execution options, are defined in the file *init_m3pe.m*. This is a MATLAB executable file that is included in *m3pe.m* at the beginning of the file. A list of all the selectable parameters, along with their optional values and nominal constraints is contained in Table 7.

Table 7. Control parameter definitions

Num	Parameter	Units	Description	Normal Constraints
1	f	Hz	Transmit frequency	$5 < f < 5000$
2	zs	m	Source depth	> 0
3	thsd	degrees	Source vertical angle of motion	$-90 < \text{thsd} < 90$
4	thrd	degrees	Receiver vertical angle of motion	$-90 < \text{thrd} < 90$
5	vsk	knots	Source speed	$-100 < \text{vsk} < 100$
6	vrk	knots	Receiver speed	$-100 < \text{vrk} < 100$
7	Nf	integer	Number of frequency cells	Nominally < 100
8	nfiles	integer	Number of environments to run	< 10
9	use_file	Boolean integer	= 1 to use a disk file for temp storage	1 or 0
10	filename(:, :)	ascii	Matrix of environment file names	Name ≤ 50 chars
11	Nr	integer	Number of range cells	$32 \leq \text{Nr} \leq 16384$ (radix 2)
12	Nz	integer	Number of depth cells	$32 \leq \text{Nz} \leq 16384$ (radix 2)
13	c0	m/s	Reference sound speed	1500 m/s
14	WAPE	Boolean integer	= 1 to use wide angle PE model otherwise use narrow angle	1 or 0
15	batten	Boolean integer	= 1 to invoke bottom attenuation	1 or 0

16	binterp	Boolean integer	= 1 to perform horizontal interpolation of bottom parameters	1 or 0
17	do_cyl_spread	Boolean integer	= 1 to include cylindrical spreading term in TL calculation	1 or 0
18	dorho	Boolean integer	= 1 to include density in propagator function	1 or 0
19	doalw	Boolean integer	= 1 to include attenuation in the water column	1 or 0
20	dorcw	Boolean integer	= 1 to accommodate receiver motion	1 or 0
21	doraytrace	Boolean integer	= 1 to compute and plot a raytrace	1 or 0
22	dobw	Boolean integer	= 1 to compute bandwidth statistics	1 or 0
23	dork	Boolean integer	= 1 to save a k-f plot in the received field	1 or 0
24	maxTL	dB	Maximum TL for color coded plots	-500 < maxTL < 500
25	minTL	dB	Minimum TL for color coded plots	-500 < minTL < 500
26	zplot	m	Depth to plot TL vs range	0 < zplot < maxZ
27	zbplot	m	Depth to plot TL vs frequency	0 < zbplot < maxZ
28	Rbplot1	m	Min range to plot TL vs frequency	0 < Rbplot1 < maxR
29	Rbplot2	m	Max range to plot TL vs frequency	0 < Rbplot2 < maxR
30	Rkplot	m	Range to save k-f spectral plot	0 < Rkplot < maxR

The parameters in Table 7 are defined in the file *init_m3pe.m* following all MATLAB assignment conventions. Here it is appropriate to discuss a few caveats regarding some of these variables. First, all source and receiver angles of motion are positive down. Second, a positive source or receiver speed implies motion towards increasing horizontal coordinates. Conversely, a negative speed implies

motion towards decreasing horizontal coordinates. Regarding the mesh size definitions, it is also important to note that the product of $Nz \times Nr \times Nf$ has a limit determined by the amount of random axis memory (RAM) installed in the computer on which the model is being executed. The product can be expanded if the *use_file* option is selected, but in either case, a limit exists that is best determined by experimentation. The nominal constraints listed in Table 7 were selected based upon experience with a computer containing 512 MB of RAM.

Regarding the binary parameters listed in items 14-23 (in Table 7), most of them are usually set to 1, when a comprehensive set of results are desired. For example, the *WAPE* variable is only provided if one desires to evaluate the difference between wide and narrow angle approximations for academic purposes. The wide angle mode should always be selected to provide the best accuracy. Similarly, the *do_cyl_spread*, *batten*, *dorho* and *doalw* parameters should only be “turned off” (i.e. set to zero) for special test cases. Obviously these need to be enabled to achieve the best accuracy. The *dorcv* parameter is required if the model is to account for receiver motion. Next, the *doraytrace*, *dobw*, and *dork* parameters simply control the execution of post processing and plotting functions and can be selected according to individual preferences.

A cautionary note needs to be discussed regarding the *binterp* parameter. It should only be enabled when the bottom acoustical parameters are range dependent but the bottom depth is constant. This is because the flag causes a horizontal interpolation of the bottom parameters with range that is not yet designed to handle variable bottom depths. Finally, the parameters listed in rows 24-30 (of Table 7) specify various plotting options that are desirable for observing the TL versus frequency response when the source or receiver speeds are greater than zero.

A.3 ENVIRONMENT DEFINITION FILES

This section describes the format of acoustical parameters specified in the ocean environment definition files referenced on row 1 in Table 6. These files

allow specification of all acoustical parameters used by the M3PE model by simply editing a single ASCII file. Although Table 6 indicates the name of the files as having the prefix *m3pe_envx*, any file name can be assigned to the *filename* variable listed in row 11 in Table 7. A list of the parameters contained in this file is given in Table 8.

Table 8. Parameters contained in the environmental definition files

Num	Parameter	Units	Normal Constraints
1	Number of SSPs	integer	> 0
2	Range of SSP	m	$0 < \text{rssp} < \text{maxR}$
3	SSP – depth vs sound speed	m - m/s	$1450 < c(z,r) < 1550$
4	Sound speed in bottom	m/s	$1450 < c(z,r) < 1550$
5	Sound speed gradient in bottom	1/s	$-20 < \text{cgrad} < 20$
6	Salinity in water	ppm	$30 < S < 40$
7	pH in water	n/a	$1 < \text{pH} < 20$
8	Average temperature in water	°C	$-10 < T < 50$
9	Attenuation in bottom	dB/λ	$0 < \alpha_B < 10$
10	Density profile in water – depth vs rho	m - kg/m ³	$900 < \rho_w < 1500$
11	Density in bottom	kg/m ³	$1000 < \rho_w < 3000$
12	Density gradient in bottom	kg/m ²	$-20 < \text{rgrad} < 20$
13	Bottom depth vs range	m - m	$0 < z_b < 10000$
14	Bottom roughness magnitude	m	$0 < \sigma < 100$
15	Roughness type	integer	1 = uniform, 2 = Gaussian, 3 = Fox-Hayes, 4 = sawtooth right, 5 = sawtooth left
16	Correlation length	m	Used only by options 3-5

Several of the variables listed in Table 7 are two dimensional. For

example, in rows 3 and 10, the sound speed and density are defined as piece-wise linear functions of depth. Also, row 13 refers to the piece-wise linear definition of the bottom depth versus range. All other parameters are single scalar variables. We also note that, although the density gradient in row 12 is specified, it is not yet used by the model.

For the case of a range-dependent ocean, the parameters defined in rows 2-12 in Table 7 are repeated for each discrete range cell. In this case, the “range of SSP” variable specified in row 2 is assigned the range value that corresponds to the acoustical parameters immediately following it. The “number of SSPs” variable defined in the first row determines the number of sets of acoustical parameters contained in the file. After all range-dependent parameter sets are defined, the bottom depth profile and roughness parameters are listed at the end of the file.

A listing of the contents of an example file is provided in Fig. 94. It can be observed that the lines of ASCII text can be grouped into four different types. The first type is preceded by a delimiter containing a single ‘%’ character followed by a line of text. The second type begins with the ‘%’ character and is then followed by a line of dashes (‘-’). The third type of line only contains a pair of percent characters (“%”). The final type contains numeric characters that may or may not be followed by spaces and text characters.

The first several lines in the parameter file, preceded by a ‘%’ character, can contain any text entered by the user. Next the parameter “Number of SSPs” must be preceded and followed by a line of dashes as shown in Fig. 94. After the first line of dashes, all the other lines of text preceded by a ‘%’ delimiter need to contain the exact headings listed in the figure. The user is hereby cautioned not to modify these lines. For example the text phrases “SSP water layer,” “SSP bottom layer,” and “Volume Absorption” must all precede the data corresponding to their labels. Also between each type of range-dependent parameters, e.g. “SSP in water”, “Volume Absorption,” or “Bottom Absorption” parameters, the file contains another delimiter represented by the ‘%’ characters. These are only

inserted between the range-dependent parameters that can be repeated according to the “Number of SSPs” parameter. Finally each line containing numeric values of some parameter can also contain a series of text symbols on the same line. However one or more ASCII spaces or tab characters must be inserted between the data and the text.

The environmental parameter file is read by the function *read_env.m*, referenced in the flow diagram in Fig. 92. This function also has a stand-alone mode that allows reading a file simply into the MATLAB workspace. Then the variables can be individually evaluated to ensure consistency with expectations.

```

% File m3pe_env1.dat
% This file contains parameters that describe
% the acoustic environment of a modeled ocean
%
% Number of SSPs
1
%
% SSP water layer (to max bot dep spec'd below)
0      range associated with SSP
% depth (m)  sound speed (m/s)
0          1500
200        1480
3000       1540
%%
% SSP bottom layer parameters
1600      Sound speed
.2        Gradient (del SOS / del depth)
%%
% Volume Absorption parameters
35          Salinity (ppm)
8            pH
15.6        Temperature (deg C)
%%
% Bottom Absorption parameter
0.1        dB/lambda
%%
% DP of water (Density vs depth of water) layer
% depth (m)  density (kg/m^3)
0            1024
3000        1024
%%
% DP of bottom (Density params of bottom) layer
1700        Density
0            Gradient (del dens / del depth)
%
% Bottom depth vs range (m)
% depth (m)  range (m)
3000        0
3000        10000
2000        20000
1000        30000
500          35000
500          40000
%
% Bottom roughness parameter
1            roughness pk-pk magnitude (m)
3            rtype, 1 = uniform, 2 = Gaussian, 3 = Fox-
Hayes, 4 = sawtooth right, 5 = sawtooth left
100         Lst = length of sawtooth (m) if applicable
%

```

Range dependent.
Can be repeated
according to the
Number of SSPs
definition at the top.

Figure 94. Example ocean environment definition file

THIS PAGE INTENTIONALLY LEFT BLANK

APPENDIX B. RANGE DEPENDENT RAY TRACE FUNCTION

This appendix presents the derivation of the method used to produce the ray traces included throughout this thesis. The first section derives the mathematics associated with ray theory, and the second section describes the numerical technique which solves the equations. A third section provides a description of the MATLAB code that implements the functions.

B.1 RAY THEORY

The first part of our discussion below closely follows parts of Refs. 41 and 42. We begin by restating the homogenous Helmholtz equation as

$$\nabla^2 p + \frac{\omega^2}{c^2(\mathbf{x})} p = 0 \quad , \quad (B1)$$

where \mathbf{x} is the cartesian space coordinate. As usual, we can again assume that the pressure is a spatially variant time harmonic function defined by

$$p(\mathbf{x}) = A(\mathbf{x}) e^{i\omega\tau(\mathbf{x})} \quad . \quad (B2)$$

Then the spatial gradient is

$$\nabla p = e^{i\omega\tau} (\nabla A + i\omega A \nabla \tau) \quad , \quad (B3)$$

and the Laplacian is

$$\nabla p^2 = e^{i\omega\tau} \left(i\omega \nabla A \cdot \nabla \tau - \omega^2 A |\nabla \tau|^2 + \nabla^2 A + i\omega \nabla A \cdot \nabla \tau + i\omega A \nabla^2 \tau \right) \quad . \quad (B4)$$

Substituting (B4) into (B1), and dropping the time-dependent term, results in

$$i\omega \nabla A \cdot \nabla \tau - \omega^2 A |\nabla \tau|^2 + \nabla^2 A + i\omega \nabla A \cdot \nabla \tau + i\omega A \nabla^2 \tau + \frac{\omega^2}{c^2} A = 0 \quad . \quad (B5)$$

Equation (B5) is true when both the real and imaginary parts are equal to zero. Thus,

$$\nabla^2 A - \omega^2 A |\nabla \tau|^2 + \frac{\omega^2}{c^2} A = 0 \quad (B6)$$

and

$$\omega \nabla A \cdot \nabla \tau + \omega \nabla A \cdot \nabla \tau + \omega A \nabla^2 \tau = 0 \quad . \quad (B7)$$

Next we take the limit of Eqs. (B6) and (B7) as $\omega \rightarrow \infty$, which results in

$$|\nabla \tau|^2 = \frac{1}{c^2} \quad (B8)$$

and

$$2 \nabla A \cdot \nabla \tau + A \nabla^2 \tau = 0 \quad . \quad (B9)$$

Equation (B8) is commonly called the *eikonal* equation, while (B9) is called the *transport* equation. The *eikonal* equation determines the trajectory of vectors that are perpendicular to the wavefront, or position of constant phase. The *transport* equation determines the amplitude along the wavefront trajectory. To derive the ray tracing formulae, we focus on the *eikonal* equation.

Equation (B8) can be rewritten in cylindrical coordinates as

$$\left(\frac{\partial \tau}{\partial r} \right)^2 + \left(\frac{\partial \tau}{\partial z} \right)^2 + \left(\frac{1}{r} \frac{\partial \tau}{\partial \phi} \right)^2 = \frac{1}{c(r, z, \phi)^2} \quad . \quad (B10)$$

Here we note that the speed of sound is defined to be generally variable with all spatial coordinates. If we neglect azimuthal variations, this becomes

$$\left(\frac{\partial \tau}{\partial r} \right)^2 + \left(\frac{\partial \tau}{\partial z} \right)^2 = \frac{1}{c(r, z)^2} \quad . \quad (B11)$$

Eqs. (B10) and (B11) now have the form of a Hamilton-Jacobi equation used to describe the classical motion of a particle. The analogy between sound propagation and particle motion has been known for many years (see [43] for example). The following discussion shows how methods from classical mechanics provide a convenient framework for solving the acoustic wavefront trajectory problem.

Let us briefly digress to highlight some of the aspects of this analogous theory. Our discussion closely follows the contents of reference [44]. Hamilton's principle states that the actual path taken by a particle between fixed end points will be the path that minimizes a quantity called the "action". The action is defined as the integral of the difference between the kinetic energy, T (a function of velocity), and the potential energy, V (a function of position), defined according to

$$S = \int_{t_1}^{t_2} (T(\dot{x}) - V(x)) dt . \quad (B12)$$

Here the variable x defines the position, and t_1 and t_2 are the time end points for which the particle motion is being evaluated. The integrand is also called the Lagrangian, defined as $L(x, \dot{x}) = T(\dot{x}) - V(x)$. The variable \dot{x} refers to the time rate of change of x . In Hamiltonian mechanics, the momentum associated with a generalized coordinate, q_j , is a function of the Lagrangian according to

$$p_j = \frac{\partial L}{\partial \dot{q}_j} . \quad (B13)$$

The momentum p_j , the generalized coordinate variable q_j , and the Lagrangian, $L(q, \dot{q})$, together define the Hamiltonian function, $H(p, q)$, as

$$H(p, q) = \sum_{i=1}^D p_i \dot{q}_i - L(q, \dot{q}) \quad (B14)$$

where D is the dimensionality of the generalized coordinates, i.e. the number of degrees of freedom in the system.

The Hamiltonian is analogous to the total energy of the system⁴². It is related to the generalized coordinate and the momentum by the following first order equations:

$$p_j = -\frac{\partial H}{\partial q_j} , \quad (B15)$$

$$\dot{q}_j = \frac{\partial H}{\partial p_j} . \quad (B16)$$

Equations (B15) and (B16) are referred to as Hamilton's equations of motion. They represent a pair of first-order coupled differential equations that can be more easily solved than a higher order set of equations.

Given these tools, and recognizing τ as the action-like variable and r as the time-like variable in Eq. (B11), we can begin to solve (B11) by defining the momentum term, p , as

$$p = \frac{\partial \tau}{\partial z} . \quad (B17)$$

Then, Eq. (B11) can be rewritten as

$$\frac{\partial \tau}{\partial r} = \left(\frac{1}{c(r,z)^2} - p^2 \right)^{\frac{1}{2}} . \quad (B18)$$

Next, we can define the term $\frac{\partial \tau}{\partial r}$ as the negative of the Hamiltonian. That is

$$H(p,z,r) = -\frac{\partial \tau}{\partial r} = -\left(\frac{1}{c(r,z)^2} - p^2 \right)^{\frac{1}{2}} . \quad (B19)$$

Then, by using (B15) and (B16), it follows that

$$\dot{p} = \frac{dp}{dr} = -\frac{\partial H}{\partial z} , \quad (B20)$$

and

$$\dot{z} = \frac{dz}{dr} = \frac{\partial H}{\partial p} . \quad (B21)$$

Substituting (B19) into (B20) and taking the derivative results in

$$\frac{dp}{dr} = \frac{-1}{c(r,z)^3 \left(\frac{1}{c(r,z)^2} - p^2 \right)^{\frac{1}{2}}} \frac{dc(r,z)}{dz} = \frac{-1}{c(r,z)^2 (1 - c(r,z)^2 p^2)^{\frac{1}{2}}} \frac{dc(r,z)}{dz} . \quad (B22)$$

Performing this same substitution into Eq. (B21) also results in

$$\frac{dz}{dr} = \frac{p}{\left(\frac{1}{c(r,z)^2} - p^2 \right)^{\frac{1}{2}}} = \frac{c(r,z)p}{(1 - c(r,z)^2 p^2)^{\frac{1}{2}}} . \quad (B23)$$

Now recall that $\frac{dz}{dr}$ is nothing more than the slope of the ray perpendicular to the direction of the propagating wavefront in range and depth space. The relationship of this derivative to the grazing angle of propagation is

$$\tan(\theta) = \frac{dz}{dr} . \quad (B24)$$

Thus,

$$\frac{dz}{dr} = \tan(\theta) = \frac{\sin(\theta)}{\cos(\theta)} = \frac{c(r,z)p}{(1 - c(r,z)^2 p^2)^{\frac{1}{2}}} . \quad (B25)$$

Equating the numerators on both sides of (B25) results in the following simple definition for the momentum:

$$p = \frac{1}{c(r,z)} \sin(\theta) . \quad (B26)$$

In (B22), (B23), and (B26), we now have a system of equations that can be numerically integrated to solve for the trajectory in range and depth of a perpendicular ray to an acoustic phase front. Prior to discussing numerical methods, we also need an expression for the travel-time of a ray through space. This can be attained by using a method from classical mechanics as well. Again we closely follow reference [42]. In this case, Fermat's Theorem tells us that the travel time of a particle is related to the Lagrangian by

$$T = \int_{r1}^{r2} L(r, z) dr \quad . \quad (B27)$$

From (B14) the Lagrangian is related to the Hamiltonian by

$$L(z, r) = \frac{dp}{dr} - H(p, z, r) \quad . \quad (B28)$$

Also recall the definition of the Hamiltonian as

$$H(p, z, r) = - \left(\frac{1}{c(r, z)^2} - p^2 \right)^{\frac{1}{2}} = - \frac{1}{c(r, z)} (1 - c(r, z)^2 p^2)^{\frac{1}{2}} \quad . \quad (B29)$$

Substituting (B23) and (B29) into (B28) results in

$$L(z, r) = \frac{c(r, z)^2 p^2}{c(r, z) (1 - c(r, z)^2 p^2)^{\frac{1}{2}}} + \frac{(1 - c(r, z)^2 p^2)}{c(r, z) (1 - c(r, z)^2 p^2)^{\frac{1}{2}}} \quad . \quad (B30)$$

This can be simplified to

$$L(z, r) = \frac{1}{c(r, z) (1 - c(r, z)^2 p^2)^{\frac{1}{2}}} = \frac{1}{c(r, z) \left(1 - c(r, z)^2 \frac{\sin^2(\theta)}{c(r, z)^2} \right)^{\frac{1}{2}}} = \frac{1}{c(r, z) \cos(\theta)} \quad . \quad (B31)$$

Thus the integral of (B31) along the ray path provides the travel time of the ray between the endpoints of integration. That is

$$T = \int_{r1}^{r2} \frac{1}{c(r, z) \cos(\theta)} dr \quad . \quad (B32)$$

B.2 NUMERICAL SOLUTION

We now describe a procedure for generating the range and depth coordinates of an acoustical ray originating from a source position with a particular vertical launch angle. Our problem requires integration of Eqs. (B22) and (B23) over a horizontal range interval. This is performed using the Runge-Kutta Method, as described by Smith^{42,45} for this application. Our discussion also relies heavily upon reference [46].

Equations (B22) and (B23) follow the general form of a coupled first order ordinary differential equation that can be re-written as

$$\frac{dy}{dx} = f(x, y(x)) . \quad (B33)$$

This implies that the differential of a function, $y(x)$, is dependent upon the original function, and an independent variable, x . Problems of this sort can be solved by the recursion⁴⁴,

$$y_{n+1} = y_n + \int_{x_n}^{x_n+h} f(x, y(x)) dx , \quad (B34)$$

where h is the length of the sub-interval along the independent variable x . In the 4th order Runge-Kutta approach, the solution is obtained numerically by

$$y_{n+1} = y_n + \frac{1}{6} (k_1 + 2k_2 + 2k_3 + k_4) \quad (B35)$$

where

$$k_1 = h \cdot f(x_n, y_n) , \quad (B36a)$$

$$k_2 = h \cdot f\left(x_n + \frac{1}{2}h, y_n + \frac{1}{2}k_1\right) , \quad (B36b)$$

$$k_3 = h \cdot f\left(x_n + \frac{1}{2}h, y_n + \frac{1}{2}k_2\right) , \quad (B36c)$$

$$k_4 = h \cdot f(x_n + h, y_n + k_3) . \quad (B36d)$$

It is also interesting to note that if the function $f()$ is independent of $y(x)$, then $k_2 = k_3$ and (B36) reduces to Simpson's rule, (where h is substituted for $h/2$), i.e.,

$$y_{n+1} = y_n + \frac{h}{6} \left(f(x_n) + 4f\left(x_n + \frac{1}{2}h\right) + f(x_n + h) \right) .$$

We are now ready to show how the above methods can be applied to our problem. For completeness, we restate Eqs. (B22) and (B23) below:

$$\frac{dp}{dr} = \frac{-1}{c(r,z)^2 (1 - c(r,z)^2 p^2)^{\frac{1}{2}}} \frac{dc(r,z)}{dz} \quad (B22)$$

$$\frac{dz}{dr} = \frac{c(r,z)p}{(1 - c(r,z)^2 p^2)^{\frac{1}{2}}} \quad . \quad (B23)$$

In our case, the range variable r plays the role of the independent variable x in (B36). Also, the range increment Δr plays the role of the interval length h . The recursion relation for depth z can then be found from⁴²

$$z_{n+1} = z_n + \frac{1}{6} (k_1 + 2k_2 + 2k_3 + k_4) \quad . \quad (B37)$$

$$k_1 = \Delta r \frac{dz}{dr} (z_n, p_n, r) \quad , \quad (B38a)$$

$$k_2 = \Delta r \frac{dz}{dr} \left(z_n + \frac{1}{2} k_1, p_n + \frac{1}{2} m_1, r + \frac{\Delta r}{2} \right) \quad , \quad (B38b)$$

$$k_3 = \Delta r \frac{dz}{dr} \left(z_n + \frac{1}{2} k_2, p_n + \frac{1}{2} m_2, r + \frac{\Delta r}{2} \right) \quad , \quad (B38c)$$

$$k_4 = \Delta r \frac{dz}{dr} (z_n + k_3, p_n + m_3, r + \Delta r) \quad . \quad (B38d)$$

A similar set of steps must be simultaneously executed for the momentum, p according to

$$p_{n+1} = p_n + \frac{1}{6} (m_1 + 2m_2 + 2m_3 + m_4) \quad , \quad (B39)$$

$$m_1 = \Delta r \frac{dp}{dr} (p_n, z_n, r) \quad , \quad (B40a)$$

$$m_2 = \Delta r \frac{dp}{dr} \left(p_n + \frac{1}{2} m_1, z_n + \frac{1}{2} k_1, r + \frac{\Delta r}{2} \right) \quad , \quad (B40b)$$

$$m_3 = \Delta r \frac{dp}{dr} \left(p_n + \frac{1}{2} m_2, z_n + \frac{1}{2} k_2, r + \frac{\Delta r}{2} \right) \quad , \quad (B40c)$$

$$m_4 = \Delta r \frac{dp}{dr}(p_n + m_3, z_n + k_3, r + \Delta r) . \quad (B40d)$$

Our final step is to present the approach for computing the travel times by integrating the Lagrangian as presented in (B32). Smith⁴² recommends using Simpson's rule,

$$T = \frac{\Delta r}{3} [L(r) + 4L(r + \Delta r) + 2L(r + 2\Delta r) + \dots + 4L(r + (n-1)\Delta r) + L(r + n\Delta r)] . \quad (B41)$$

Here n is the number of range cells for which the Lagrangian (specified by (B31)) is evaluated. Thus, the Lagrangian, $L(r) = [c(z, r)\cos(\theta(z, r))]^{-1}$, is evaluated at each position along the ray path and plugged into (B41) to compute the travel time up to a particular position along the ray. The propagation angle, θ , can be found from (B26), i.e.

$$\theta(z, r) = \sin^{-1} [c(z, r)p(z, r)]^{-1} . \quad (B42)$$

B.3 MATLAB IMPLEMENTATION

A MATLAB function has been written to implement the method described in the previous sub-section. The function is called *raytrace*, and is executed by calling the function inside a main program. The inputs to the function are listed and described in Table 9. These inputs are specified in the argument list of the *raytrace.m* function.

It is noted that the sound speed and bottom depth can be range-dependent. However, due to the simplicity of the reflection method, it is not recommended that bottom depths with applied roughness be input to this routine. In the M3PE implementation, a mean bottom depth (without roughness) was used to create all the ray trace plots illustrated in the various sections of this thesis.

Table 9. Input Variables to the Raytrace Function

Number	Variable	Description
1	zs	Source depth
2	z	Depth vector
3	Nz	Number of depth cells
4	c	Speed of sound matrix (range vs depth)
5	maxR	Maximum range (m)
6	zb	Bottom depth vs range
7	itheta	Center angle in degrees of rays at the source
8	dtheta	Width of ray bundle in degrees
9	delth	Angle separation of rays at the source
10	nobounce	= 1 to suppress boundary interactions
11	pssp	= 1 to plot the ssp, 0 otherwise
12	istatus	= 1 to plot status messages

The outputs of the function consist of color plots of the ray trace and the travel time versus range. Each ray is given a separate color or line characteristic (solid versus dashed) to facilitate following the ray through range and depth space. A maximum of 12 separate line types are available. When greater than 12 rays are plotted, the color or line type characteristics are reused in modulo fashion. Optionally, the sound speed profile can also be plotted. Finally, the travel times versus launch angle and depth at the final range are printed to the workspace window in a formatted list.

The processing sequence within the *raytrace.m* routine is illustrated by the flow charts in Figs. 97 and 98. It can be observed that the numerical integration is performed inside two nested loops, over the range grid and for each individual ray.

When a boundary interaction is recognized, a series of linear interpolation operations are executed depending upon whether the boundary is the bottom or the surface. Figure 95 is provided to help illustrate our notation for the bottom interaction. In this case the incident ray impinges on the bottom at an

angle of θ_0 relative to the horizontal axis (positive angles down). The last sample of the ray before the bottom is exceeded is located at $[r_{n-1}, z_{n-1}]$, where “n” refers to the range index.

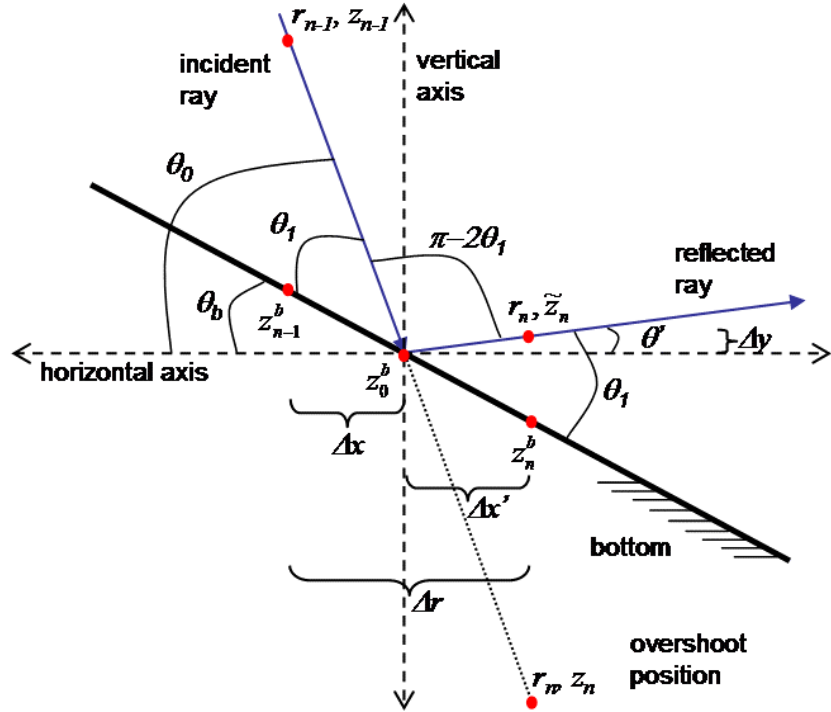


Figure 95. Bottom reflection geometry

The local angle of the bottom slope is

$$\theta_b = \tan^{-1} \left(\frac{z_n^b - z_{n-1}^b}{\Delta r} \right), \quad (B43)$$

where z_n^b is the bottom depth at the discrete range increment “n”, and Δr is the range resolution. Then the reflected momentum is

$$p = \sin \left(\frac{\theta_b - \theta_0}{c(z, r)} \right), \quad (B44)$$

Next, the depth of the ray after the reflection is computed for the discrete range associated with index “n” by the following steps. The angle between the incident ray and the bottom is

$$\theta_1 = \theta_0 - \theta_b \quad . \quad (B45)$$

The angle between the reflected ray and the horizontal axis is

$$\theta' = 2\theta_1 - \theta_0 \quad . \quad (B46)$$

The equation of the line defining the incident ray is

$$y = \frac{(z_n - z_{n-1})}{\Delta r} x + z_{n-1} \quad , \quad (B47)$$

and the equation of the local bottom is

$$y = \frac{(z_n^b - z_{n-1}^b)}{\Delta r} x + z_{n-1}^b \quad . \quad (B48)$$

Equating vertical variables provides a solution to the horizontal component of the incident ray,

$$\Delta x = \frac{(z_{n-1} - z_{n-1}^b) \Delta r}{(z_n^b - z_{n-1}^b) - (z_n - z_{n-1})} \quad . \quad (B49)$$

Here the origin, z_0^b , is the point at which the ray intersects the bottom. The horizontal component of the reflected ray is

$$\Delta x' = \Delta r - \Delta x \quad . \quad (B50)$$

The vertical component of the reflected ray is

$$\Delta y' = \Delta x' \tan(\theta') \quad . \quad (B52)$$

Finally, the new depth of the ray relative to the surface is

$$\tilde{z}_n = z_0^b - \Delta y' \quad . \quad (B53)$$

After the reflection, the ray is propagated from the point $[r_n, \tilde{z}_n]$ with the new momentum defined by Eq. (B44),

If the ray depth during the propagation loop becomes less than zero (at the surface) a similar approach is followed. An illustration of the geometry is provided in Fig. 96.

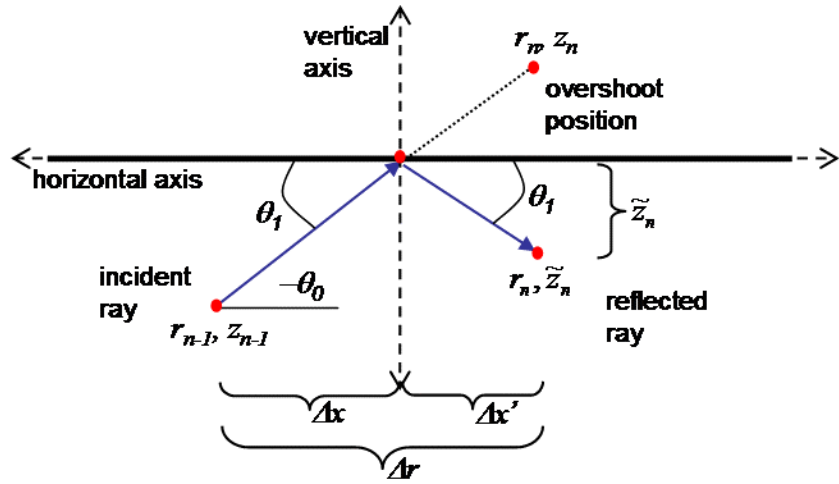


Figure 96. Surface reflection geometry

The ray depth after reflection is computed from the following steps. If θ_0 is the angle of the incident ray (positive down), then

$$\theta_1 = -\theta_0 \quad (B54)$$

is the angle between the incident ray and the horizontal axis. Then the horizontal component of the ray is

$$\Delta x = \frac{z_{n-1}}{\tan(\theta_1)} \quad (B55)$$

The horizontal component of the reflected ray is

$$\Delta x' = \Delta r - \Delta x \quad (B56)$$

Finally the vertical component is

$$\tilde{z}_n = \Delta x' \tan(\theta_1) \quad (B57)$$

From the point $[r_n, \tilde{z}_n]$, the ray is propagated with the new momentum

$$p = \sin\left(\frac{\theta_1}{c(z, r)}\right) \quad (B58)$$

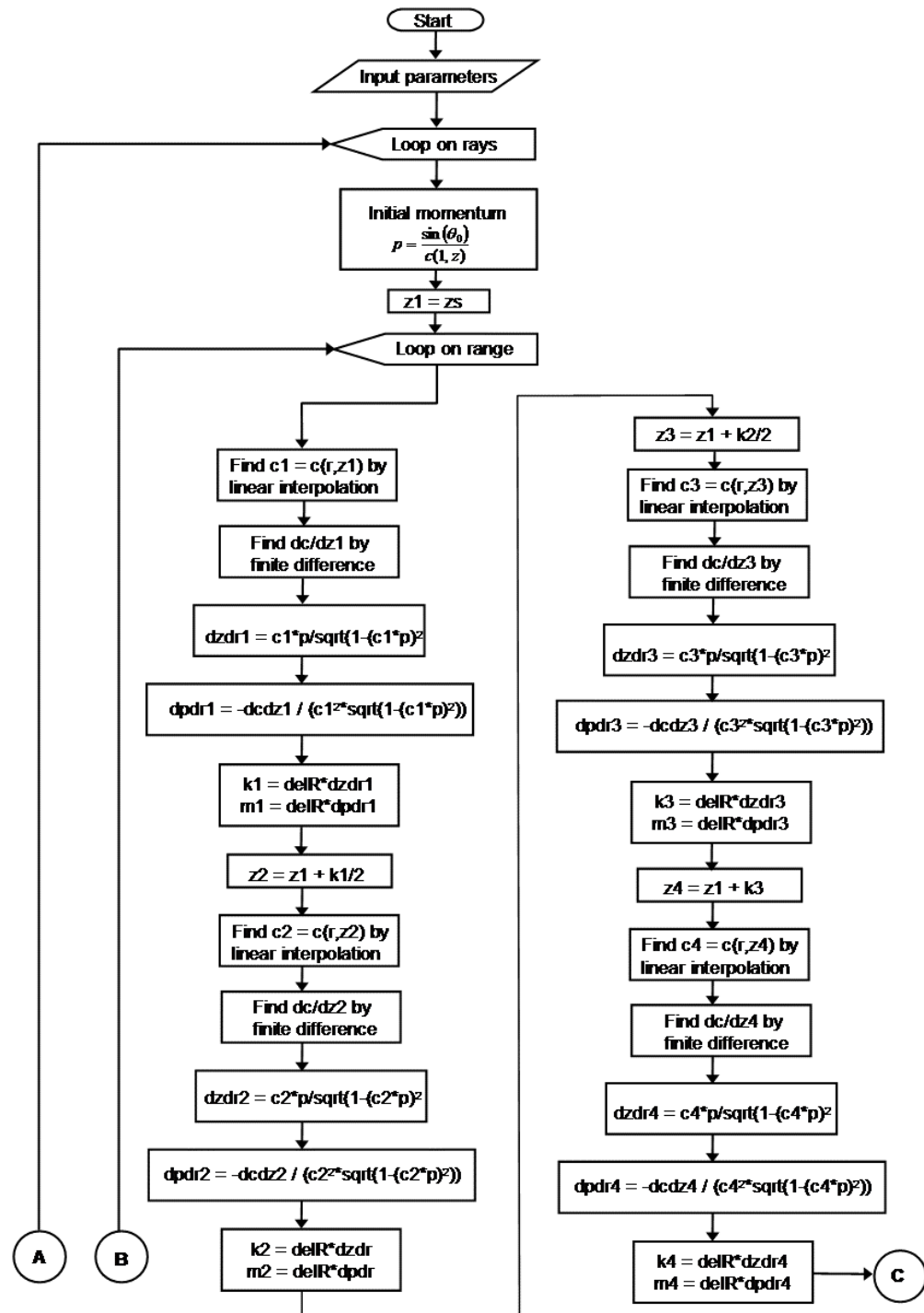


Figure 97. Flow Diagram of Raytrace Function, part (a)

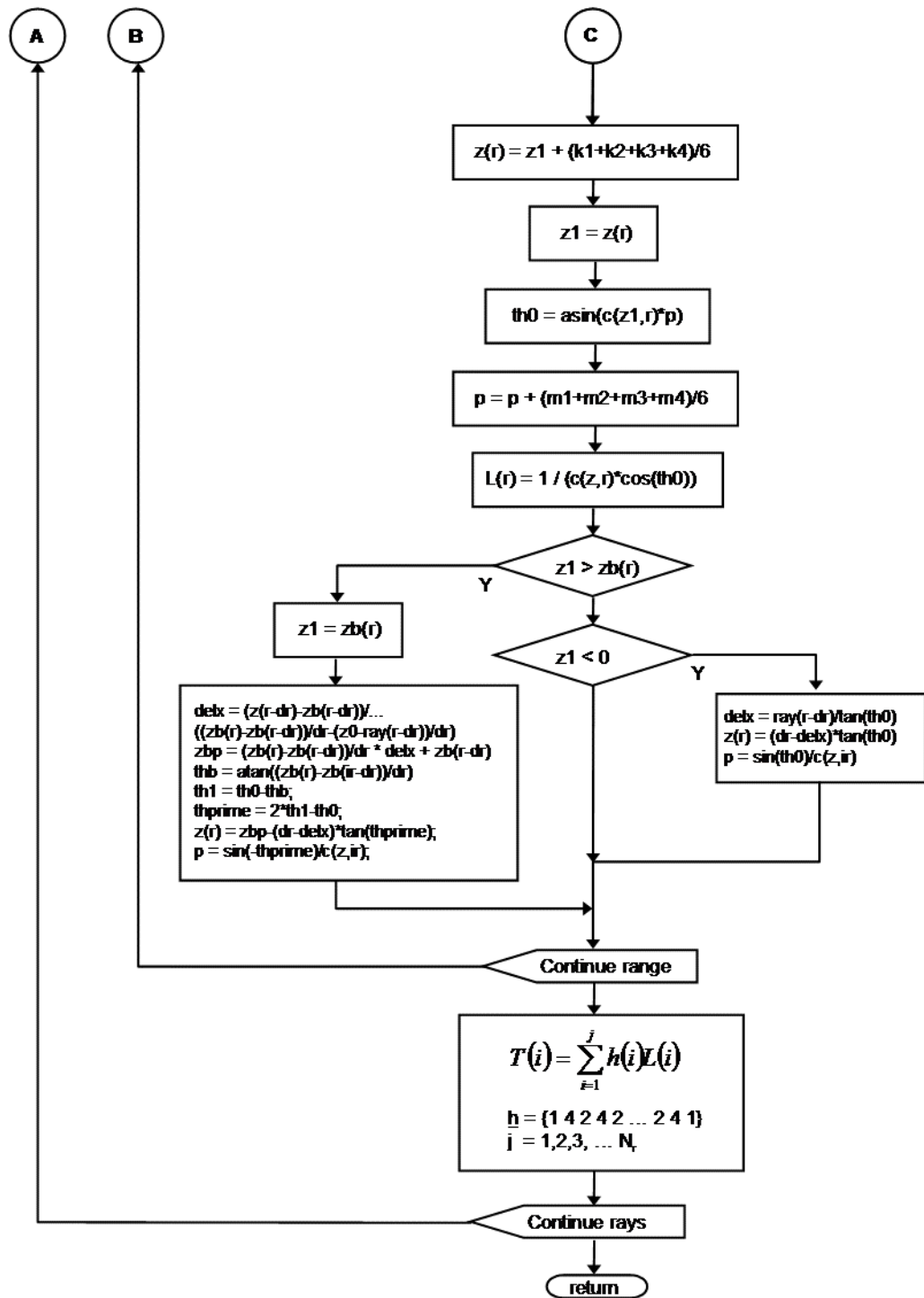


Figure 98. Flow Diagram of Raytrace Function, part (b)

B.4 BENCHMARK EXAMPLES

To illustrate its capabilities, the *raytrace* program was executed with Munk's canonical SSP down to a depth of 4500 m. A flat bottom was assumed out to a range of 200,000 m. The SSP is explicitly defined as follows:

$$c(z) = c_0 \left[1 + \varepsilon \left(e^{-\eta} + \eta - 1 \right) \right], \quad (B43)$$

where $\eta = \frac{2(z - z_{axis})}{B}$ and $z_{axis} = 1000$ m, $B = 1000$ m, $\varepsilon = 0.0057$, and $c_0 = 1490$ m/s. A plot of this SSP is illustrated in Fig. 99.

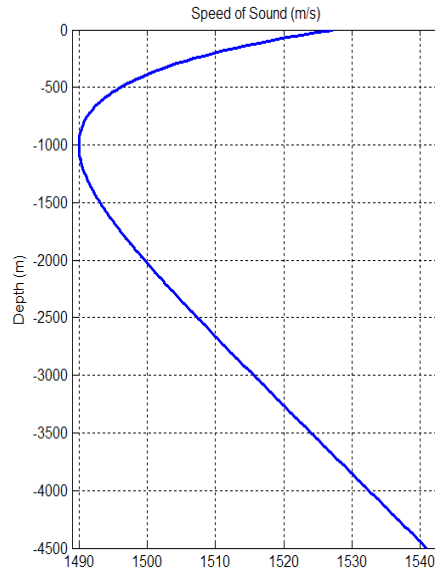


Figure 99. Munk's canonical profile

A mesh size of $N_z = 400$ and $N_r = 8000$ was selected for our plot. With the source depth, zs (from Table 9) equal to 1000 m, the rays propagating from launch angles between $[-30^\circ, 30^\circ]$ at 0.5° increments are plotted in Fig. 100. Figure 101 illustrates the trace from a source at 500 m. Reference 41 can be consulted to find examples using the Munk profile and a flat bottom for comparison.

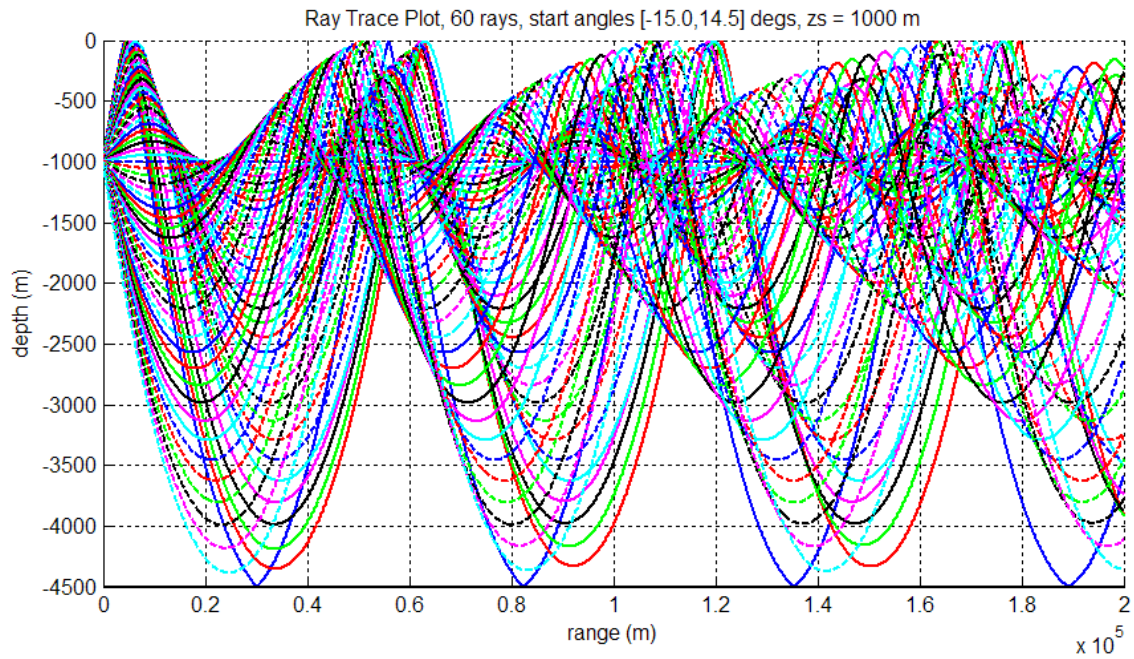


Figure 100. Example ray trace, $z_s = 1000$ m

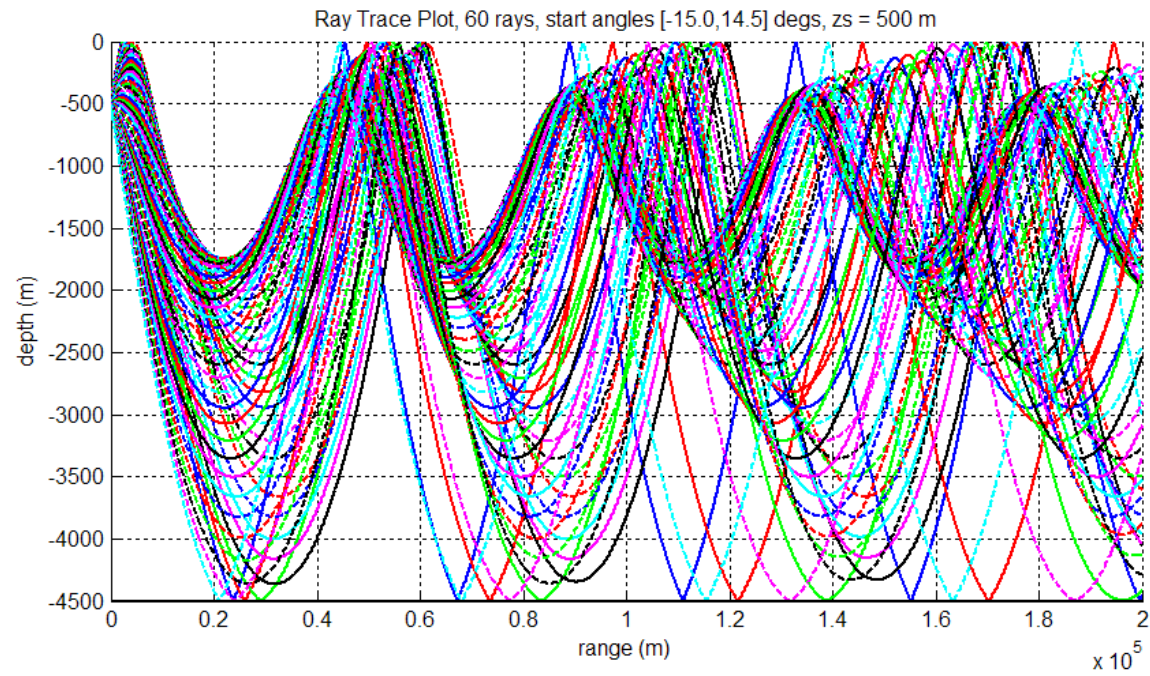


Figure 101. Example ray trace, $z_s = 500$ m

THIS PAGE INTENTIONALLY LEFT BLANK

APPENDIX C. SCALAR FORM OF THE KE OPERATOR

This appendix derives a scalar version of the KE operator defined in Eq. (20) that is equivalent to the operator form given by Eq. (16). The result is used as a multiplier in the wavenumber domain within the Split-Step Fourier marching algorithm defined by Eq. (21). We begin by restating Eq. (16) as

$$T_{OP} = 1 - \sqrt{1 + \mu} = 1 - \sqrt{1 + \frac{1}{k_0^2} \frac{\partial^2}{\partial z^2}} \quad . \quad (16)$$

Equation (16) can be generalized as

$$\hat{T}_{OP}(x) = 1 - \sqrt{1 + \frac{x^2}{k_0^2}} \quad . \quad (C1)$$

Then $\hat{T}_{OP}(x)$ can be expanded into a Maclaurin series as

$$\hat{T}_{OP}(x) = \sum_{n=0}^{\infty} \frac{\hat{A}_n}{n!} x^n \quad , \quad (C2)$$

where the coefficients A_n are the successive derivatives of $\hat{T}_{OP}(x)$ evaluated at zero according to

$$\hat{A}_n = \frac{\partial^n}{\partial x^n} \hat{T}_{OP}(x) \quad . \quad (C3)$$

Also

$$x = \frac{1}{k_0} \frac{\partial}{\partial z} \quad . \quad (C4)$$

Similarly, the operator T_{OP} can be rewritten as

$$T_{OP} \left(\frac{\partial}{\partial z} \right) = \sum_{n=0}^{\infty} \frac{A_n}{n!} \frac{\partial^n}{\partial z^n} \quad , \quad (C5)$$

where the exponential factor has been incorporated directly into the partial derivative.

Recall from Eq. (15) that T_{op} is applied to the PE field function $\psi(z)$. It then follows that

$$T_{op}\left(\frac{\partial}{\partial z}\right)\psi(z) = \sum_{n=0}^{\infty} \frac{A_n}{n!} \frac{\partial^n}{\partial z^n} \psi(z) . \quad (C6)$$

Then $\psi(z)$ can be written in terms of its wavenumber transform as

$$\psi(z) = \int \Psi(k_z) e^{ik_z z} dk_z . \quad (C7)$$

Substituting Eq. (C7) into (C6) results in

$$T_{op}\left(\frac{\partial}{\partial z}\right)\psi(z) = \sum_{n=0}^{\infty} \frac{A_n}{n!} \frac{\partial^n}{\partial z^n} \int \Psi(k_z) e^{ik_z z} dk_z . \quad (C8)$$

In (C8), it is possible to interchange the partial derivative and integral since only the exponential term in the integral is a function of z . The result is

$$T_{op}\left(\frac{\partial}{\partial z}\right)\psi(z) = \sum_{n=0}^{\infty} \frac{A_n}{n!} \int \Psi(k_z) \frac{\partial^n}{\partial z^n} (e^{ik_z z}) dk_z . \quad (C9)$$

After taking the derivatives, the result is

$$T_{op}\left(\frac{\partial}{\partial z}\right)\psi(z) = \sum_{n=0}^{\infty} \frac{A_n}{n!} \int \Psi(k_z) (ik_z)^n e^{ik_z z} dk_z . \quad (C10)$$

Then all the functions of the variable n , including the summation, can be brought inside the integral as

$$T_{op}\left(\frac{\partial}{\partial z}\right)\psi(z) = \int \Psi(k_z) \left(\sum_{n=0}^{\infty} \frac{A_n}{n!} (ik_z)^n \right) e^{ik_z z} dk_z . \quad (C11)$$

Now the terms in the parenthesis in the right side of Eq. (C11) have the same form as Eq. (C2). Therefore we can rewrite (C11) as

$$T_{op}\left(\frac{\partial}{\partial z}\right)\psi(z) = \int \Psi(k_z) \hat{T}_{op}(k_z) e^{ik_z z} dk_z . \quad (C12)$$

Since Eq. (C2) is equivalent to Eq. (C1), it follows that

$$\hat{T}_{op}(k_z) = 1 - \sqrt{1 - \frac{k_z^2}{k_0^2}} \quad , \quad (C13)$$

Thus, Eq. (C12) tells us that applying the operator T_{op} to the field function $\psi(z)$ is equivalent to multiplying the scalar function $\hat{T}_{op}(k_z)$ by the transformed field $\Psi(k_z)$ and transforming the result back into the z domain.

THIS PAGE INTENTIONALLY LEFT BLANK

INITIAL DISTRIBUTION LIST

1. Defense Technical Information Center
Ft. Belvoir, Virginia
2. Dudley Knox Library
Naval Postgraduate School
Monterey, California
3. Technical Library
Naval Undersea Warfare Center
Newport, Rhode Island
4. Dr. Kevin Smith
Naval Postgraduate School
Monterey, California
5. David Pistacchio
Naval Undersea Warfare Center
Newport, Rhode Island
6. Dr. Roy L. Streit
Naval Undersea Warfare Center
Newport, Rhode Island